Mapping of structures and properties evolved during sono-electroplating of nickel thin films

A thesis submitted in partial fulfilment of the requirements for the degree of

Master of Technology
In
Metallurgical & Materials Engineering

Submitted
By

Madhusmita Moharana
Roll No. – 211MM1382

Department of Metallurgical & Materials Engineering
National Institute of Technology
Rourkela
2013

Mapping of structures and properties evolved during sono-electroplating of nickel thin films

A thesis submitted in partial fulfilment of the requirements for the degree of

Master of Technology
In
Metallurgical & Materials Engineering

Submitted
By

Madhusmita Moharana
Roll No. – 211MM1382
M.Tech
(2013)

Under the Supervision of

Prof. Archana Mallik

Department of Metallurgical & Materials Engineering
National Institute of Technology
Rourkela
2013

National Institute of Technology
Rourkela

CERTIFICATE

This is to certify that the thesis entitled, "**Mapping of structures and properties evolved during sono-electroplating of nickel thin films**", submitted by Madhusmita Moharana in partial fulfillment of the requirements for the award of Master of Technology Degree in Metallurgical and Materials Engineering at the National Institute of Technology, Rourkela is an authentic work carried out by her under my supervision and guidance.

To the best of our knowledge, the matter embodied in the thesis has not been submitted to any other University/ Institute for the award of any degree.

Supervisor

Prof. Archana Mallik
Dept. of Metallurgical and Materials
Engineering
National Institute of Technology
Rourkela- 769008

Date: 22/05/13

ACKNOWLEDGEMENT

With deep regards and profound respect, I avail this opportunity to express my deep sense of gratitude and indebtedness to **Prof. Archana Mallik**, Assistant Professor, Department of Metallurgical and Materials Engineering, National Institute of Technology, Rourkela, for introducing the present research topic and for their inspiring guidance, constructive criticism and valuable suggestion throughout in this research work. It would have not been possible for me to bring out this thesis without their help and constant encouragement. I am sincerely thankful to **Prof. B. C. Ray,** Professor and Head of Metallurgical and Materials Engineering Department and Prof. Archana Mallik for providing me necessary facility for my work and facilitating me the Electrometallurgical lab to continue my research work. I consider myself to be fortunate enough to have had opportunity to work under their guidance and enrich myself from their vast knowledge and analysis power. They will always be constant source of inspiration for me. I also express my sincere gratitude to Prof. A. K. Mondal, Chairman PGDAC to help us understand the administrative requirements and perform the same to fulfill the degree.

I also express my sincere gratitude to the department of ceramic (NIT, Rourkela), for giving me opportunity of using Atomic Force Microscopy (AFM). I am highly grateful to lab Members of Department of Metallurgical and Materials Engineering, N.I.T., Rourkela, especially Mr. S.Pradhan, Mr. S. Hembram, Mr. A. Pal and Mr. K.Tanti for their help during the execution of experiments.

Special thanks to my family members, all department members and all my friends of department of Metallurgical and Materials Engineering for being so supportive and helpful in every possible way.

I am also gratefully acknowledging the financial support of this work by the Department of Science and Technology (DST) India and National Institute of Technology (NIT), Rourkela for necessary infrastructure support.

Date: 22/05/13 **Madhusmita Moharana**

CONTENTS

List of Figures

List of tables

List of Publications

1. **Madhusmita Moharana**, Archana Mallik, *Nickel electrocrystallization in different electrolytes: An in-process and post synthesis analysis*, **Electrochimica Acta** 98 (2013) 1-10.
2. **Madhusmita Moharana**, Archana Mallik, *A study of structural and property relationship in electroplated Nickel thin films bath type variations*, **5th National Symposium for Materials Research Scholars MR-13,** 9-10th May, 2010, IIT Bombay, 2013 (Oral presentation).
3. **Madhusmita Moharana**, *One day workshop on Advanced Characterization Techniques*, **5th National Symposium for Materials Research Scholars MR-13**, 8th May, 2010, IIT Bombay, 2013.
4. **Madhusmita Moharana**, Archana Mallik, *Mapping of residual stress evolved during electroplated and sono-electroplated Ni thin films*, **Journal of The Electrochemical Society** [Communicated].

ABSTRACT

Nickel and its alloy films have versatile applications including metal coatings for its high strength, surface finishing and corrosion resistance, use in microelectronics, integrated optoelectronics and data storage technologies also used in decoration, electroplating industry and protection industries. Most properties of thin films are influenced by some factors such as crystalline structure, texture, or internal/residual stresses. The present research revolves around the residual stresses evolved during film synthesis. Residual stresses are stresses that remain after the original cause of the stresses (external forces) has been removed, which can have strong effects on film performance. These stresses are basically caused by interface coherency, thermal cycling and change in deposition parameters. Hence an understanding of the evolution of the same during synthesis will be a great avenue to thin film technologists. In the present study, an emerging technique sono-electroplating (electroplating plus ultrasound), has been used to synthesize Ni thin films at room temperature for four different electrolyte baths i.e. sulphate, chloride, Watts and sulphamate. And the aim of this study is to find the effect of ultrasonic vibration on evolution of residual stresses along with analysis of various parameters and properties including hardness, stress, surface finish and basic behavior of the depositing system in terms of cyclic voltammetry and chronoamperometry. The in-process analysis includes the electrochemical techniques and post-synthesis analysis followed by morphological studies includes SEM, AFM, XRD, hardness, residual stress and film thickness from surface profilometer. The same is solicited for electroplated and sonoelectroplated nickel thin films in four different aqueous solutions. The deposition and dissolution processes has been performed on electrocrystallized Ni in four types of baths i.e. sulphate, chloride, Watts and sulphamate baths, were analyzed by cyclic voltammetry (CV) technique. Also the micrographs of these processes have been obtained from the SEM analysis for Watts bath. The deposit from the bath with ultrasound gave a smoother surface from chloride, sulphate, Watts to sulphamate bath. Hardness value was found to be increased from 0.482, 0.814, 1.402, and 1.645GPa to 0.965, 1.137, 1.751 and 1.840GPa respectively for chloride, sulphate, Watts to sulphamate bath for silent and ultrasound conditions. The thickness of all the films is below 2.670μm for silent and 3.740μm for ultrasonic condition. The residual stresses of the deposits were reduced with an ultrasonically agitated bath. The residual stress was found to be compressive irrespective of deposition condition and is found

to be increased but tensile stress is found to be reduced in the presence of ultrasound. The result indicates that ultrasound has a definite impact on the deposit characteristics.

Keywords: Thin films, Electrodeposition, Sonoelectrodeposition, Residual stress, Nickel, Low temperature, Kinetics, SFM, Hardness, Surface profilometry, Nucleation, Grain growth, Surface analysis.

CHAPTER –1

Introduction

Introduction
Research motivation
Objectives
Thesis outline

1.1. Introduction

The current trend in technology is to make everything smaller and faster. Now it is not only standard to have a personal computer at both work and home, but computers can even be found in our vehicles and in the form of cell phones and personal digital assistants (PDAs). This all is possible with the nanotechnology. Electrodeposited Nickel has been used for various applications, such as decorative coating, service apparatus, and functionally suitable metal coatings for its high strength, surface finishing or good smoothness. Due to the ferromagnetic property, electrodeposited Ni is widely used in the fields of microelectronics, integrated optoelectronics, data storage technologies, and micro electromechanical system (MEMS). It is used in computer read and writes heads, computer memory chips etc. Electroplating of Ni coatings is frequently used for corrosion protection of steel. All the above application depends on the properties, behavior and reliable performance of deposited thin film. The strength of coatings in electrodeposition can be improved by pulse voltage and the other is alloyed with hard elements. Residual stresses are stresses that remain after the original cause of the stresses (external forces) has been removed. On substrates are in a state of residual stress which can have strong effects on film properties and mechanical performance. These stresses are basically caused by interface coherency, thermal cycling and change in deposition parameters and also applications of films. Most properties of thin films are influenced by some factors such as crystalline structure, texture, or internal/residual stresses [1-3]. The knowledge of these parameters is of great interest for the understanding of the process involved or of the mechanical behavior of the films. The small length scales and reduced dimensionality associated with thin film microstructures can change the mechanical behavior of films relative to the bulk. One common example is the large residual stress often observed to develop in thin films during deposition.

Residual stresses are known to exist in thin films regardless of the type of deposition method [4-7]. There are many factors proposed to be playing a role in the creation of these stresses, e.g. thermal expansion mismatch of the film and the substrate material [8], atom incorporation into the growing film during deposition [7], lattice misfit with the substrate [9], variation of inter-atomic spacing with crystal size [10], recrystallization processes [11], microscopic voids [12], and phase transformations [13]. Moreover, the nature and magnitude of these stresses vary with the deposition method and post-deposition treatments. Residual stresses and their distribution are essential for the mechanical performance, structural

integrity and lifetime of the components. Excessive residual stresses in thin film may cause defect formation and delamination at the film–substrate interface, buckling of the films. Consequently the adhesion between the film and substrate will be affected by the stress in the film leading to decrease of the stability and reliability of the components and devices. Therefore, it is significant to understand origins of the stresses of the films and to control their magnitude. Abermann et al. [14] shows a complicated compressive-tensile-compressive (CTC) behavior in the development of stress with deposition and increased thickness. Tensile stress was predominant for nucleation. Initially, individual nuclei were under compressive stress due to the influence of surface stress. Tensile stress was then generated at coalescence of nuclei in a process often described as zipping to form grain boundaries. The third stage of the stress development is again compressive which explains as, adatoms diffuse into the grain boundaries [15, 16]. Residual stresses are one of the crucial parameters in thin films and coatings, which can affect both performances and surface integrity, since adhesion or cracking resistance can be strongly altered. Hence an understanding of the evolution of the same during synthesis will be a great avenue to thin film technologists. In the present study, an emerging technique sono-electroplating, coupling ultrasound with electroplating, has been used to synthesize Ni films at room temperature. And the aim of this study is to find the effect of ultrasonic vibration on evolution of residual stresses along with analysis of various parameters including hardness, surface finish and basic behavior of the depositing system in terms of cyclic voltammetry and chronoamperometry. Ultrasonic agitation increased the deposition rate and limited current density as compared to the deposits without application of ultrasound [17, 18]. The deposit from the bath with ultrasound gave a smoother surface, increased micro hardness and the residual stresses of the deposits were reduced with an ultrasonically agitated bath. The residual stress was found to be compressive irrespective of deposition condition and was found to be reduced in presence of ultrasound. Furthermore the hardness of the films increased with the impact of sonication. The results indicate that ultrasound has a definite impact on the deposit characteristics. However the study needs further critical analysis before drawing an assertive conclusion. This research will focus on mapping the evolution of intrinsic stress in the electrodeposited nickel thin films obtained by sono-electrodeposition on to the graphite substrates from various bath types including sulphate, chloride and watts. The internal stress in the thin films is measured by means of the substrate curvature method.

1.2. Research Motivation

Structural properties of metal thin films and alloy thin films are dependent on the concentration of the electrodeposition bath, deposition bath, temperature, current density and pH of the electrolyte. Residual stresses on substrates may have strong effects on film properties and mechanical performance. These stresses are basically caused by interface coherency, thermal cycling and change in deposition parameters and also applications of films. The aim of the project is to reduce the residual stress with the application of ultrasonic vibration. Also to investigate the various kinetic properties and structural properties for the Ni deposits for four different electrolyte baths.

1.3. Objectives

The overall objectives to be achieved in this study are:

1.3.1 Main objectives:

- **i.** Electrodeposition and sono-electroplating of nickel thin films by bath variation.
- **ii.** In-process and post synthesis analysis of deposited nickel thin films (during and after the deposition).
- **iii.** Stress evolution for both electrodeposited and sonoelectrodeposited Ni thin films.

1.3.2. Work during the project:

- **i.** Metal (Ni) thin film synthesis by electrodeposited and sono-electroplating method for four types of bath i.e. watts, sulphate, chloride and sulphamate.
- **ii.** Analysis of nucleation and growth kinetics from cyclic voltammetry and chronoamperometry technique.
- **iii.** Structural and compositional analysis by XRD, AFM, SEM and EDS.
- **iv.** Analysis of residual stress, film thickness, roughness by Stylus surface profilometer and AFM.
- **v.** Analysis of microhardness and nanohardness of Ni thin films by microhardness tester and Nanoindentation.

1.4. Thesis outline

The organization of the rest of the thesis is as follows:

Chapter 2 deals with the concept of electrodeposition and sonoelectrodeposition, their mechanism, applications, evolution of residual stresses both in manufacturing process and in thin films synthesis process, surface morphology changes with variation in bath type and brief review of literatures on nickel deposition.

Chapter 3 focuses on the brief description of Electrochemistry and Sonoelectrochemistry, the experimental setups, synthesis of the nickel thin films and the characterization tools used to characterize the fabricated samples. The electrochemical analysis includes the description of cyclic voltammetry and chronoamperometry which deals in detail the synthesis and in-process electrochemical analysis. The phase analysis study was described by the understanding of X-ray diffraction (XRD) technique. Morphological structural characterization is understood by the scanning electron microscope (SEM) and Atomic force microscopy (AFM) methods. The residual stress and hardness is understood from Stylus surface profilometer and microhardness tester.

Chapter 4 includes the results and discussion the characterization of the ultrafine particles along with structural properties study of the electroplated and sonoelectroplated Ni thin films for four different electrolyte baths i.e. sulphate, chloride, Watts and sulphamate baths. The cyclic voltammetry (CV) analysis has been performed on electrocrystallized Ni to understand the deposition and dissolution processes in four types of baths i.e. sulphate, chloride, Watts and sulphamate baths. This is also used to set the deposition potential and to study the electrochemical aspects. The chronoamperometry current transients are explained and analyzed which shows the nucleation and growth processes. XRD has been properly used for the phase identification. The surface morphologies are characterized by SEM and AFM. The analysis confirms the finer deposit with increasing Ni concentration. The residual stress, hardness is calculated from surface profilometer and microhardness tester.

Chapter 5 this chapter is entitled with conclusions which enlist the detailed results obtained from chapter 4. Finally a list of references has been included referred for the preparation of the thesis. However, the work needs further amplification to explore the structural properties of Ni thin films for the different baths.

CHAPTER –2

Literature survey

Introduction to stresses

Foundation of residual stresses in manufacturing processes

Residual stresses in thin films

Intrinsic stress generation mechanisms in thin films

Review on Stresses in electroplated and sono-electroplated thin films

Synthesis techniques for thin films deposition

Nucleation and growth mechanism of thin films

2.1. Introduction to Stresses

The stress resident inside a component or structure after all applied forces have been removed is defined as Residual stress. There are two types of residual stress one is the Compressive residual stress which acts by pushing the material together, and other is the tensile residual stress which pulls the material apart. Mathematically, tensile stress is positive and compressive stress is negative. Also stresses is defined as normal stresses which act perpendicular to the face of a material and shear stresses which act parallel to the face of a material as shown in Figure 2.1. In total there are 6 independent stresses at any point inside a material represented by σ_{ij} where 'i' is the direction of stress acting on the material and 'j' is the face the stress is acting on [17].

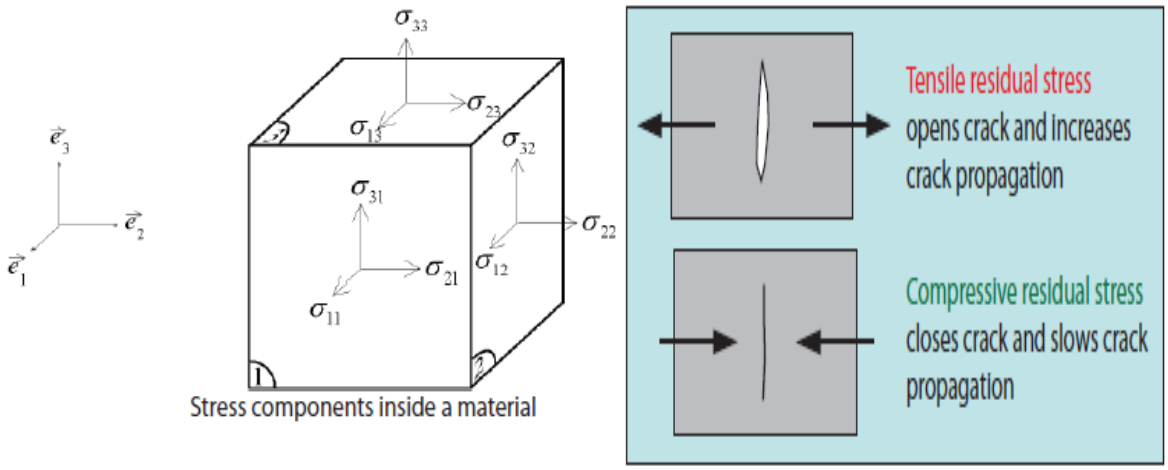

Figure 2.1: Showing the stress component inside a material[17].

When a material is plastically deformed by the applied mechanical loads, thermal loads or phase changes then residual stress are generated on the surface of the material [18-20]. Mechanical and thermal processes may also alter its residual stress state when applied to a component during service [19]. The total stress for the material within a component is equal to the residual stress generated plus the applied stress.

Total stress = Residual stress + Applied stress

Hence the knowledge in state of residual stress is important to determine the exact loads experienced by a component. In most cases, compressive residual stress is beneficial. It tends to increase slow crack propagation, fatigue strength and fatigue life, and increase resistance to environmentally assisted cracking such as hydrogen induced cracking and stress corrosion cracking [20-23]. But tensile residual stress in the surface is generally detrimental as it increases crack propagation and decreases fatigue strength and fatigue life, and also lowers the resistance to environmentally assist cracking [24, 25].

2.1.1. Types of Residual Stress

Residual stresses can be characterized on the basis of their existence within a material. Stresses that occur in major over a distance within a material are called as macro-stresses and stresses that exist only locally either between grains or inside a grain are called micro-stresses. The total residual stress inside a material is the sum of 3 types of stresses [25].

Type I Stresses: Macro-stresses occurring over distances within a material. These stresses vary within the body of the component over a range much larger than the grain size

Type II Stresses: Micro-stresses caused by differences in the microstructure of a material and occur over distances comparable to the size of the grain in the material. It can change sign and/or magnitude over distances comparable to grain size of the material under analysis. These stresses occur in single phase materials due to the anisotropic behaviour of grains, or in multi-phase material due to the presence of different phases.

Type III Stresses: These stresses exist inside a grain due to imperfections in crystal like presence of dislocations or crystal defects within the grain.

2.1.2. Importance of Residual Stress

Residual stress affects:

- Hydrogen initiated cracking (HIC) and Stress corrosion cracking (SCC)
- Low and high cycle fatigue performance
- Fatigue crack initiation and propagation (Damage tolerance)
- Fretting of material
- Material distortion
- Shot Peen forming (controlled distortion)

2.1.3. Management and Control of Residual Stress

There are many ways to introduce and manage residual stresses, among them: cold working techniques, such as shot peening, laser shock peening, ultrasonic peening, hammering, burnishing, low plasticity burnishing, rolling, coining and split sleeve expanding, can generate compressive residual stresses [26]. Hot working techniques, such as heat treatment, controlled cooling and localized heating are often used to minimize or reduce the magnitude of residual stress in components [27]. Tempering at around 1500C retains 50 - 60% of the residual stresses developed during quenching. Higher tempering temperatures greatly reduce

the surface compressive stress. Stress relief temperature around 6000C is used for mechanically deformed parts or, parts with tensile residual surface stresses. Dangerous level of residual tensile surface stresses may also be removed by gentle grinding on the surface [28].

2.2. Foundation of Residual stresses generation in manufacturing processes

Residual stresses and their optimization and interpretation represents a serious barrier to better materials fabrication, its processing and usage which effect the surface integrity and its service life [25, 29]. Hence considerable attention has focused on them. There is increased interest in optimizing designs to reduce residual stresses which is generated during the manufacturing of material process that gives reliable performance for all components of final products. Hence a better understanding by designers and manufacturing engineers are required to minimizing these unusual effects which is deliberately installed or coincidentally present after a manufacturing operation [21, 25, 27]. As factory-made product become additional subtle, sophisticated and significantly in industries wherever there are issues for user and public safety, and there's enhanced interest in optimizing designs to provide reliable performance from all parts of the ultimate product. This interest is also among concentrate on different aspects, like minimizing producing weight or prices. The natures of finished surfaces are crucial in managing potential mechanisms of wear, fracture and corrosion. In an ideal world, their understanding should be based on facts of the parameters of the component which also includes its residual stresses. The origin of residual stresses in manufacturing components are the result of non-uniform yielding, and are installed either deliberately (e.g. by peening), or as an unintended impact of a necessary process (e.g. mechanical forming, or heat treatment) [29, 31, 32]. Occasionally there are sources, such as carburizing in case hardened steels, or materials with dissimilar thermal expansion coefficients are joined as welded or brazed assemblies, or materials is present as an applied coating. In components, residual stresses are always in balance. This balance is disturbed by machining off which results a peened compressive layer from the surface. The balance is restoring by the remaining forces which redistributed to changes the shape of the component during the process. Also for the same reason, the arc height of an Almen strip is a quantitative measure of the stress, generated by peening effect of its faces, which is a measure of the stability of the peening process [25].

2.2.1. Residual Stresses from Manufacturing Operations

Residual stresses from manufacturing operation include heat treatment, conventional and non−conventional machining, welding and cleaning processes.

2.2.1.1. Heat treatment

Metallic components sometimes would like some form of heat treatment for component's better mechanical properties. In heat treatments involving quenching, it may be either to hold back precipitation or to promote hardening then the cooling rates at the surface are higher than at the center [25]. Only consideration of the volume change due to thermal gradient, at the start of cooling, the surface cools faster than the core. The difference in temperature between the core and surface increases upto certain time till it reaches an upper limit. As a result, soon the surface contracts more than the interior which creates a stress against the core. Since the core does not contract by the same amount thus a condition of compression in the core and tension in the rigid outer shell is observed. This stresses results in irreversible plastic flow between the core and surface. These residual stresses are presumably extended through the volume of the part, and are often referred to as body stresses [28].

2.2.1.2. Conventional Machining

In the past, numerous studies have been conducted to determine relationships between the cutting edge geometry, machining parameters and residual stresses. The processes like chip forming techniques resembling turning, drilling, broaching and sawing are traditional metal removal processes. There are many parameters which influence the residual stresses. Residual stresses in the machined surface and the subsurface are affected by workpiece, cutting tool, tool/workpiece interface, and cutting parameters, such as cutting speed, feed rate and depth of cut. The availability of coolant or lubricant at the points of contact, the original shape and developing wear of the tool and the precise orientation of the cutting edge under load many other events can radically change the near-surface residual stress pattern in the product. The nature of a surface conjointly includes its residual stress distribution, which may be measured and monitored throughout method development or tool proving; in post-production review and even while the part continues to be on the machine, with instrumentation [33−41].

2.2.1.3. Non-conventional Machining

"Non-conventional" machining processes include metal erode and removal methods that are increasingly finding applications replacing more conventional machining. Some of them are electro-discharge machining (EDM), plasma cutting and laser drilling and cutting which leave behind a re-solidified surface and a modified sub-surface layer of material that may require extensive characterization and subsequent processing. A process for the eroding and removing of material from electrically conductive materials by use of consecutive electric sparks is termed as Electric discharge machining (EDM). The causes of residual stresses during EDM processes are mainly due to metallurgical transformations and the non-homogeneity of heat flow or due to restricted area inhomogeneous plastic deformation, respectively [42]. Other processes includes are electro-polishing and electrochemical milling, may not even leave a residual stress field associated with the new surface. On the other hand, these surfaces will also be different from the conventionally produced surfaces they replace, and reflection should be given to developing, characterizing and applying a treatment to improve these surfaces for better mechanical properties [25].

2.2.1.4. Welding

There are many welding processes, from the "Thermite" process and gas welding, to manual and automatic arc welding, and electron beam and plasma welding. Also there are some modern techniques of friction welding and friction-stir welding. All welding processes normally attain a temperature of the materials to be joined to about or above their melting points. The materials to be joined are fuse together, and the source of heat is removed. As the heat is removed the temperature falls. Hence the cooling metal contracts which results in residual stresses that developed in and around the joint with or without local yielding. These stress causes distortion in the structure of the material. By stress-relieving heat treatments, the elevated temperature to the point at which the materials can flow to reduce the local stresses can be obtained. But it is rarely possible by thermal treatments alone, to completely remove residual stresses unless a phase change is involved. The residual stress fields in and around a weld are almost certainly three dimensional, and vary through the thickness of the material [25, 43].

2.2.1.5. Residual Stress during Casting

As in the case of quenched cylinders where phase transformation occurs, castings which undergo no phase transformation would normally have tensile stresses in the interior and compressive stresses at the surface. The situation however can get intricate through the following [28]:

(a) Mechanical self-control and restraint that a mould can offer as in permanent molding or die-casting

(b) Artificial cooling rates (i.e. chills) introduced into the casting

(c) Section-size of casting

Table 2.1 shows Main origins of residual stress resulting from different manufacturing processes. The different origins of residual stress for metal working operations usually carried out in the industry. To produce an industrial part, we can use one or several of the techniques listed in the table. To calculate the residual stress existing in a part, the source of the stress must be identified first

Table 2.1: Shows main origins of residual stress resulting from different manufacturing processes [25].

MANUFACTURING/THIN FILMS AND COATINGS/COMPOSITES (PROCESS)	ORIGIN MECHANICAL	ORIGIN THERMAL	ORIGIN STRUCTURAL
1. **Smelting** 2. **Casting**	No	Temperature gradient during cooling	Change of phase
1. **Shot-peening** 2. **Hammer-peening** 3. **Roller burnishing** 4. **Shock laser** 5. **Treatment** 6. **Bending** 7. **Rolling** 8. **Chasing** 9. **Forging** 10. **Straightening** 11. **Extrusion**	Heterogeneous plastic deformation between the core and surface of the part	No	No
1. **Grinding** 2. **Turning** 3. **Milling** 4. **Drilling** 5. **Boring**	Plastic deformation due to the removal of chips	Temperature gradient due to heating during machining	Change of phase during machining if the temperature is sufficiently high
Quenching without a phase change	No	Temperature gradient	Non
Surface quenching with a phase change (induction, EB, laser,	No	Temperature gradient	Change of volume due to a phase change

plasma, classical methods)			
Case-hardening Nitriding	No	Thermal incompatibility	New chemical component with D V
Welding	Flanging	Temperature gradient	Microstructural change (HAZ)
Brazing	Mechanical incompatibility	Thermal incompatibility	New phase at interface
Electroplating	Mechanical incompatibility	Mechanical incompatibility	Composition of plating depending on bath used
Hot spraying (plasma, laser, Jet Kote)	Mechanical incompatibility, micro-cracking	Thermal incompatibility, temperature gradient	Change of phase in plating
PVD, CVD	Mechanical incompatibility	Mechanical incompatibility	Change of phase
Composite	Mechanical incompatibility	Mechanical incompatibility	No

3.3. Residual stresses in thin films

Desirable or not, internal or residual stress is almost always going to be present in thin films. Stress may be present in thin films whether or not external loads are applied and may be due to a variety of reasons that are introduced during film deposition, which include: differential thermal expansion of the film/substrate, mismatches between the lattice parameter of the film and the substrate, atomic peening, incorporation of foreign atoms, microscopic voids, variation of interatomic spacing with crystal size, recrystallization processes, crystallite coalescence at grain boundaries and phase transformations [44-46]. Residual stresses are stresses that remain even after the original cause of the stresses (external forces) has been removed. Residual stress can have strong effects on film properties and mechanical performance. These stresses are basically caused by interface coherency, thermal cycling and change in deposition parameters [47-49].

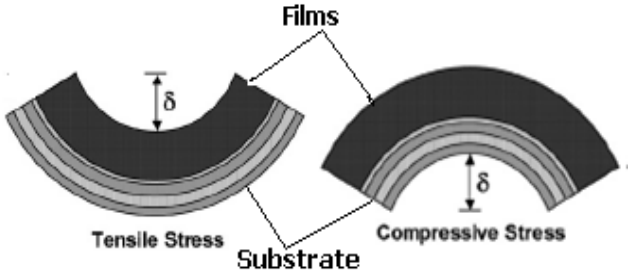

Figure 2.2(a): Schematic diagram of compressive and tensile stress [47].

The film 'wants' to be smaller or larger than the substrate allows it to be. Hence the film is in tensile stress (film 'wants' to shrink) or compressive stress (film 'wants' to expand) as shown in Figure 2.2(a). Large tensile stress may cause film delamination and / or cracking and debonding whereas excessive compressive stress can lead to film buckling [47]. Furthermore the application of the films and their properties like optical, electrical, magnetic, and functional properties is affected by the presence of residual stress [48]. Thus, understanding the origin of such stresses and controlling them is important for the reliable manufacture of such thin film system.

3.3.1. **Types of residual stresses in thin films**

There are three components of the residual stress devolved in thin film at a given temperature as shown in Figure 2.2(b). Magnitude of a residual stresses $'\sigma'$ can be expressed as

$$\sigma = \sigma_{th} + \sigma_i + \sigma_e \qquad (1)$$

Where σ_{th}= Thermal stress is due to the difference in thermal coefficient of substrate and deposited films, σ_i= Intrinsic stress is due to the intrinsic factors like lattice mismatch, presence of impurities etc. and σ_e= Extrinsic stress is due to the external factors. Residual stress in films can be either compressive or tensile as in Figure 2.2(c).

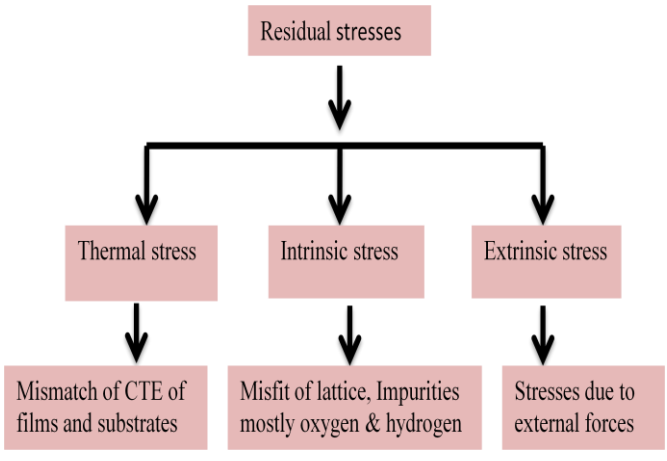

Figure 2.2(b): Classification of residual stresses in thin films and the causes

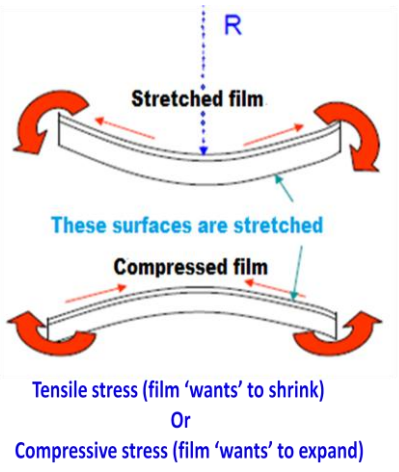

Figure 2.2(c): Residual stress in thin films can either be compressive or tensile.

If the stress is large enough, it could lead to fracture of the substrate, film or substrate/film interface. According to the theorem of minimum energy, the equilibrium state of an elastic solid body is when the potential energy of the system is at a minimum. For a system that is experiencing externally applied forces or residual stress, the system may find an equilibrium

position if rupture has occurred reducing the potential energy of the system [49]. Summarizing the theorem of minimum energy, the strain energy caused by residual stress may be reduced by the rupture or delamination of the film. In extreme cases tensile residual stress may lead to film cracking and peeling away from the substrate [50] and compressive residual stress may lead to film buckling and delamination from the substrate as shown in Figure 2.3(a) & 2.3(b). Besides the extreme cases just mentioned, residual stresses may also lead to the generation of crystalline defects, imperfection of epitaxial layers and the formation of film surface features such as hillocks and whiskers [51]. These less obvious results of residual stress may affect material properties such as magnetization, reflectivity and electrical conductivity [52, 35]. The residual stress can be measured by wafer curvature method. If the film thickness is far thinner than the substrate, the residual stress of the film is calculated by using the Stoney's equation [51] which is given by,

$$\sigma_f = \frac{1}{6}\left(\frac{1}{R_2} - \frac{1}{R_1}\right)\frac{E_s t_s^2}{(1-\upsilon_s)}\left[1 - \frac{t_f}{t_s}\right] \qquad (2)$$

Where, Es is that the Young's modulus. υ_s is that the Poisson's ratio of the substrate. R1 and R2 are substrate's radii of curvature before and after film deposition respectively. t_s is the thickness of the substrate and t_f is the thickness of the film.

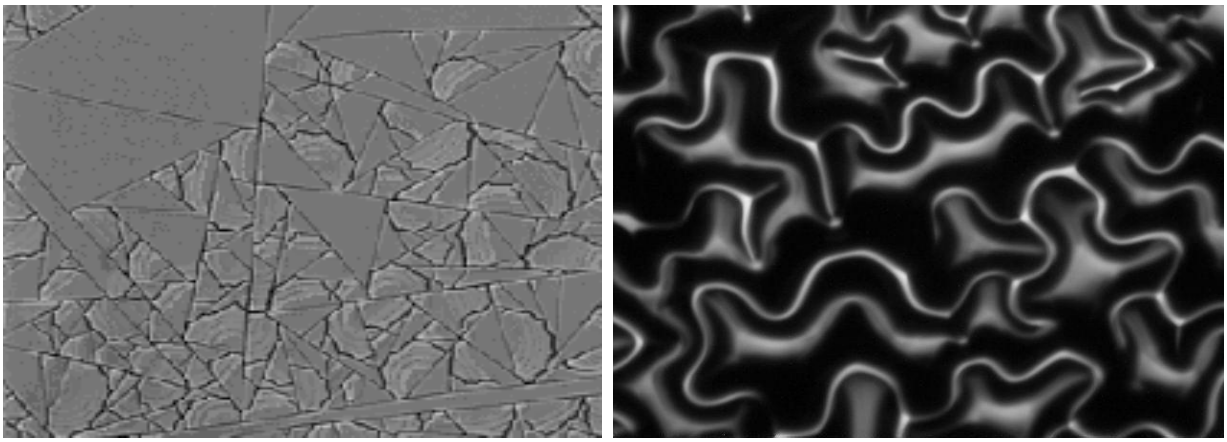

Figure 2.3: a) Low-k dielectric film in tension [50] and b) Tungsten film in compression [50].

3.3.2. **Origin of Residual stresses in thin films**

In 1978, Abermann printed the primary in-situ stress measurements on a growing film. These measurements had shown an advanced compressive–tensile–compressive (CTC) behavior within the development of stress during the deposition of nickel thin film. Grain growth of the larger grains at the expense of the smaller grains happens throughout the deposition

method. This development of the microstructure throughout deposition complicates finding the origin of the observed stresses in these films which is shown in Figure 4(a) [54−56].

i. 1st stage:

For the observed compressive stress throughout the primary stage of the deposition, two explanations are offered. One uses surface stress because for the initial compressive stress. The other uses an excess population of adatoms on the surfaces because of the initial compressive stress.

ii. 2nd stage:

Coalescence of the islands, "zipping", is employed as a mechanism to elucidate the incidence of tensile stress. In Figure 2.4(a) a pair of the method is illustrated. At coalescence of the individual grains, the grain boundary energy is less than the energies of two free surfaces, hence surface energy, at the expense of elastic energy of the film/substrate system, hence tensile stress within the film. By joining two formerly disjunction grains along, double the surface energy is traded for the grain boundary energy. This leads to the formation of sharp, cracklike features known as cycloid surfaces on the surface of the film. This result ought to be operative from the start of coalescence to the formation of endless film.

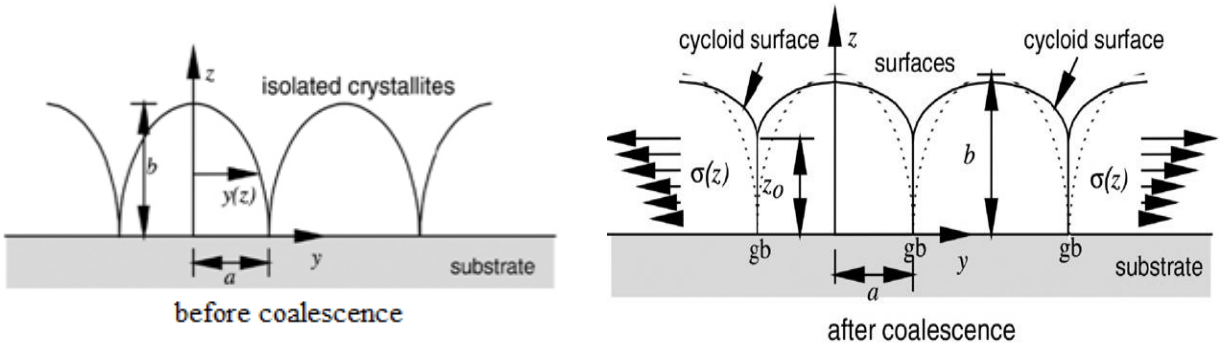

Figure 2.4(a) : Crystallite coalescence process, showing the elastic displacements and stresses [49].

iii. 3rd stage:

The third stage of the strain development is once more compressive. Here three explanations are offered. Within the 1st explanation, the surface stress on the highest of the film is held in order of the compressive stress within the growing continuous film. This can be constant surface stress that was additionally used to elucidate the initial compressive stress, however was masked by a tensile stress throughout the coalescence of the film. Within the second explanation, adatoms are incorporated between adjacent ledges on the surface of the growing film. Within the third explanation, adatoms diffuse into the grain boundaries.

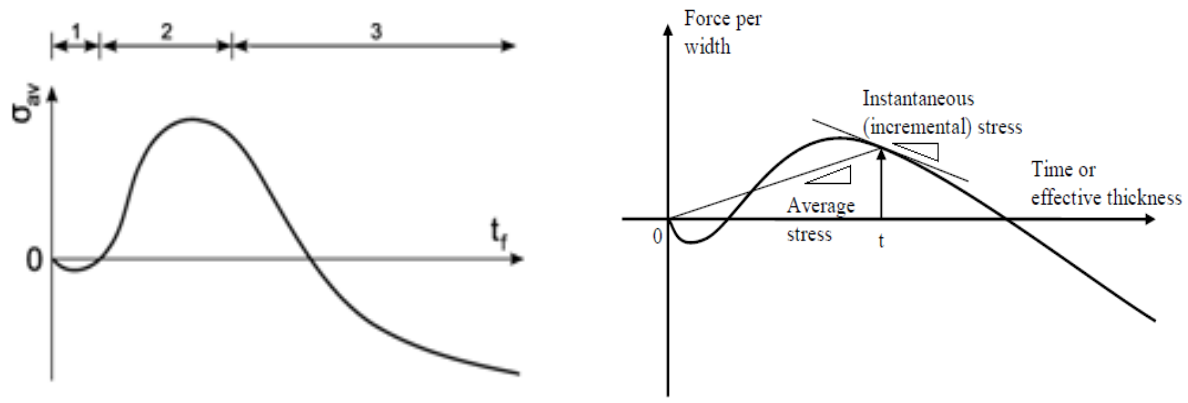

Figure 2.4(b): The three stages of film growth (compressive-tensile-compressive stress) for films at deposition temperature. Typical plot of force per width vs. time (or effective thickness). The average and instantaneous stress are indicated at the time or thickness of t [57].

Figure 2.4(b) shows the evolution of average film stress σ_{av} as a function of film thickness t_f during the deposition procedure. The curve describes the three stages of film growth (compressive-tensile- compressive stress) for films at deposition temperature. In-situ monitoring of the average stresses during deposition shows that the film thickness at which the change from tensile to compressive stresses occurs (between stages 2 and 3) depends strongly on the materials involved and can lie between a few nanometers and a few hundred nanometers.

3.4. The intrinsic stress generation mechanisms in thin films during the growth process

For intrinsic stress generation processes, there have been many studies of mechanical behavior of thin films in a variety of materials and under various conditions for the past few decades, and many mechanisms have been proposed in terms of surface/interface stress including island coalescence, grain growth, and incorporation of impurities or adatoms. However, the origin of stress generation is not yet well understood. Atomic mobility is one of the most important factors in determining the stress behavior during deposition, so studying the kinetics of stress changes responding to various process conditions may give useful clues for the stress generation mechanisms. In this section it describes the general stress behaviors during the deposition of Volmer-Weber thin films, and then an overview of some important mechanisms proposed to explain the intrinsic stress generation during film deposition.

3.4.1. **The general stress behavior during Volmer-Weber thin film growth**

In many polycrystalline thin film deposition, Volmer-Weber (VW) growth mode is usually found to be seen common. Initially small isolated 3D clusters are nucleated on a substrate and then grow into larger islands during VW growth mode. During islands grow, individual island come together and contact each other and finally coalesce into a continuous film. Numerous experimental studies were carried out on many material systems under various deposition conditions in order to understand the stress behavior of VW films [58-60]. The stress behaviors of VW thin films were classified by Abermann into two types [61]. The stress behavior of each type is shown in Figure 2.5. The curve of type I is generally seen in high melting point (or low mobility) materials, such as Si, Cr, Fe, W and Ta. In these materials only tensile film stress is developed with increasing thickness during growth. When there is a saturation point of growth, the final film stress usually does not change or changes only slightly over time. The curve of type II is observed in low melting point (or high mobility) materials, such as Al, Ni, Ag, Au and Cu. The microstructure of the deposited films generally shows equiaxed columnar grain structure (Figure 2.5(b)). A small compressive stress develops initially during deposition, followed by a tensile stress evolution for type II materials. Then this tensile stress soon reaches a maximum value and subsequently decreases to a net compressive stress. Hence after deposition of thin films the stress can be either net tensile or compressive stress depending on many factors including mobility of the film material, final stress during the deposition and final film thickness. Fascinatingly, when the growth is resumed the stress quickly returns to the value at which the growth was stopped and the film stress develops as if there were no interruption during growth [62]. Abermann found that the maximum tensile stress occurs at the thickness at which the film becomes completely continuous [63]. This statement suggests a strong correlation between stress and microstructure evolution in thin films. After the microstructure in films becomes continuous, the stress decreases to net compressive stress, indicating that this decrease is not just stress relaxation but the result of compressive stress generation. Hence the compressive stress generation mechanism seems to be suppressed in low mobility materials. The stress behavior transitions from type I to type II [64-67], which are observed at increased temperature because the diffusivity of an atom increases with temperature. Many mechanisms have been suggested in order to explain the origin of the tensile stress and compressive stress generation during thin film growth. Typical stress-thickness vs. thickness plots during Volmer-Weber thin film growth is shown in Figure 2.5(c) which shows the stress developed during various stages of deposition [62].

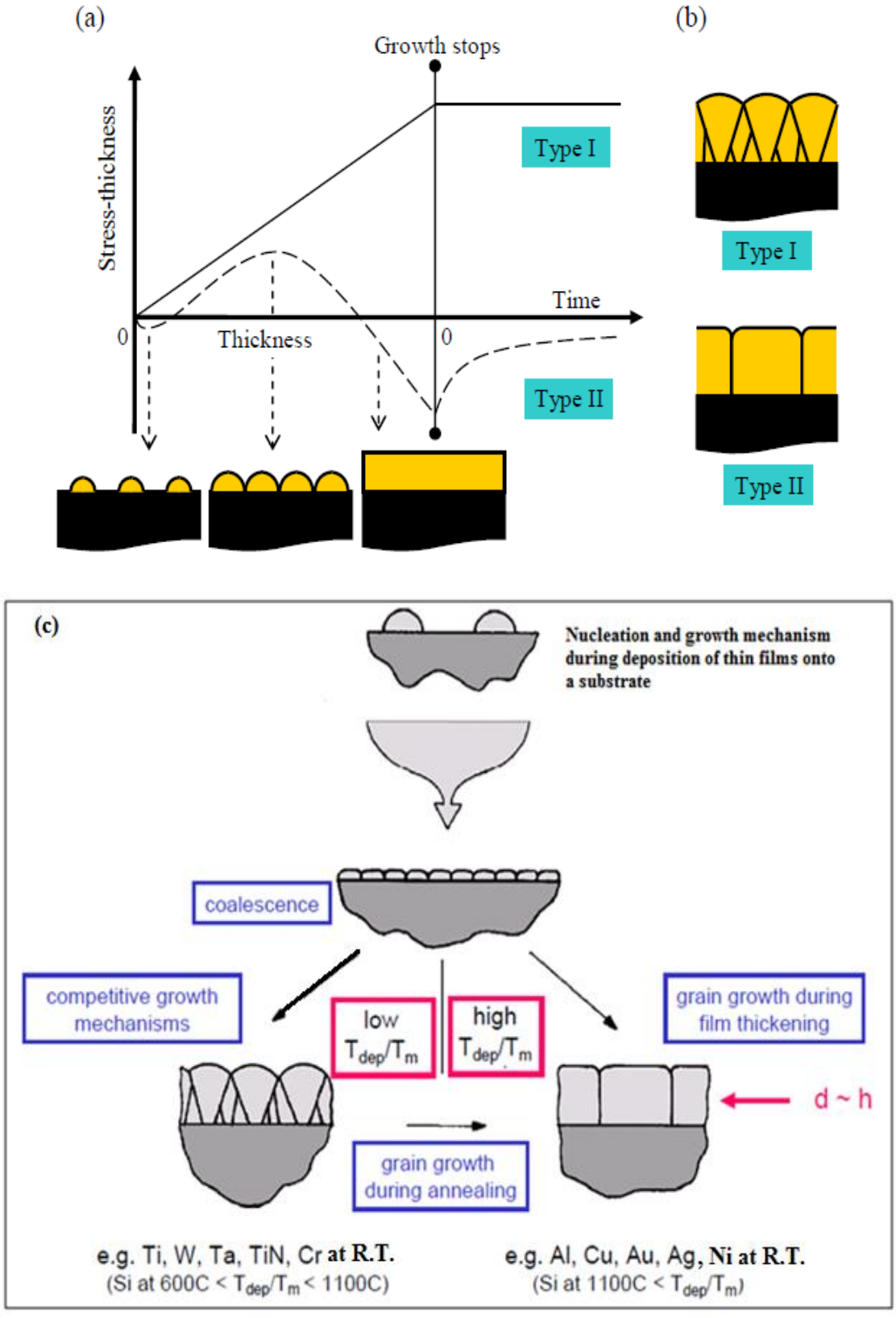

Figure 2.5: Typical stress-thickness vs. thickness plots during VW thin film growth. (a) Solid line shows the stress evolution of type I materials and dashed line shows the stress evolution of type II materials. Stress changes after growth are also presented as a function of time. Microstructure evolution of thin films in type II is shown schematically for corresponding stage of stress evolution. (b) Microstructure of

continuous film is shown for each type. Thin film in Type I shows high aspect ratio columnar grain structure (longer in thickness direction) and thin film in Type II shows equiaxed columnar grain structure (c) Nucleation and growth mechanism of thin films [68, 62].

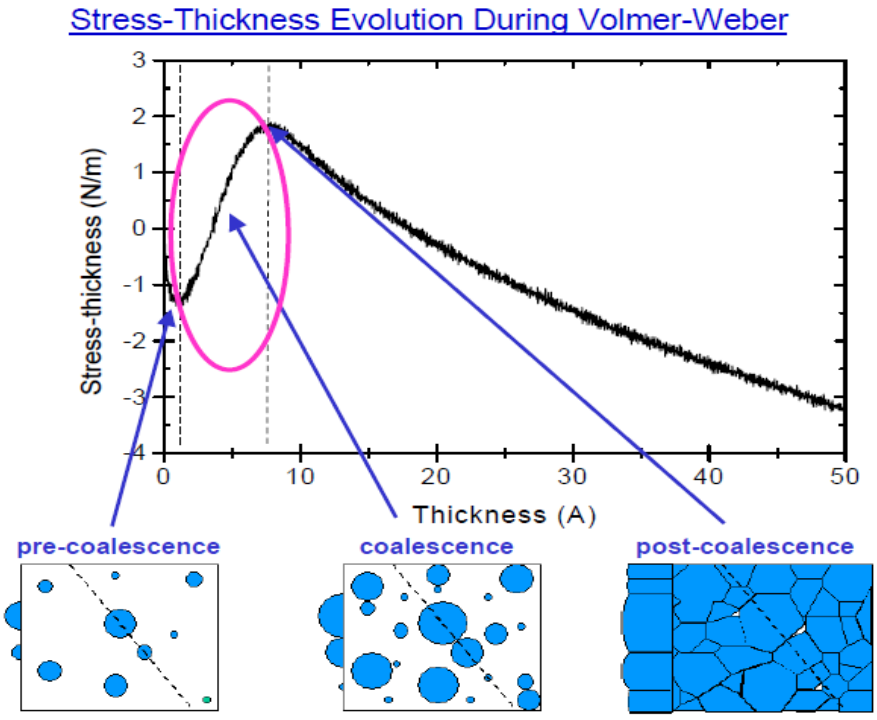

Figure 2.9: Typical stress-thickness vs. thickness plots during VW thin film growth showing the stress developed during various stages of deposition [62].

3.4.1.1. Early stage compressive stress generation in thin films by surface stress

In the initial stage of the deposition, the deposited material is present as individual islands resulting as a separate nucleation events. They appeal to the observation of compression of small spherical clusters by the action of the interface according to the Laplace formula. The lattice constant in a very small solid is different from the equilibrium value in the bulk material. This difference can be attributed to the effect of surface stress *f*. A stress on the surface can induce a pressure change in a solid. This pressure change is called the Laplace pressure and is equal to the difference between the pressure of the solid and the pressure of the surrounding vapor. At an equilibrium state, the work done by the surface stress *f* should be balanced by the work done by the Laplace pressure ΔP, so that the internal stress σ is given as follows for an isotropic spherical solid with radius *R*:

$$\Delta P dV = f dA \qquad (7)$$

$$\sigma = \Delta P = f\left(\frac{dA}{dV}\right) = \frac{2f}{R} \qquad (8)$$

Where, R = Radius of the particle

f = Surface or internal energy

ΔP = Compressive stress

Therefore, the change of the lattice constant in small solids can be calculated using the relationship between Laplace pressure and volume strain ($\Delta a/a$), where, a, is the lattice constant of the bulk solid:

$$\frac{\Delta a}{a} = \frac{2f}{R} \times \frac{(1 - 2\nu_f)}{E_f} \qquad (9)$$

Note that the volume strain disappears as the radius increases because the effect of surface stress is negligible in large dimensions. The change of lattice constant during island growth does not induce a stress as long as the island can move on the substrate. A basic assumption of the early stage compressive stress generation is that the island is firmly attached to the substrate when it is beyond the certain critical size (R_{cr}). The lattice constant of the island is locked down from that point and does not change on further growth. However, the equilibrium lattice constant will keep changing, approaching that of the bulk material during growth. Therefore, the difference of lattice constant between the equilibrium and the actual value will create an internal stress in the island, and the stress can be estimated by

$$\sigma = 2f\left[\frac{1}{R} - \frac{1}{R_{cr}}\right] \qquad (10)$$

This idea was first proposed by Laugier [69] without quantitative analysis. Abermann, Koch, and Floro *et al*. [70-72] have used this concept to explain stress behavior in their experimental data. Again the wetting angle, θ, of the particle on the substrate is determined by the young equation relating the surface interfacial energies.

$$\cos\theta = \frac{\gamma_s - \gamma_{is}}{\gamma_i} \qquad (11)$$

Where, γ_s= Surface energy of substrate

γ_i= Surface energy of island

γ_{is}= Surface energy of the island/substrate interface

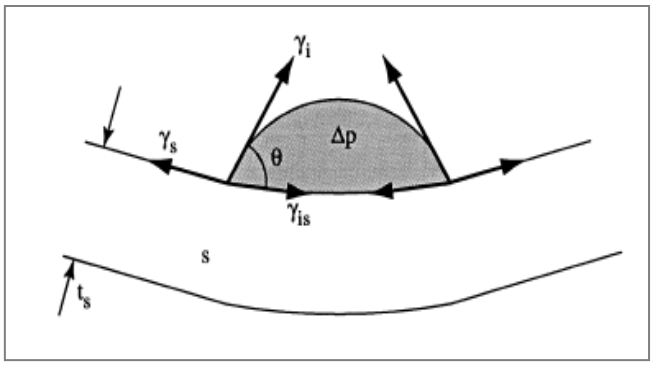

Figure 2.10: Schematic diagram of the substrate curvature resulting from the force action of the surface and interface stresses associated with an isolated island [73].

When the crystal structural of island and substrate are similar and lattice parameters are nearly equal then a low energy interface forms between them. The contact angle θ is then small. Some of the preferred nucleation sites for island growth formation are inclusions, grain boundaries, stacking faults and dislocations. Also during the early stages of nucleation, before the film has coalesced, the film stress is compressive. This has been attributed to the effect of surface capillary forces on the isolated cluster.

3.4.1.2. Tensile stress generation during thin film deposition due to coalescence

Tensile stress in thin films is inversely proportional to the average grain size. This proportionality rules out vacancy annihilation, pore elimination, and structural relaxation as cause for tensile stress in polycrystalline films. The general consensus for the origin of tensile stress generation is that the surface energy reduces by forming grain boundary at the expense of strain energy. Tensile stress caused by island coalescence in which the elastic strain energy is introduced and was driven by the energy reduction associated with creating a grain boundary segment from the solid-vapor surfaces of two neighboring grains. These surfaces will pull together to form a grain boundary when the grains are separated by a sufficiently small critical distance. Hoffman [74] and his colleagues developed the original concept, and Nix and Clemens [75] improved this idea with the crack closing process. Freund and Chason [76] suggested another model based on the theory of contact of elastic solids with cohesion in order to capture a more realistic process of island coalescence.

Hoffman assumed that when two isolated island surfaces are close enough they snap together spontaneously to form a grain boundary because this process can lower the total surface energy by $\Delta\gamma = 2\gamma_s - \gamma_{gb}$, where γ_s and γ_{gb} are the energy of an island surface and grain boundary, respectively. Hence tensile stress is a function of

$$\Delta\gamma = 2\gamma_s - \gamma_{gb} \qquad (12)$$

The maximum tensile stress is given by

$$\sigma_{max} = \left[\frac{-2M\Delta\gamma}{L}\right]^{1/2} \qquad (13)$$

Where, M is the biaxial modulus of the film and L is the grain size. From this model grain size increases then stress decreases. The average tensile stress decreases with increasing film thickness. From power law relation

$$\sigma_{av}(t) = 1.196 \times 10^7 (t^{-0.299}) \qquad (14)$$

Where, t is the thickness of the film.

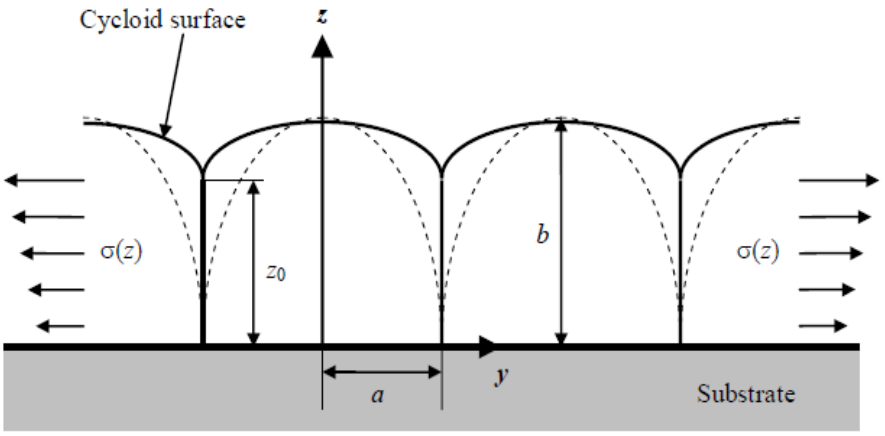

Figure 2.11: Schematic of island shape change before (dashed line) and after coalescence (solid line) [91].

The Nix-Clemens model for tensile stress generation is based on the same concept as the Hoffman model. However, in this model, they directly determined the tensile stress induced by coalescence from the amount of surface energy reduction, without estimating the separation between islands. Nix and Clemens recognized that the cracklike analysis for the stress evolution during the coalescence process, so they improved their model by using an elliptical shape island, which shows the characteristic of an elastic crack at the interface between islands as shown in Figure 2.11. The elliptical islands also lead to more realistic surface morphology inducing grain boundary grooving after coalescence. During growth, the islands do not interact until they contact each other. At the moment of coalescence, the grain boundaries "zip up", reducing the high energy surface area of islands until the magnitude of induced tensile stress is large enough to prevent the zipping up process. Freund and Chason approached this issue with the same general concept but with a different model for the zipping up process. In order to describe the zipping up process, they applied the theory of elastic contact of solids (Hertz contact theory) with cohesion.

3.4.1.3. Compressive stress generation in continuous thin film

For high mobility materials, a compressive stress develops when the films become continuous and the stress reaches a steady state during growth. During the compressive stress evolution, some dynamic behaviors are observed. The value of the compressive stress depends on growth conditions (e.g., growth rate, substrate temperature). There are four proposed mechanisms, which gives explanation for the compressive stress before the coalescence stage.

i. Compressive stress generation by surface stress

ii. Compressive stress generation by surface ledges

iii. Compressive stress generation by adatoms interaction with film surface

iv. Compressive stress generation by grain boundary diffusion

Cammarata *et al*. suggested that the compressive stress after the coalescence stage can also be explained by surface stress effects. During coalescence, a large tensile stress evolves rapidly associated with the grain boundary zipping. The increase of tensile stress will mask the intrinsic compressive stress developed by surface stress effects in the early stage of the growth. However, while the film grows thicker, the magnitude of the compressive stress also increases according to equation given below.

$$\sigma = (F + G)\left(\frac{1}{t} - \frac{1}{t_0}\right) + \beta H\left(\frac{1}{r} - \frac{1}{r_0}\right) \qquad (15)$$

Where *r* is radius; *t* is the thickness; F and H are isotropic surface stresses in the top surface and the curved surface, respectively. G is isotropic surface stress in the interface between the island and the substrate.

If we consider film thickening and grain growth together during film deposition, the intrinsic compressive stress will approach the value

$$\sigma_0 = -\frac{F + G}{t_0} - \frac{\beta H}{r_0} \qquad (16)$$

Nix and Clemens suggested that the tensile stress can be relieved by a local relaxation at grain boundaries through adatoms diffusion from the surface in high mobility materials. Cammarata suggested that the compressive stresses shown in continuous films may be the manifestation of the surface stress mechanism, which began prior to coalescence because the contribution of the tensile stress was reduced. During deposition, new atoms on the surface will create new layers and ledges quickly, increasing compressive stress. At interruption, the ledges will disappear by diffusion over a relatively large area, inducing tensile stress. This difference in diffusion processes explains the difference in stress change rate between growth interruptions and resumptions [77]. Secondly, Friesen *et al*. suggested that the adatoms can be incorporated between two adjacent ledges approaching each other. This process creates lattice interstitial defects in the film, increasing average compressive stress. As the compressive stress increases, the rate of atomic incorporation is reduced and finally the compressive stress reaches a steady state [78]. Chason *et al*. suggested a compressive stress generation mechanism based on atomic diffusion into and out of grain boundaries [79]. The main difference of this model from others is that the atoms are assumed to diffuse all the way down to the interface between the film and the substrate, so that the average stress changes depending on the growth conditions. The schematic of grain boundary diffusion of adatoms is shown in Figure 2.12. During deposition, the surface is in a nonequilibrium state, and the chemical potential on the surface is higher than it would be in equilibrium state. The increase in chemical potential may come from excess adatoms on the surface, nucleation of new

clusters, increased step density, surface morphology change, etc. The difference in chemical potential between the surface and the grain boundary acts as a driving force of atomic flow into the grain boundary. As atoms fill in the grain boundary, the stress in the film will increase; reducing the driving force by increasing chemical potential in the grain boundary, and finally steady state is reached when the chemical potential on the surface is equal to the chemical potential in the grain boundary.

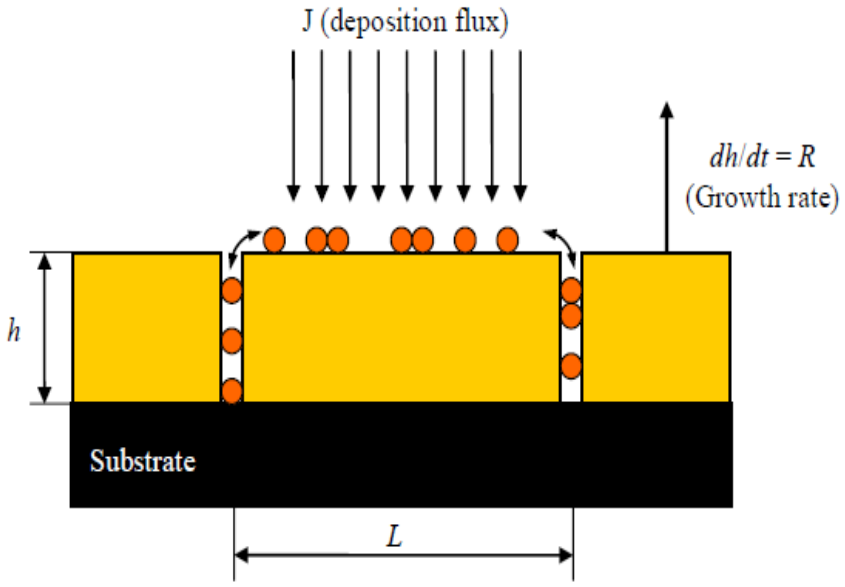

Figure 2.12: Schematic of grain boundary diffusion model. During growth, adatoms can diffuse into and out of grain boundaries because of a chemical potential difference between the surface and the grain boundary. *h* is the thickness of film and *L* is the grain size. The film grows at the rate of *R* [79].

3.5. A brief review on residual stress generation for both electroplated and sonoelectroplated metal thin films

Metallic thin films formed by a number of deposition processes often develop sizable intrinsic stress. Residual stress can drive post-deposition transformations such as whisker growth on the surface of thin films. Aside from any bulk lattice mismatch between the film and substrate, sources of stress in electrodeposited thin films include surface driven lattice parameter compression in individual nuclei, grain boundary formation when nuclei impinge, hydrogen evolution, precipitation of particles with molar volume different than the matrix, and incorporation of additives. There is some of the sited journal paper which gives a brief review on stress generation in various metal thin films which is listed below as a reference for further studies.

i. In 1975, work by L. Souzis and R. Weil [80], showed that the macrostresses were measured during the deposition of nickel monocrystals in all-sulfate electrolytes, either with no additives or containing coumarin or saccharinas additives. A high initial stress was observed for samples plated in the additive-free bath, which decreased hyperbolically with thickness. The variation in stress was observed due to the changes in the dislocation density with thickness. Also it was further found that such stress relaxation were seen which did not vary with thickness and this was not observed in samples plated in the presence of coumarin. For saccharin-containing baths, the stresses of samples plated were either zero, compressive or initially found to be tensile becoming gradual compressive with increasing thickness.

ii. In 1978, Pangarov and Pangarov[81] recapitulate the influence of important electroplating parameters on the stress and reported that in most of the cases, stress increases with the increasing of current density. Finegrained microstructures were obtained, and the nonequilibrium growth of the crystallites was favored due to the high current density. They also reported that the stress decreases with increasing bath temperature, because of the higher temperature the overvoltage of deposition get lowered and which favored the equilibrium crystal growth.

iii. In 1978, Lowenheim [82] explained the nature of stress of electrodeposited Ni with co-deposited or occluded hydrogen atoms and simultaneous gas evolution at the cathode. The residual stress decreases with the addition of a wetting agent which results from promoting hydrogen release from the electroplated Ni.

iv. In 1999, S.E. Hadian, D.R. Gabe [83] investigated on the electrodeposition of nickel and nickel–iron alloy on mild-steel and copper substrates from Ni/Fe and Watts baths. High current densities have been proved to bebeneficial in the case of surface appearances and adhesion, and also produced negligible internal stress values. Also the internal stress values of the Ni–Fe alloy deposits increased with an increase of Fe content in Ni–Fe solutions. Deposit from Watts solution shows a lower stress compared with Ni/Fe solutions and these stresses are compressive. The compressive stresses were larger when conventional plating was used with high current densities at a constant pH. The internal stress of the Ni/Fedeposits, which increased with an increase of the iron content, can be associated with decrease in the pH of plating, increase in the thickness of deposit, attributed to the lattice mismatch.

v. In 2002, work by Ghosh et al.[84] shows that the residual stress in the Ni-Cu alloy can be influenced by the deposition conditions, the compositions and the microstructures.

vi. In 2000, Basrour and Robert [85], has been reported that the stresses in the Ni deposits are very sensitive to operating conditions, such as bath temperature, pH, and current density[86–88]. Various theories accounting by J.K. Dennis and T.E. Such, for the origin of stress in electrodeposited thin films suggested that stress generated due to co-deposited hydrogen, the lattice misfit, crystallite joining, and dislocation theories [87]. They also observed that, one of the possible sources for residual stress is the defects of microstructure including grain boundaries and dislocations. Generally, defects like grain boundary and dislocations shows higher residual stress for the same composition thin film [88].

vii. In 2004,Takao Hanabusa, Kazuya Kusaka, Osami Sakata, showed that the residual stresses in the copper films were tensile in all cases.Thermal stress development was investigated in the heating and cooling processes. In the case of thick films, the internal stress decreased to the compressive side in an early stage of the heating process followed by non-linear behavior.In the cooling stage, the stresses in the film changed to tensile and increased to the final state at room temperature.The stress difference between the heating and cooling cycle was shown as a hysteresis loop in thick films [89].

viii. In 2004, the work by S.H. Kim, J.Y. Kim, J. Yu and T.Y. Lee showed that the residual stress of the electroplated Ni films depends under different conditions like current density, temperature, pH of bath, bath variation, concentration, deposition potential etc. For the pure Ni layer, residual stress can be controlled by adding a wetting agent and decreasing current density, and it is always under tensile stress. It shows that the residual stress in the film increases with increasing current density but decreases by adding a wetting agent or increasing the bath temperature. To reduce residual stress of the deposited layer, Ni should be electroplated at high plating temperature and low current density with the wetting agent. The Ni-Cu alloys of different Cu compositions from 20wt. %Cu to 100wt. %Cu were deposited with varying current density in a single bath. The residual stress was a strong function of current density and Cu composition. Decreasing current density and increasing Cu content simultaneously causes the residual stress of the metal layers to sharply decrease. For the pure Cu layer, the stress is compressive [90].

ix. In 2005, Okolo [91] and in 2006Yu et al.[92] have shown compressive stresses in Cu films, while in 2004, Hanabusaa et al.[93] and in 2007, Kima et al.[94] have observed tensile residual stresses in sputtered and electrodeposited Cu films respectively.

x. In 2013, Madhusmita Moharana and A.Mallik, showed that the residual stress developed during electrocrystallization of nickel is compressive-tensile-compressive in nature.residual stresses were analyised for four different baths i.e. sulphate, chloride, Watts and sulphamate and it was found that for sulphamate bath the nickel deposits have reudeced residual stress [95].

xi. In 1992, P. B. S. N. V. PRASAD, R. VASUDEVAN, S. K. SESHADRI, showed that stress measured for sample plating of nickel thin films from Watts bath with ultrasonic agitation produced lower stresses than that without ultrasonic agitation. It was obsereved that the stresses of the Ni deposits with a still Watts bath were tensile, whereas those with an ultrasonically agitated bath were compressive (near zero or slightly negative). With the application of ultrasonic agitation to the bath, the hydrogen is rapidly removed by vacuum bubbles, resulting in a smooth deposit. A reduced incorporation of atomic hydrogen in the deposit or substrate leads to lowered internal stresses [96].

xii. In 2003, A. Chiba, H. Haijima, K. Kobayashi , showed that the surface of vibration treatment was different compared to that of sonication and stationary states. Some cracks were observed on all the surfaces. It was estimated that Ni–B film was very hard, and was harder with sonication. The corrosion resistance was reduced. It was estimated that Ni–B deposited film had some cracks on the surface, and the cracks increased with sonication [97].

xiii. In 2011, A.Mallik and B.C.Ray[98] studied the effects of low deposition temperature on the state and level of residual stresses and grain size relation with the residual stress which was analyzed in sonoelectrochemically prepared copper thin films. It was found that the residual stress in the copper films was always compressive regardless of the film deposition temperature. Also with the increase of temperature, the grain size also increases and hence the residual stress increases.

3.5.1. **Effect of some electrodeposition parameter on the residual stress**

It is observed that the stress is dependent on many operating parameters including current density, temperature, film thickness and pH. The films plated at lower current densities and then it gradually increases with the increase in current densities up to some extent [99]. At higher temperature the grains rearrange and grow. If we increase the temperature of the bath then crystal size increases, but if we decrease the temperature of the bath the crystal size

decreases from micro range to nanorange. Due to the reduce grain size the residual stress decreases in thin film. It also observed that, residual stress in the nickel films was always tensile regardless of film thickness. The residual stress decreases with the increase in film thickness [100]. As the pH of the electrolyte increases the current efficiency, grain size and stresses in the deposit increases. It is related to decrease of hydrogen evolution reaction and hydrogen absorption [101, 102].

3.5.2. **Wafer curvature method of determination of residual stresses**

Thin films are usually in large planar geometry. Characterizations can be done without releasing the film and other particular preparations of the samples. The techniques include wafer curvature method to calculate the residual stress in thin films. Curvature measurements are frequently used to determine the stresses within coatings and layers. The deposition of a layer can induce stresses which cause the substrate to curve, as illustrated in Figure 2.5. The resulting changes in curvature during deposition make it possible to calculate the corresponding variations in stress as a function of deposit thickness. Curvature can be measured using contact methods (e.g. profilometry, strain gauges) or without direct contact (e.g. video, laser scanning, grids, double crystal diffraction topology). If the film thickness is much thinner than the substrate, the residual stress of the film can be calculated by using the Stoney's equation. It was originally derived for a beam flexed by a uniformly stressed film [103, 104], and was extended to determine two-dimensional film stress point-by-point from measured local substrate curvatures. For a uniform biaxial film stress, Stoney's equation is given by eq^{n} ,

$$\sigma_f = \frac{1}{6}\left(\frac{1}{R_2} - \frac{1}{R_1}\right)\frac{E_s t_s^2}{(1-\upsilon_s)}\left[1 - \frac{t_f}{t_s}\right] \qquad (17)$$

Where, Es is the Young's modulus.

υ_s is the Poisson's ratio of the substrate.

R_1 and R_2 are substrate's radii of curvature before and after film deposition.

t_s is the thickness of the substrate and t_f is the thickness of the film respectively.

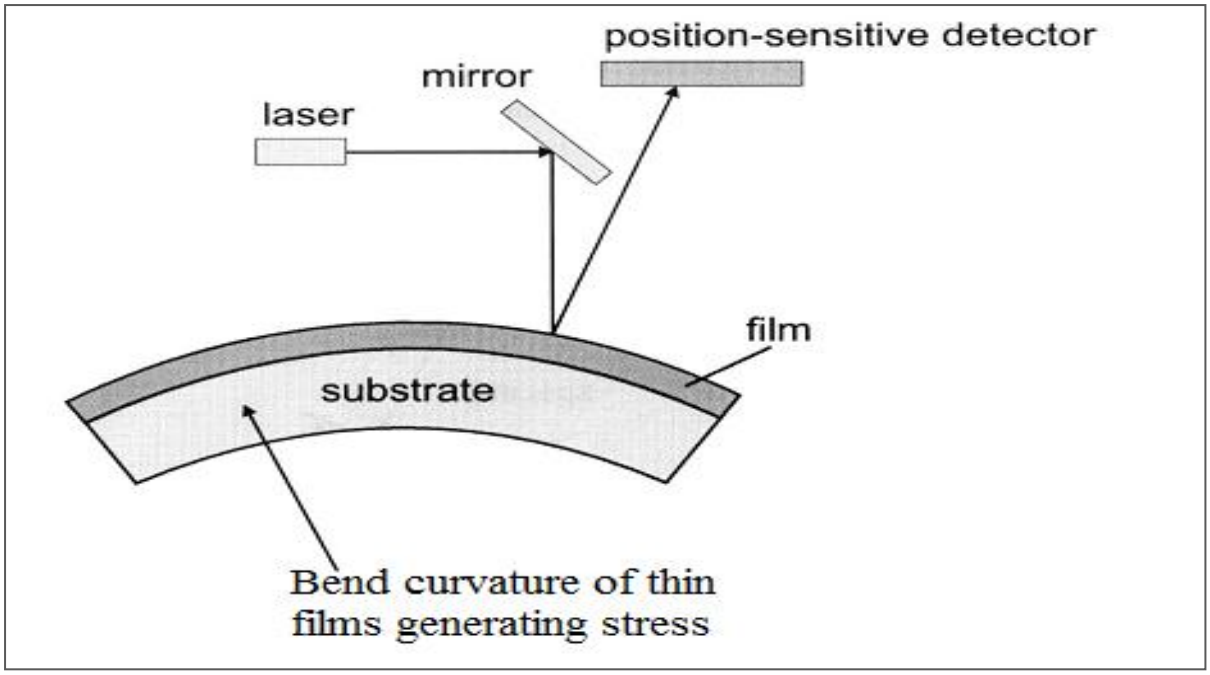

Figure 2.5: Wafer curvature method to measure stress in thin films [68].

3.6. Synthesis method for thin film depositions

The recognition that one may shield a surface from environmental attack is by the application of an inorganic, organic or metallic coating and thin films, so extending the life of the surface as well as the entire component or equipment, one of the major advances in the history of technology i.e. surface engineering. The most common reasons for altering the surface are to improve corrosion resistance, control friction and wear, alter dimension or to alter physical properties (reflection, color, conductivity). As applied to materials, surface engineering may be thin film coatings (like PVD, CVD, Molecular beam epitaxy, electrodeposition, sonoelectrodeposition), coatings or special surface treatments including processes such as thermal spray coatings, selective hardening, plating, diffusion treatments, hard-facing, high-energy treatments such as laser processing, and organic coatings such as plastic and paints laminates. The advances in thin film coatings have two approaches either in tailoring the microstructure or the thickness. The complication of the tribological properties of materials and the economic aspects of wear and friction justify an increasing research effort in bridging the fields of ultrafine-structured materials and coatings. Talking about thin films, these are the coatings with the thickness value below 1 μm and widely used in microelectronics, optics and solar cell systems. Thin films necessitate direct control of materials on the molecular and atomic scale, including surface deposition, modifications and structuring. There exists a

enormous variety of thin film deposition processes and technologies which originate from physical or chemical processes. Conversely deposition processes for applications in advanced surface engineering processes and microelectronics will be the most challenging and demanding approaches in the near future. The more important thin film deposition processes are based on liquid phase chemical techniques, gas phase chemical processes, evaporation methods and glow discharge processes. Typical processes are e.g. ion beam assisted deposition (IBAD) and plasma enhanced chemical vapor deposition (PECVD). Examples for novel thin film processing techniques, which are still under development, are pulsed laser ablation (PLD) and chemical solution deposition (CSD). These techniques enable the synthesis of complex thin film materials like complex oxides, carbides, and nitrides. The electrodeposition/sonoelectrodeposition of thin films is a viable alternative to vacuum-based deposition process, such as plasma deposition, sputtering or chemical vapor deposition. Its major advantages are its simplicity, that processing can take place at room temperatures and pressures, and that thin film properties can be controlled. The next section deals with the electrochemical deposition mechanism (electrocrystallization) which also includes approaches to understand the process towards fabrication of fine grained films.

3.6.1. **Electrodeposition technique**

Electrochemical metal deposition is one of the oldest subjects within the framework of electrochemistry. Metal electrodeposition takes place at electrode: electrolyte interfaces under the influence of an electric field. The occurrence of chemical changes due to passage of electric current through an electrolyte is termed as electrolysis and the deposition of any substance on an electrode as a consequence of electrolysis is called electrodeposition. The field of electrochemistry encompasses a massive array of different phenomena (e.g., electrophoresis and corrosion), devices (electrochromical displays, electro analytical sensors, batteries, and fuel cells), and technologies (the electroplating of metals and the large-scale production of aluminum and chlorine). In electrodeposition three electrodes is used and these are the working electrode, the counter and reference electrodes. The working electrode is the substrate on to which the metal deposition is done and it can be graphite plate, silicon, steel etc. The counter and reference electrode can be graphite rod or platinum electrode with 0.2 cm diameter and Hg/HgCl or Ag/AgCl (Saturated Calomel Electrode) respectively. The bath temperature was maintained at 298.15 K (25°C) for the deposition potential. For sonoelectrochemical experiment ultrasonic vibrator of frequency (20 KHz) was used, which

was positioned just below the electrochemical cell. The experimental setup arrangement for electrodeposition is shown below in Figure 2.6. The technology of electrochemical deposition of metals and alloys involves the reduction of ions from aqueous, organic, and fused salt electrolysis. The deposition of material species involves reduction of ions in the solution as $M_{Sol}^{Z+} + Ze \rightarrow M_{lattice}$.

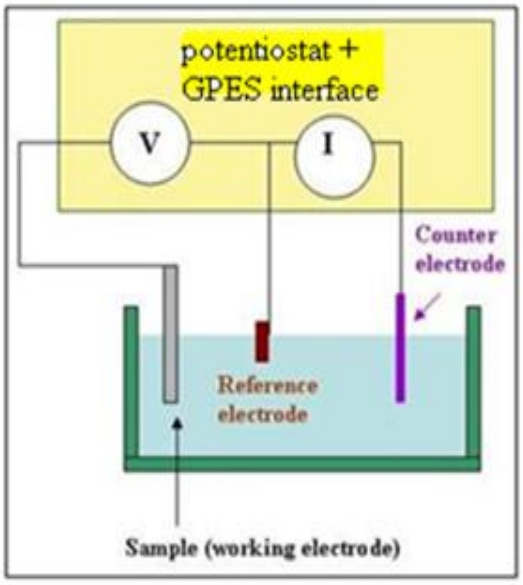

Figure 2.6: Experimental setup for electrodeposition methods.

The seemingly simple single reaction needs pre and post-complex steps before contributing to the whole deposition process. This is a reaction of charged particles at the interface between a solid metal and a liquid solution. The two types of charged particles, an ion and an electron, can cross the interface. Hence four types of fundamental areas are involved in the due process of deposition: (1) electrode-solution interface as the locus of deposition process, (2) kinetics and mechanism of the deposition process, (3) nucleation and growth processes of the deposits and (4) structure and properties of the deposits [105-107].

3.6.1.1. Advantages of electrodeposition process

- **a)** Selectivity and specificity (from the choice of electrode and potential)
- **b)** High sensitivity and low detection limit
- **c)** Ready to use compact instruments
- **d)** Capability in a single step process to produce metals, alloys and metal-matrix composites in various forms
- **e)** Speed and accuracy
- **f)** Ability to produce fully dense nanostructures free of extraneous porosity

g) Relatively low cost of application

3.6.1.2. Sonoelectrodeposition technique

Sonoelectrodeposition is quite similar to electrodeposition technique the only difference is an addition ultrasound agitation is given to the electrolyte. The experimental setup arrangement is shown below in Figure 2.7(a).

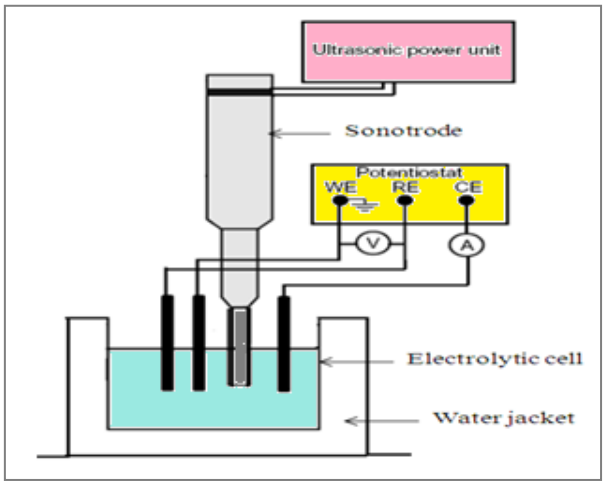

Figure 2.7(a): Experimental setup for Sonoelectrodeposition method.

Sonicated deposit shows uniform surface coverage, agglomerated grains and relatively finer grain size than silent deposits. This may be due to the homogeneous mass distribution in the interphase due to bubble breaking and bubble collapse effect of the cavitations phenomena associated due to coupling of ultrasound to the depositing bath. A keen observation of the deposit indicates the amount of agglomeration at higher deposition potential. Hence it may be assumed that ultrasound with higher potential has helped in proper distribution of the mass. Sonoelectrodeposition is an advance technique or method to get a uniform, stress free, high density thin film onto a substrate. Ultrasonic agitation increased the deposition rate and limited current density. The deposit from the bath with ultrasound gave a smoother surface and exhibited increased microhardness. The residual stresses of the deposits were reduced with an ultrasonically agitated bath [108].

3.6.1.3. Advantages of sonoelectrodeposition

Some of the advantages of sonoelectrodeposition over other techniques are:

a) Improves deposition rate

b) Increase current density

c) Increase smoothness of the surface

d) Reduction of residual stress on the film

e) Increase the microhardness of the film

f) No skilled operator required

g) Film thickness reduces

h) Reduces agglomeration

i) Dense deposition

3.6.1.4. Mechanism of Sonoelectroplating or Sonoelectrodeposition

Sonochemistry is the emerging study of chemical reactions powered by high frequency sound waves. Ultrasonic waves in liquids cause the formation of tiny bubbles that collapse so quickly, and with such enormous temperatures and pressures, that novel chemical reactions are generated. Chemists are using this unusual high-energy chemistry in many ways, such as creating inexpensive industrial catalysts, cleaning up polluted water, and zapping cancer cells. Sonochemistry is based on the effects of cavitations, the creation and collapse of bubbles in a liquid subjected to ultrasound.

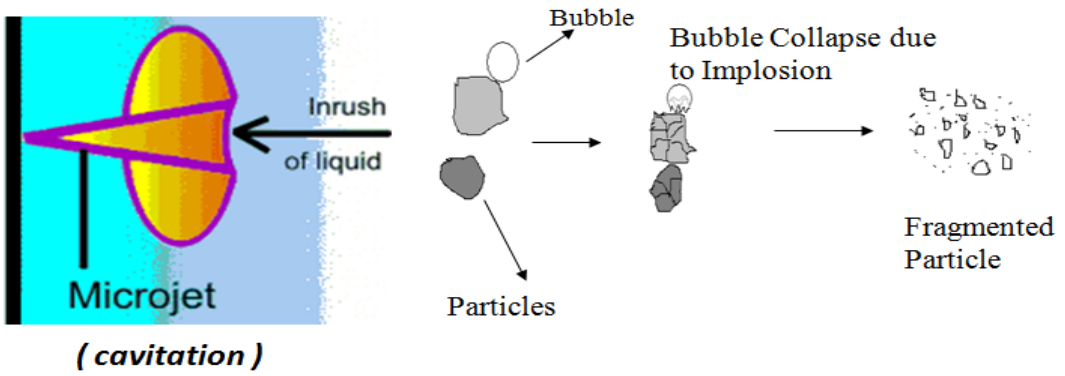

Figure 2.7(b): Mechanism of ultrasonic agitation [109].

Sound consists of alternating expansion and compression cycles traveling through a medium. Compression cycles push molecules together, while expansion cycles pull them apart. In a liquid, the expansion cycle of ultrasound can generate sufficient negative pressure to create bubbles, or cavities, in the liquid. Bubbles form at "weak spots", which are places where gases are either dissolved in the liquid or are trapped on contaminating particles. Even ultrapure liquids contain such weak spots. The importance of cavitations for Sonochemistry isn't so much how the bubbles form; rather, it is what happens when they collapse. At some point, a bubble can no longer absorb energy efficiently from the ultrasound, and it implodes. The rapid compression of gases and vapors inside the bubble creates enormous temperatures

and pressures. In addition to extreme temperatures and pressures, cavitational collapse also produces shock waves in the surrounding liquid [109]. These waves have important consequences for reactions involving liquid–powder slurries. Powders are typically too small to generate the jets of liquid created by extended solid surfaces, but the particles can be slammed together by a passing shock wave. The speed of impact is in the neighborhood of half the speed of sound. At these speeds, particles that hit each other directly can melt together. If the shock wave delivers a glancing blow, particles can abrade each other, smoothing each other's surface. This process can increase chemical reactivity of the powder by removing passivation coatings such as oxide which formed on the surface. The mechanism of sonoelectrodeposition is explained with a pictorial diagram in Figure 2.7(b).

3.7. Nucleation and growth mechanism for thin films

The analysis of current time transient is an important technique for studying the kinetics of electrocrystallization. The form of the current transient is a typical characteristic of an electrochemical nucleation and growth process. All transient exhibit a similar behavior; these are illustrated by a rapid decrease in current at very short time, which corresponds to charging of the double layer. This is followed by an increase in current due to the isolated growth of all individual nuclei and the increasing number of these nuclei present on the electrode surface. During this stage, the transport of electroactive species to nuclei formed on the surface occurs through hemispherical diffusion zones developed around each individual nucleus. As these grow, the coalescence of neighboring diffusion zones with localized hemispherical nuclei gives increase to a current maximum, followed by a decaying current, related to planer electrode diffusion. These features are consistent with nucleation of 3D hemispherical clusters followed by diffusion limited growth. According to Scharifker and Hill, the rate law for growth of 3D islands during electrochemical deposition is dependent on the mechanism of nucleation and growth. Analysis of early stages of nucleation, leads to two limiting cases. The two limited models are instantaneous or progressive three-dimensional nucleation with hemispherical diffusion-controlled growth of nuclei [110]. Instantaneous nucleation corresponds to a slow growth of nuclei on a small number of active sites, all activated at the same time. In this case all active sites available on the electrode surface are occupied in a very short time period after applying overpotentials and then, the nuclei only grow. Therefore instantaneous nucleation occurs when the nucleation rate is very high. Progressive nucleation

corresponds to a fast growth of nuclei on many active sites, all activated during the course of electroreduction. In this case nuclei are continuously formed during the whole time period at which overpotential is applied. Hence progressive nucleation will occur when nucleation rate is low [111, 112].

Table 2.2: Important results of Scharifker and Wills theory

S. no.	Instantaneous nucleation	Progressive nucleation
1.	$t_m = \left(\frac{1.2564}{N\pi kD}\right)$	$t_m = \left(\frac{4.6733}{AN_\infty \pi k' D}\right)^{1/2}$
2.	$I_m = 0.6382\, zFDc(kN)^{1/2}$	$I_m = 0.4615\, zFD^{3/4}c(k' AN_\infty)^{1/4}$
3.	$I_m^2 t_m = 0.1629\, (zFc)^2 D$	$I_m^2 t_m = 0.2598\, (zFc)^2 D$
4.	$\frac{I^2}{I_m^2} = \frac{1.9542}{t/t_m}\left\{1 - \exp\left[-1.2564\left(\frac{t}{t_m}\right)\right]\right\}^2$	$\frac{I^2}{I_m^2} = \frac{1.2254}{t/t_m}\left\{1 - \exp\left[-2.3367\left(\frac{t}{t_m}\right)^2\right]\right\}^2$

The proposed equation of Scharifker and Hill for 3D nucleation and growth are given in table, where D is diffusion coefficient, c the bulk concentration, zF the molar charge of the electrodepositing species, N the total number of nuclei, N_∞ number density of active sites, Im and tm current and time coordinate of the peak and k and k' are numerical constant. k and k' can be defined as

$$K = \left(\frac{8\pi cM}{\rho}\right)^{1/2} \qquad (18)$$

$$K' = \frac{4}{3}\left(\frac{8\pi cM}{\rho}\right)^{1/2} \qquad (19)$$

CHAPTER -3

Experimentation

Experimental Setup

Electrolytic bath preparation

Synthesis

Cyclic Voltammetry

Chronoamperometry

X-Ray diffraction (XRD)

Scanning Electron Microscope (SEM)

Atomic force microscope (AFM)

Stylus Surface profilometer

Microhardness Tester

3.1. Experimental Setup

The electrochemical analyses were performed in a conventional three-electrode cell using Potentiostat/Galvanostat (Eco Chemie Netherland, Autolab PGSTAT 12) interfaced with GPES software. The working electrode was a graphite electrode (Asbury, USA) with a surface area of 0.05 cm2, the counter and reference electrodes were a platinum electrode (with a surface area of 3.14 cm2) and Hg/HgCl (saturated calomel electrode) respectively. The electrochemical experiments were carried out with a three electrode arrangement whereby the potential relative to some reference electrode such as a saturated calomel electrode (SCE) or a silver/silver chloride electrode (Ag/AgCl), is scanned at a working electrode (graphite) and the resulting current flowing through the working electrode and the counter electrode (platinum electrode) is monitored in an electrolyte solution. The bath temperature was maintained at 298.15 K (25 ◦C). For sonoelectrochemical experiment ultrasonic vibrator of frequency (20 KHz) was used, which was positioned just below the electrochemical cell. The experimental setup arrangement is shown in figure 3.1(a) & (b).

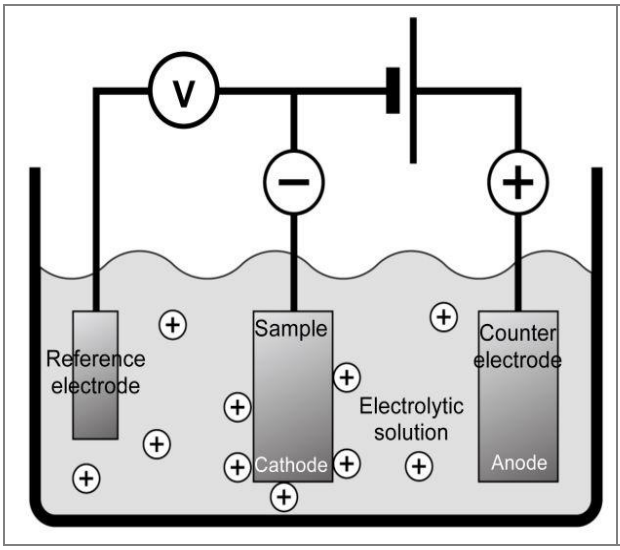

Figure 3.1(a): Schematic of a standard three electrode cell.

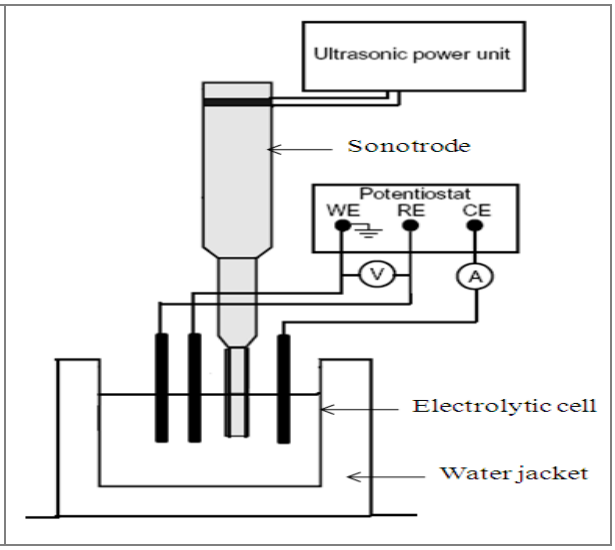

Figure 3.1(b): Experimental setup of sono-electroplating.

3.2. Electrolytic bath Preparation

The plating bath contains metallic salts used for making solution conductive. All chemicals were from commercial sources and were the highest purity available. They were used without further purification. Solution was prepared from an additive free chemical bath in doubly distilled water at room temperature and under moderate agitation. All solutions in this study

were prepared from doubly distilled water. Nickel thin films are deposited from four different electrolyte baths. The compositions of different baths for nickel deposition along with the operating parameters are given in the table below as Table 3.1.

Table 3.1: Compositions of the four types of bath

Chemicals used for the solutions	Sulphate bath	Chloride bath	Watts bath	Sulphamate bath
	Electrolyte Composition (gmL^{-1})			
Nickel sulfate, $NiSO_4.6H_2O$	240	-	240	
Nickel chloride, $NiCl_2.6H_2O$	-	240	45	15
Nickel sulphamate, $Ni(SO_3N_2)_2$	-	-	-	300
Boric acid, H_3BO_3	30	30	30	30
	Operating Conditions			
Temperature (˚ C)	25˚ C	25˚ C	25˚ C	25˚ C
Agitation	Mechanical	Mechanical	Mechanical	Mechanical
Anodes	Nickel	Nickel	Nickel	Nickel
pH	4.0	4.0	4.0	4.0

3.3. Synthesis

Electrodeposition and Sonoelectrodeposition were used as a route to fabricate corresponding Nickel thin films. A potentiostatic mode is commenced for deposition. The laboratory setup for electrodeposition has an electrolytic bath maintained at a particular composition with cathode and anode immersed in the bath. And also for Sonoelectroplating it has the same arrangement as for electrodeposition but with an additional ultrasonic horn inserted into the electrolyte cell. Temperature is maintained at 25°C and pH is maintained at 4. Cyclic voltammetry was performed in the potential range of +2.5 to −2.5 V versus SCE at a scan rate of 10 mV/s in all four types of baths. The bath temperature was maintained at 298.15 K (25 ◦C) and pH at 4 for all cyclic voltammetry analysis. The deposition was performed at −1.5 V potential with Chronoamperometry method. The structural morphology, crystallite size and lattice strain of Ni deposits were analyzed by SEM (JEOL JSM 6480 LV scanning electron microscope), AFM (Veeco di Innova) and XRD (PANalytical). The hardness property was analyzed by Microhardness tester, Nanoindenter, and the residual stress was analyzed by surface profilometer (Veeco Dektak 150). The measurements of nanoindentation were calculated from the Nanoindenter instrument which has a Berkovich (B–J 07) type of indenter embedded with a diamond tip. The key variables of the electrodeposition include

bath variation and Ni concentration present for four different baths for deposition with a constant deposition potential of -1.5V.

3.4. Electrochemical Analysis

The electrochemical phase formation is studied by methods including cyclic voltammetry (CV) and Chronoamperometry (CA). Here the basic principles underlying CV and CA are described, as they have been used in the analysis and synthesis of the nickel thin films. Schrifkar and Hills model of nucleation and growth are used to study the nucleation and growth mechanism.

3.4.1. Cyclic Voltammetry

The theoretical approach for cyclic voltammetry (CV) analysis was first given by Randles in 1938 [113]. Cyclic voltammetry is a versatile technique for investigating the electrochemical behavior of a system. The mechanism of redox and transport properties of a system in electrolyte solution is understood from the cyclic voltammetry study or analysis. It determines the potentials at which different electrochemical processes occur in the system. The effectiveness of CV is its capability for rapid observation of the redox behavior over a wide range of potential. It also investigates the role of adsorption, diffusion, and redox mechanism [114, 115]. The electrochemical experiments were carried out with a three electrode arrangement whereby the potential relative to some reference electrode such as a saturated calomel electrode (SCE) or a silver/silver chloride electrode (Ag/AgCl), is scanned at a working electrode (graphite) and the resulting current flowing through the working electrode and counter electrode (platinum electrode) is monitored in a electrolyte solution. A cyclic voltammetry is a display of current along x-axis versus potential along y-axis. The potential between working and reference electrode is scanned back and forth linearly with time between two extreme values. When the potential of the working electrode is more negative than that of the redox couple present in the electrolyte, the corresponding species may be reduced that is what the electrons flow away from the electrode and produce a cathodic current which corresponds to a cathodic peak. Similarly when the potential of working electrode is more positive than that of a redox couple, the corresponding species may be oxidized and produce an anodic current which corresponds to an anodic peak. In the current study, in each case, cathodic peak may correspond to either nickel deposition or

hydrogen evolution or both of the processes and anodic peak corresponds to the dissolution of deposited layer or other simultaneous anodic processes [116-118].

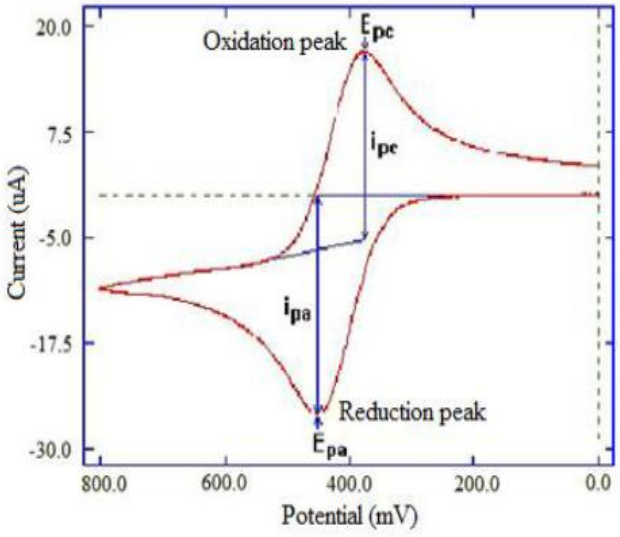

Figure 3.2: A typical cyclic voltammogram showing reduction and oxidation current peaks [96].

3.4.2. Chronoamperometry

Chronoamperometry (CA) is an electrochemical technique in which the potential of the working electrode is stepped and the resulting current from faradic processes occurring at the electrode (caused by the potential step) is monitored as a function of time. This i~t response is comprised of two components. The first is the current due to charging the double-layer and the other is due to the electron transfer reaction with the electroactive species. When the working electrode is immersed in the electrolytic solution, a very thin region called the double layer is formed at the electrode/electrolyte interface. The double layer contains a distribution of ions at the interface and is considered to work as a capacitor (C) that represents the electrode double-layer capacitance [119]. The current (i.e., electrons) flows to the working electrode (WE) in order to bring its potential to some desired value. A potentiostat with a 3-electrode cell provides the current via the auxiliary electrode (AE) to the WE while the potential is measured with respect to a reference electrode (RE). Of course, the extent to which both occur simultaneously depends on the initial, E_i, and the final value, E_f, of the potential. The Cottrell equation describes how the current, I, decays as a function of time, t as shown in the Figure 3.3. Under a diffusion-controlled rate conditions, the current decay is given by Cottrell law [120]

$$i = \frac{nFAD^{1/2}C^{b}}{(\pi t)^{1/2}} \qquad (20)$$

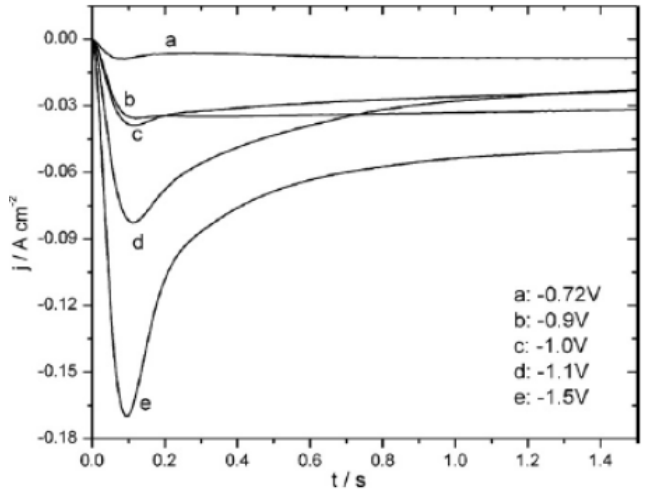

Figure 3.3: Chronoamperometry (Current-time transient) Curve [102]

where n is the number of electron(s) transferred per electroactive molecule or ion; F is Faraday's constant; A is the area of the electrode surface in cm^2; D is the diffusion coefficient in cm^2/s; C^b is the concentration of the electroactive species in mol/cm^3; and t is time in second. The current raises rapidly to a maximum value decays as a function of $t^{1/2}$ according to eq^n (20).

3.5. Characterization Technique

Several techniques have been used to characterize the electrodeposited and sonoelectrodeposited thin films. Details of some of the techniques are enlisted below. The technique used in this study includes XRD to analyze the phase, crystallite size and lattice strain, Surface profilometer, Microhardness tester and Nanoindenter to analyze the structure and properties of deposits (residual stress and hardness). The microstructure studies of the deposits were done by SEM and AFM for various electrolyte baths. The AFM analysis also reflects about the average grain size and the roughness. The chemical composition/purity of the deposited films was determined by energy dispersive spectroscopy (EDS) analysis.

3.5.1. X-Ray Diffraction (XRD)

X-ray diffraction line profile analysis is an adopted technique, powerful tool and nondestructive method, to characterize the behavior of different materials. It reveals

information about the crystallographic structure, lattice parameter, interplanar spacing, phase analysis and physical properties of materials and thin films. XRD is a technique used to characterize the crystallite size, lattice strain, crystallographic structure and preferred orientation in polycrystalline or powdered solid samples. XRD techniques are based on the elastic scattering of X-rays from structures that have long range order. An effect of the finite crystallite sizes is seen as a broadening of the peaks and strain in an X-ray diffraction as is explained by the Williamson-Hall formula. The X-ray diffraction, in the range of scanning angle 40-100° at a scanning rate 2° with CuKα radiation with λ=1.5406Å, using (PANalytical) Philips X' PERT System X-Ray Diffractometer. An effect of the finite crystallite sizes is seen as a broadening of the peaks and strain in an X-ray diffraction as is explained by the Williamson-Hall formula [121].

3.5.2. Scanning Electron Microscope (SEM)

Film morphology and composition is obtained by JEOL 6480 LV scanning electron microscope (SEM) equipped with an energy dispersive X-ray detector of Oxford data reference system. The micrographs were taken at low acceleration voltages of 15 or 20KV for best possible resolution from the surface rather than the interior of the deposits. The Scanning electron microscope images the sample surface by scanning it with a high-energy beam of electrons in a raster scan pattern. The interaction between the electrons and the atoms of the sample produces signals that contain information about the elemental composition, sample's surface topography, morphology of the sample surface and other properties such as electrical conductivity. The different types of signals produced by an SEM include back-scattered electrons (BSE), secondary electrons (SE), characteristic X-rays, light as cathodoluminescence, specimen current due to electron movement and transmitted electrons. The signals result from interactions of the electron beam with atoms at or near the surface of the sample. Back-scattered electrons (BSE) are beam electrons that are reflected from the sample by elastic scattering. Characteristic X-rays are emitted when an incident electron beam excite and removes an inner shell electron from the sample then an electron from an outer, higher-energy shell fills the vacancy, and the difference in energy between the higher-energy shell and the lower energy shell, releasing enormous energy which may be in the form of an X-ray. And with a help of energy dispersive spectrometer, the number and energy of the X-rays emitted from a specimen can be measured. This energy is in the form of X-rays called characteristic X-rays that are used to identify the composition and measure the abundance of

elements in the sample. Energy dispersive X-ray spectroscopy (EDS or EDX) is an analytical technique used for the elemental analysis or chemical characterization of a sample [122, 123].

3.5.3. Atomic Force Microscopy (AFM)

Atomic force microscopy (Veeco di Innova) is a type of microscopy technique used to characterize surfaces at very high resolution. The high resolution images are formed due to the mechanical movement of the probe in raster scan of the specimen i.e., in a serial fashion at discreet locations (pixels). The main aim of the AFM technique is to measure the forces acting between a fine tip and a specimen. The mechanism of AFM is a sharp probe or tip with conducting P(n) doped silicon is brought into close proximity with the sample to be analyzed the image with high resolution. A positive or negative bending of the cantilever results due to the attractive or repulsive forces which generally results from interactions between the tip and the sample surface. A laser beam, which is reflected from the back side of the cantilever, is used to detect the bending of the cantilever. In the contact mode the tip is scanned very close to the surface of sample. In this mode the interatomic force between the cantilever and the sample is repulsive which causes the cantilever to bend up and these forces increase as the probe begins to contact the surface. In the non-contact mode, the cantilever is held on a farther distance of the order of tens to hundreds of angstroms from the sample surface, and there is an attractive force between the cantilever and sample, largely a result of the long-range Vander Waals interactions. The AFM is capable of measuring nanometer scale images of insulating surfaces with little or no sample preparation as well as measuring the 2D and 3D images of surfaces and studying the topography. It also helps to analyze the substrate roughness and grain size, step formation in thin film epitaxial deposition, pin-holes formation or other defects in oxides growth. A significant advantage of AFM is that non-conducting surface imaging can be done, and hence it is very suitable for biological systems [124].

3.5.4. Stylus Surface Profiler

The Stylus Surface Profiler (Dektak 150) is the culmination of four decades of stylus profiler technology innovations. Surface Profilometer is a measuring instrument used to measure a surface's profile, in order to quantify its roughness. For a specified distance and specified contact force, a diamond stylus is moved vertically in contact with a sample and then moved laterally across the sample A surface profilometer can measure small surface variations in vertical stylus displacement as a function of position. It can measure small vertical features

ranging in height from 10 nanometers to 1 millimeter. The height position of the diamond stylus generates an analog signal which is converted into a digital signal stored, analyzed and displayed. The radius of diamond stylus ranges from 20 nanometers to 25 micrometers. The horizontal resolution is controlled by the scan speed and data signal sampling rate. The force of the stylus may range from less than 1 to 50 milligrams. The analysis was carried out in Dektak 150 surface profilometer at a force of 0.3 mg. It provides repeatable, accurate measurements on varied surfaces, from traditional 2D roughness surface characterization and step height measurements to advanced 3D mapping and film stress analyses. With its small footprint, latest generation technology and extensive add-on capabilities, the Dektak 150 enables superior performance, versatility and value for industry and research engineers.

3.5.5. Microhardness

Hardness is a characteristic of a material, not a fundamental physical property. It is defined as the resistance to indentation, and it is determined by measuring the permanent depth of the indentation. More simply put, when using a fixed force (load) and a given indenter, the smaller the indentation, the harder the material. Indentation hardness value is obtained by measuring the depth or the area of the indentation. The Vickers hardness test method, also referred to as a microhardness test method, is mostly used for small parts, thin sections, or case depth work. The Vickers method is based on an optical measurement system. The Microhardness tester (LM248AT, Leco), specifies a range of light loads using a diamond indenter to make an indentation which is measured and converted to a hardness value. A square base pyramid shaped diamond is used for testing in the Vickers scale. Typically loads are very light, ranging from a few grams i.e. 5 grams to 2 kilograms. The Microhardness methods are used to test on metals, ceramics, and composites, almost any type of material. In order to provide a small enough specimen that can fit into the tester. Additionally, the sample preparation will need to make the specimen's surface smooth to permit a regular indentation shape and good measurement, and to ensure the sample can be held perpendicular to the indenter [125].

CHAPTER -4

Results and Discussion

Electrochemical analysis (CV& CA)

2D and 3D nucleation and growth model

Surface characterization

Property analysis

Residual stress analysis

4. Results and discussion

The electrodeposition rate of Ni depended upon the composition of electrolytes, pH, bath temperature and ultrasonic frequency. The deposition rate increased with increasing pH, bath temperature, and concentration of $NiSO_4$, $NiCl_2$, whether ultrasound was present or not. The basic principle of CV and CA are described, as they have been utilized in the analysis and synthesis of the nickel thin films. The Several characterization techniques have been used to characterize the electrodeposits and sonoelectrodeposits of nickel thin film. The X-ray diffraction, in the range of scanning angel 40^0 to100° at a scanning rate 2° with CuKα radiation (λ=1.5406A^0) using Philips X' PERT System X-Ray Diffractometer. JEOL scanning electron microscope (SEM) at low acceleration voltages, atomic force microscope (AFM) were employed to examine the particle size, morphology, and microstructure of the electrodeposits and sonoelectrodeposits of thin film for the various bath types at constant temperature and potential. The chemical composition and purity of the electrodeposits and sonoelectrodeposits was determined by energy dispersive spectroscopy (EDS) analysis. Property analyses were carried on with the help of microhardness tester, nanoindentation and stylus surface profilometer.

5.2. Electrochemical analysis

The electrochemical analyses were performed with the help of cyclic voltammetry and chronoamperometry techniques. The thermodynamics and kinetics of the entire electrocrystallization process by cyclic voltammetry and chronoamperometry analysis is addressed as in-process studies.

5.2.1. Cyclic voltammetry

Cyclic voltammetry (CV) was carried out under silent and sonicated conditions in the potential range of −2.5 to 2.5V. Fig 4.1(a) & (b) shows the cyclic voltammetric patterns of electrodeposited nickel in four electrolytes i.e. sulphate, chloride, Watts and sulphamate, at a scan rate of 10 mV/Sec at silent and ultrasound conditions. In case of silent atmosphere, well resolved anodic and cathodic peaks are visualized but for sonication condition there is no such prominent cathodic peaks and the both anodic and cathodic peaks have greater intensity as compared with the same peaks for static or silent condition for all electrolytic bath types. However the position and intensity of peaks are different for all the baths as mentioned in Table−4.1 (a). In the current study, in each case, cathodic peak may correspond to either

nickel deposition or hydrogen evolution or both of the processes and anodic peak corresponds to the dissolution of deposited layer or other simultaneous anodic processes [116−118].

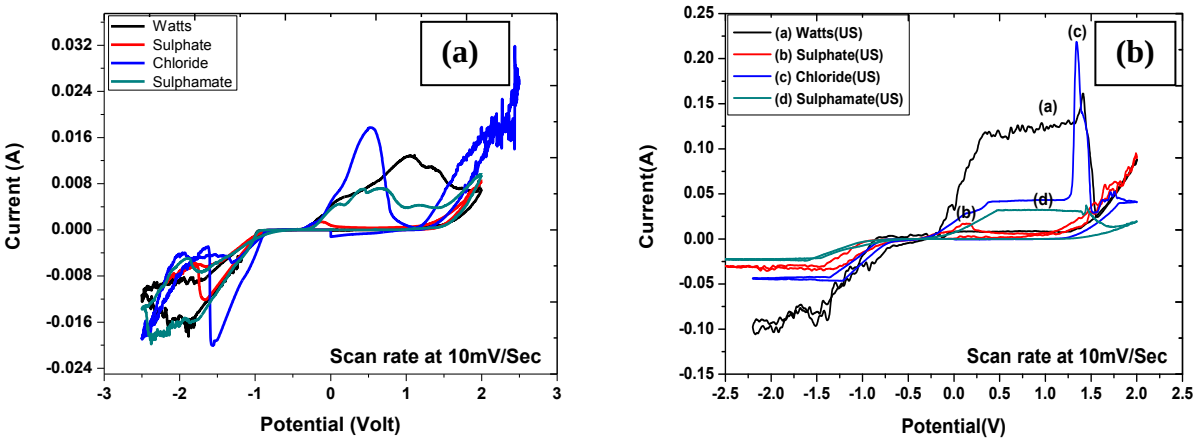

Figure 4.1: Cyclic voltammetry of nickel deposition for four different baths for both (a) silent and (b) ultrasound conditions

Both the cathodic and anodic reactions are followed with some steps of reactions as mentioned below:

Both the cathodic and anodic reactions are followed with some steps of reactions [116].

(1) During the cathodic electrodeposition of nickel with and without sonication from aqueous acid solution, two possible reactions can precede at the electrode surface:

(i) Deposition of nickel is the main reaction occurring at the electrode surface

$$Ni^{2+} + 2e^{-} \rightarrow Ni \qquad (21)$$

(ii) During electrodeposition process, molecular hydrogen is producing at the cathode

$$2H^{-} + 2e^{-} \rightarrow H_2 \qquad (22)$$

In deposition mechanism, a set of reaction is assumed to be most relevant for nickel deposition. Here the nickel monohydroxide cations, $NiOH^{+}$ plays an important species in the charge transfer.

(a) Monohydroxide is formed in the solution as a product of the reaction given below

$$Ni_2^{+} + H_2O \leftrightarrow NiOH_{(aq)}^{+} + H^{+} \qquad (23)$$

(b) Then in the next reaction $NiOH^{+}$ is adsorbed at the electrode

$$NiOH_{(aq)}^{+} \leftrightarrow NiOH_{(ads)}^{+} \qquad (24)$$

(c) The adsorbed $NiOH^{+}$ is discharged by gaining electron

$$NiOH_{(ads)}^{+} + e^{-} \rightarrow NiOH \qquad (25)$$

(d) The last reaction is deposition of Ni at the electrode

$$NiOH + H^+ + e^- \rightarrow Ni + H_2O \quad (26)$$

Similarly during the electrodeposition of Ni, hydrogen discharge takes place which is also followed with several steps of reaction.

(a) Desolvation of hydrogen cations (H_3O^+) and then partially discharge at the electrode surface

$$H_3O^+ + e^- \rightarrow H_{(ads)} + H_2O \quad (27)$$

Also fresh nickel layer act as catalyst which react with hydronium cations to discharge hydrogen

$$Ni + 2H_3O^+ + e^- \rightarrow Ni - H_2 + 2H_2O \quad (28)$$

(b) Next the hydrogen atoms obtained in step (a) combines in the adsorbed state to form adsorbed hydrogen molecules

$$2H_{(ads)} \rightarrow H_{2(ads)} \quad (29)$$

$$2H_3O^+ + Ni - H_2 + 2e^- \rightarrow Ni + 2H_{2(ads)} + 2H_2O \quad (30)$$

(c) Then the last step is the desorption of adsorbed hydrogen molecules as bubbles in hydrogen discharge mechanism

$$nH_2 \rightarrow (H_2)_2 \quad (31)$$

Also during the process of hydrogen discharge chlorine anions are produce which is take place with the following steps

$$Ni^{2+} + Cl^- \leftrightarrow NiCl^+ \quad (32)$$

$$NiCl^+ \leftrightarrow NiCl^+_{(ads)} \quad (33)$$

$$NiCl^+_{(ads)} + e^- \rightarrow NiCl_{(ads)} \quad (34)$$

$$NiCl_{(ads)} + e^- \leftrightarrow Ni + Cl^- \quad (35)$$

(2) The possible reaction steps of nickel layer dissolution with formation and adsorption of nickel species[21]

$$Ni + OH^- \rightarrow NiOH_{(ads)} + e^- \quad (36)$$

$$NiOH_{(ads)} \leftrightarrow NiOH^+_{(ads)} + e^- \quad (37)$$

$$NiOH^+_{(ads)} \leftrightarrow Ni^{2+}_{(sol)} + OH^- \quad (38)$$

Table−4.1shows the other kinetic parameter derived from cyclic voltammetry analysis for both silent and ultrasound conditions. For silent condition referring figure 4.1(a), the cathodic

peaks are observed with increasing negative potentials from chloride, sulphate, sulphamate to Watts bath. For Watts the cathodic peak is observed at highest negative potential as compared to others. It was also observed that the cathodic peak for Watts is quite noisy which may be due to evolution of hydrogen. Again for sulphate and chloride bath, an increase of negative current was observed after the formation of the peaks in the cathodic region. This may be due to the simultaneous evolution of hydrogen gas during the negative sweep of the potential. Cathodic peak for sulphate and chloride are at −1.665V and −1.565V and the corresponding currents are − 0.0121A and − 0.002A respectively. It was also observed that for sulphamate bath there is no such prominent peak rather the cathodic peak goes on increasing from −1.787V to −2.189V. This may be due to excess Ni^{2+} ions or no depletion of discharging Ni^{2+} ions at the graphite/sulphamate interphase. Now focusing on the anodic portion, a huge variation can be observed for different baths. For sulphate, the anodic peak is observed at more negative potential as compared to other electrolyte baths. The intensity of the anodic peak of sulphate bath is also quite less. The corresponding peak may not be the anodic dissolution peak as the physical observation of deposited electrode signifies unlike other reported article [117, 118].

Table 4.1: Experimental values for cyclic voltammetry of electrodeposited and sonoelectrodeposited Ni for four electrolyte baths

Bath types	Ni concentration (gm/l)		Cathodic peak (volt)		Anodic peaks (volt)		Stripping efficiency (Q_a/Q_c)		Crossover potential (volt)	
	SL*	**US****	**SL***	**US****	**SL***	**US****	**SL***	**US****	**SL***	**US****
Sulphate	53.62	53.62	−1.665	−1.484	−0.120	0.115	0.394	0.935	−0.982	−0.468
Chloride	59.32	59.32	−1.565	−1.228	0.536	0.432, 1.333	1.412	1.126	−0.898	−0.645
Watts	64.74	64.74	−1.882	−0.903, −1.394	1.111, 1.340	0.381, 1.423	0.704	1.284	−1.020	−0.238
Sulphamate	67.77	67.77	No distinct peak	−1.458, −1.078	0.122, 0.388, 0.686	0.486, 1.440	0.474	0.935	−1.020	−0.556

Silent condition, **Ultrasound condition

For chloride the stripping peak decreases and then there is a sudden increase of a peak which may indicate that other cathodic processes are active. In addition multiple anodic peaks are observed for Watts and sulphamate on inverting the potential scan direction. Multiple peaks may be due to dissolution or oxidation of pure nickel, nickel hydroxides or nickel hydride

which arises during the deposition process. To analyze the stripping efficiency of deposited nickel, charges due to the cathodic (Q_c) and anodic (Q_a) processes can be obtained from the integration of the cathodic and anodic branches of the I/E curves respectively. The stripping efficiency for sulphate is low and chloride is high which may complement the cyclic voltammetry analysis results. In each case we notice that during the reverse potential scan a crossover on the cathodic branches is observed. The crossover feature indicates that nickel deposition proceeds through a nucleation and growth phenomena. It also relates to the equilibrium potential. The equilibrium redox potential of nickel is -0.225V and the observed cathodic over potential is indicating large negative potential values. Hence the kinetics of the systems of study may be under the control of concentration polarization i.e. a diffusion control one. The kinetic parameters for the ultrasound are also shown in Table 4.1. For ultrasonic condition, referring Figure 4.1, the anodic peak heights are observed as higher compared to that under static condition. These peaks have higher intensities followed with a plateau region. This indicates the increased amount of nickel deposition under the effect of ultrasonic irradiation. But the cathodic reduction peaks are not so prominent and the deposition occurs with the simultaneous evolution of hydrogen gases. There exists crossover potential. This indicates that it is mass controlled instead charge controlled and diffusion is enhanced under the effect of ultrasonic irradiation. The corresponding voltage for reduction and oxidation peaks for all the baths is given in the Table 4.1. The stripping efficiency for sulphate and sulphamate is same which is less than one but chloride and Watts it is greater than one. For Watts and chloride the stripping efficiency is high which may complement the cyclic voltammetry analysis results. Also the cathodic over potential is indicating large negative potential values compared to the nickel equilibrium redox potential. Hence here also the kinetics of the systems of study may be under the control of concentration polarization i.e. a diffusion control one. With the effect of ultrasonic agitation the cathodic over potential reduces and stripping efficiency increases compared to silent condition.

5.2.2. **Chronoamperometry**

The chronoamperometry curves for nickel deposition on the graphite electrode prepared under silent and ultrasound conditions at temperatures 25°C for four different electrolyte baths are illustrated in Fig 4.2(a) & (b). Chronoamperometry was used to study the nucleation and growth mechanism of Ni thin films on the graphite cathode. In chronoamperometry experiments, the deposition is done at a single chosen potential for a specific time period at

which the deposition would occur. The current transients were performed at −1.5V for 30 seconds for static and sonication conditions. The principal nature of a current-time transient for nucleation with overlapping has an initial falling current corresponding to double layer charging, then a rising section corresponding to nuclei appearance and saturation on the substrate and again a falling section due to subsequent growth of electroactive area as established nuclei grow. The characteristic feature of the silent deposition curve is that in which the initial decrease in current corresponds to the double layer charging (DLC) at the electrode surface which prominent for all baths and decreases from sulphamate, Watts, sulphate to chloride. Then there is a rising current which is due to the appearance of the new phase and the increasing number of nuclei present on the electrode surface. Normally at 25˚C the rising current trend is absent for most of the metal films depositions which may be due to the sufficient availability of ions at the start of the experiment after which growth of the nuclei occurs which corresponds to the decaying current whereas at other temperatures the rising and decaying current trend is followed which we observed in Figure 4.2 for both silent and ultrasound. Here in CA curve for all silent baths the nucleation saturation limit for sulphate, chloride, Watts to sulphamate is −0.0115, −0.0219, −0.0196, −0.0155. During the growth section, the current value falls uniformly due to slow rate of diffusion of atoms to the growth interface and then attain a constant growth as in curve predicts in the Figures 4.2[126**]** obeying the Cottrell law. Here the growth period is high for deposits from chloride and sulphate baths. Now for the Sonicated chronoamperometry current transients (SCCT) as shown in Figure 4.2(b), it is observed that for Chloride and sulphamate bath a sharp initial increase in current followed by sequential irregular nucleation and growth loops like current responses but it is not seen for other baths. This random current progression may not be inferred as noise rather it corresponds to the secondary nucleation followed with an irregular growth. The succeeding nucleation loops are the consequences of secondary nucleation due to crystal fragmentation by the formation and collapse of the cavitational bubbles at the electrode surface [127]. The prilimary loops may be due to the conventional 3D nucleation and growth. Hence here the current increases abruptly with a sudden decrease after undergoing a higher and sharper current peak at the maximum compared to that of a silent chronoamperometry current transients. This shows that there is a nucleation process after a certain period of time and hence the nucleation increases with a pre-deposition of ions on to the films. Hence dense and uniform Ni deposits to the graphite substrate. The current transients curves of four baths are fitted to an Scharifker and Hills model to determine of standard kinetics parameters like I_{max} (saturation point of nucleation), t_{max} (time for nucleation

saturation); D(diffusion coefficient) and N (active nucleation density) as shown in Table 4.2. Here the calculated diffusion coefficient, '*D*' and nucleation number density, '*N*' for the Ni depositions in both the conditions is given according to the equations $D = \frac{I_m^2 t_m}{0.1629(zFc)^2}$ and $N = \frac{1.2564}{t_m \pi k D}$, where z is the number of electron involved (here the number of electron involved are 2), F is Faraday's constant, 96500 coulomb, c is bulk concentration of the electrolyte (0.055 gm/cc) and k is a constant,$k = (\frac{8\pi CM}{\rho})^{1/2}$. Where ρ is the density of Copper (8.9 gm/cc), M is the molecular weight of nickel (58.69 gm). The total charge consumed for ultrasound bath condition is more as compared to the charges involved in the deposition without sonication. The difference may be attributed to the nucleation phenomena. The diffusion coefficient calculated for the silent condition is 7.774, 6.069, 8.990, 7.562 ($\times 10^{-12}$ cm^2 s^{-1}) while in the presence of ultrasound the value increases as 113.90, 60.03, 35.73($\times 10^{-12}$ cm^2 s^{-1}) for sulphate, chloride, Watts and sulphamate. This increased value in presence of ultrasound is due to fast mass transport. In the presence of ultrasound the nuclei number density for primary nucleation decreases as compared to silent atmosphere which may be due to the ablation of the electrode surface by the ultrasound, so the number of nuclei near the electrode surface decreases.

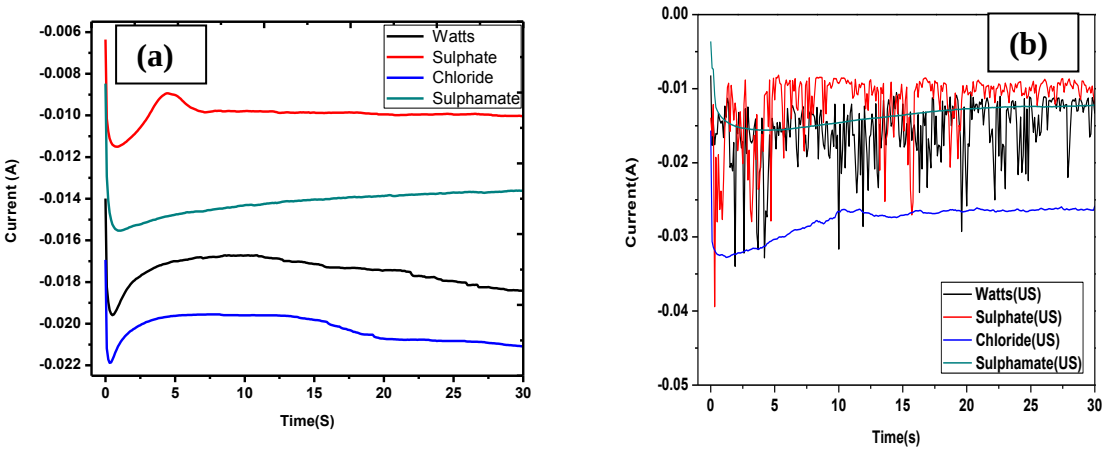

Figure 4.2: Current transients of Ni thin films onto a graphite substrate at -1.5V for four different electrolytes in (a) silent and (b) ultrasound bath.

Table-4.2: Calculated Kinetic Parameter of Ni deposits from chronoamperometry curve in both silent and ultrasound conditions

Bath types	I_{max} (10^{-2} A/cm)		T_{max} (Sec)		D × 10^{-12} (cm^2 s^{-1})		N×10^{10} (cm^{-2})		Q (C)	
	SL*	**US****	**SL***	**US****	**SL***	**US****	**SL***	**US****	**SL***	**US****
Sulphate	−1.15	−7.79	0.8	3.2	7.774	113.90	1.707	0.004	−0.524	0.416
Chloride	−2.19	−3.27	0.4	1.2	6.069	60.03	2.764	0.176	−0.298	0.832
Watts	−1.96	-	0.5	-	8.990	-	3.548	-	−0.608	0.626
Sulphamate	−1.55	−1.56	0.9	4.0	7.562	35.73	3.230	0.084	−0.426	0.458

Silent condition, **Ultrasound condition

5.3. 2D and 3D nucleation and growth model for nickel thin films

Generally two extreme cases of nucleation are considered for the phase formation onto a substrate. Those are instantaneous and progressive nucleation. The main difference between both is that in instantaneous nucleation all nuclei form at the same time and growth take place comparatively slowly but in progressive nucleation new nuclei form during the course of deposition process and growth take place relatively faster. Consequently the nucleation mechanism have been attempted to describe through theoretical models developed by Bewick et al. [128] and Scharifker and Hills [129] for the analysis of 2D and 3D nucleation mechanism and kinetics respectively. The equations are usually used in the form of dimensionless. The curves is plotted against (I/I_m) or $(I/I_m)^2$ and (t/t_m), where I_m and t_m being the current maximum of the measured potentiostatic transient, and the corresponding time, respectively. The theoretical model for 2D instantaneous and progressive nucleation is plotted with the help of the given equation (39) and (40) respectively [128].

$$\frac{I}{I_m} = \frac{t}{t_m} \exp\left[\frac{1}{2}\left\{1 - \left(\frac{t}{t_m}\right)\right\}^2\right] \qquad (39)$$

$$\frac{I}{I_m} = \left(\frac{t}{t_m}\right)^2 \exp\left[\frac{2}{3}\left\{1 - \left(\frac{t}{t_m}\right)^3\right\}\right] \qquad (40)$$

Again equation (41) and (42) are used to plot the theoretical model for 3D instantaneous and progressive nucleation respectively [129].

$$\frac{I^2}{I_m^2} = \frac{1.9542}{\frac{t}{t_m}}\left\{1 - \exp\left[-1.2564\left(\frac{t}{t_m}\right)\right]\right\}^2 \qquad (41)$$

$$\frac{I^2}{I_m^2} = \frac{1.2254}{\frac{t}{t_m}}\left\{1 - \exp\left[-2.3367\left(\frac{t^2}{t_m^2}\right)^2\right]\right\} \qquad (42)$$

To study the nucleation mechanism of nickel thin films, theoretical curves were compared with experimental data which were plotted against (I/I_m) or $(I/I_m)^2$ and (t/t_m), to examine the

nucleation mode (2D/3D) and trend (instantaneous/progressive) of appearance of nuclei for all electrolytic baths with constant deposition potentials. Plots of (I/I_m) vs. (t/t_m) for 2D nucleation mechanism is calculated from Eq^{n}s. (39) and (40) and $(I/I_m)^2$ vs. (t/t_m) for 3D nucleation mechanism is calculated from Eq^{n}s. (41) and (42) for both silent and ultrasound deposition at potential −1.5V are shown in Figure 4.3 (a) & (b) along with the experimental data taken from the current–time transients presented in Figure 4.2(a) & (b).

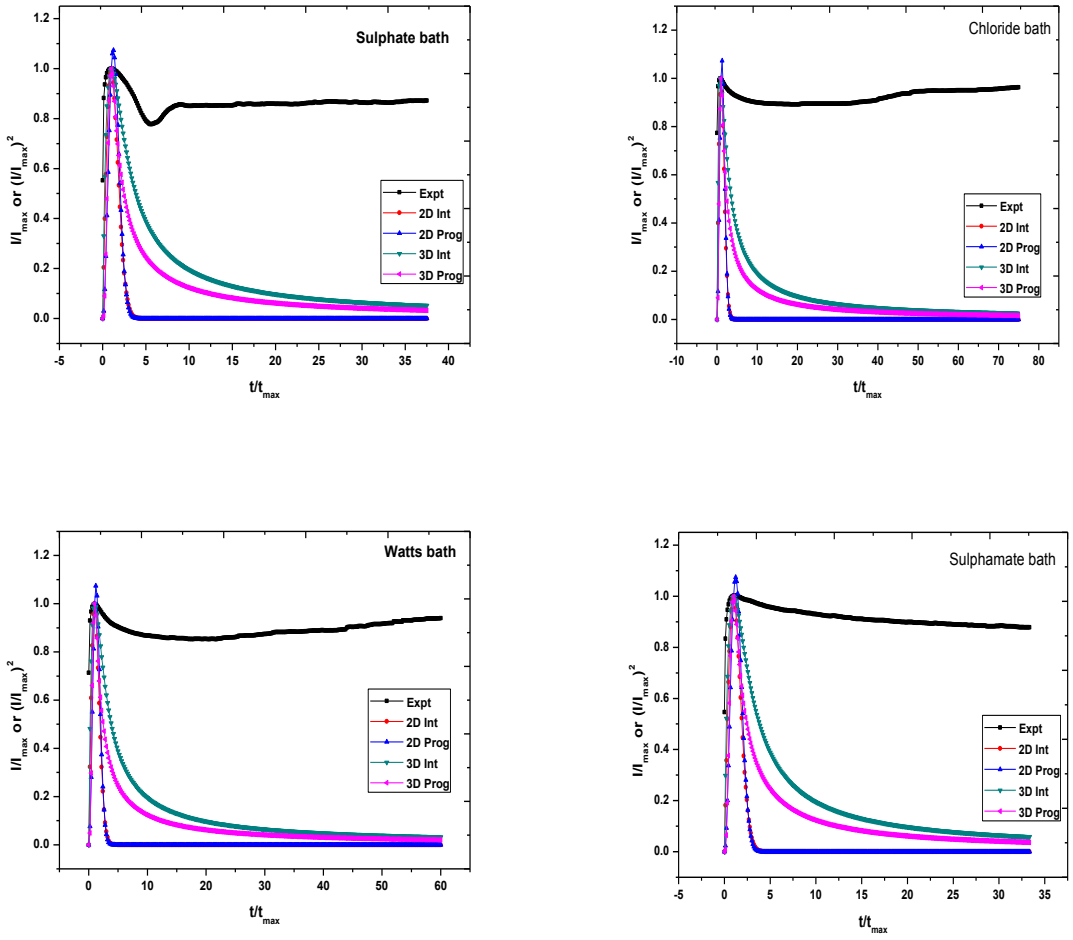

Figure 4.3(a): A comparison of the theoretical 2D and 3D plot for both instantaneous and progressive nucleation with experimental data for silent deposition at potentials of −1.5V for all baths

From the figure it is observed that the rising part of the experimental curves coincides with the theoretical curves for 2D as well as 3D instantaneous nucleation, indicating appearance of fresh nuclei on the active sites, which are activated at the same time. After the maximum, the expected behavior of 2D theoretical currents to vanish after formation of a monolayer can be observed, since the exponential terms decrease faster than their coefficients increase with time. Whereas a positive deviation of experimental curve, which is the result of the current

transients terminated to a plateau can be found. This phenomenon can be due to the further formation of new layers on the underlying monolayer preventing a drop in current.

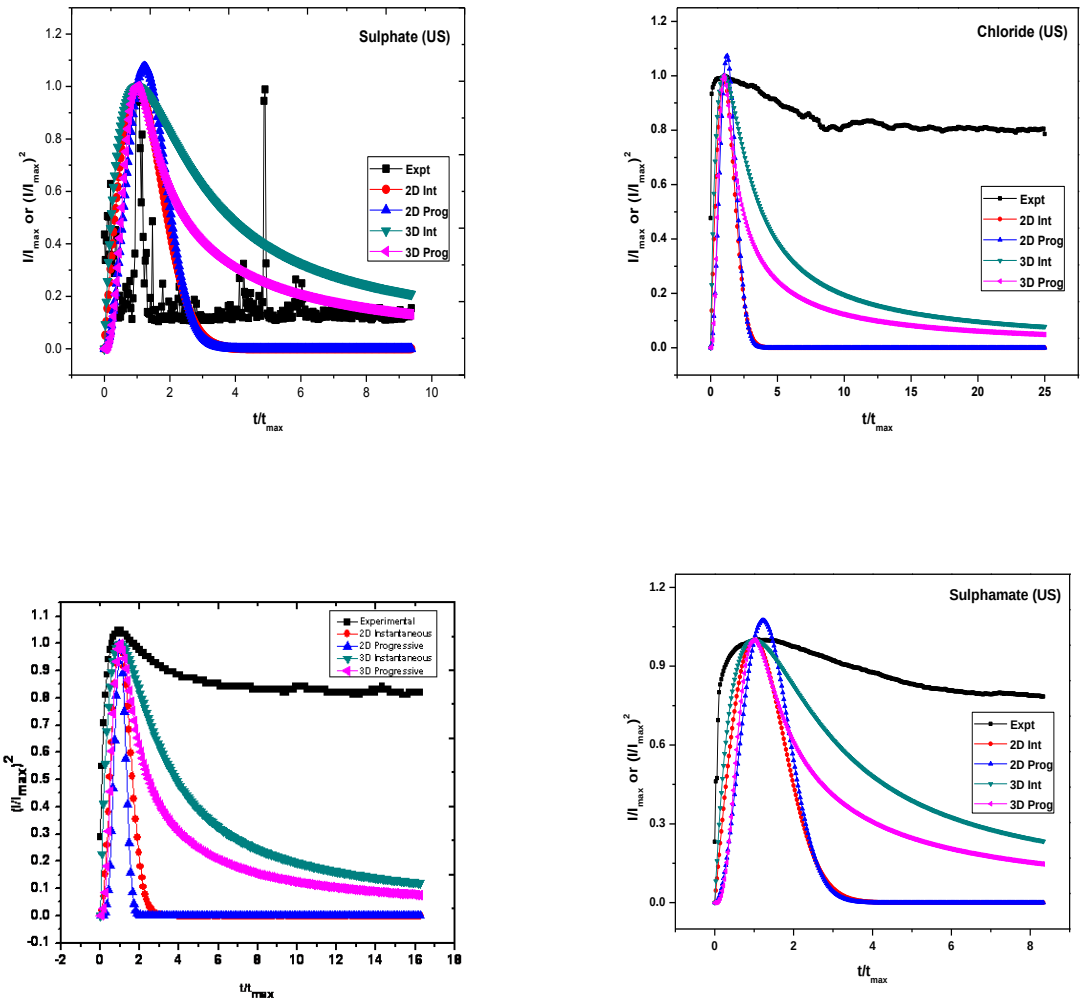

Figure 4.3(b): A comparison of the theoretical 2D and 3D plot for both instantaneous and progressive nucleation with experimental data for ultrasound deposition at potentials of −1.5V for all baths

Hence the 2D module of appearance of Ni nuclei can be ruled out here. Furthermore the figure shows that, for longer time ($t \geq t_m$), the experimental data are in good agreement with the grow law for instantaneous nucleation followed by diffusion limited growth with obvious positive deviation from the theoretical plot. This deviation can be reasonably attributed to the presence of a parallel reaction to the Ni film electrodeposition process.

5.4. Structural characterization

A structural analysis study was carried out with the help of XRD pattern, SEM and AFM micrographs. The XRD analysis gives detail of grain size, lattice strain and SEM and AFM shows the morphology of the surface of the deposited Ni thin films with and without sonication for four different electrolyte baths includes sulphate, chloride, Watts and sulphamate. The section below gives the detail survey of these techniques for all baths.

5.4.1. **Phase analysis by XRD**

Figure 4.4 (a) & (b) shows the X−ray diffraction pattern of Nickel deposits for silent and ultrasonic condition for different electrolyte baths deposited on a graphite substrate in the range of scanning angle 40°−100° at a scanning rate 2° with CuKα radiation (λ=1.5406A°) using X Ray Diffractometer. The average crystallite sizes of the deposits were determined by the Williamson-Hall formula as Scherrer equation is valid only for powders or loosely bound deposits but not for hard and adherent deposits. The lattice strain for deposits from four types of bath is calculated from the XRD graph. The contribution of the particle size and nonuniform strain in the grains to the observed X-ray line broadening, β, are considered to be additive generating the formula as:

$$\boldsymbol{\beta_{total}} = \boldsymbol{\beta_{particle}} + \boldsymbol{\beta_{strain}} = \frac{(0.94)\lambda}{t\cos\theta} + 4\tan\theta\frac{\Delta d}{d} \qquad (43)$$

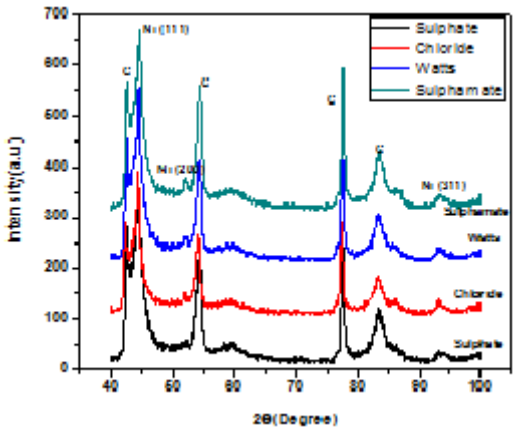

Figure 4.4(a): XRD pattern for silent condition for Ni deposits obtained from four different baths

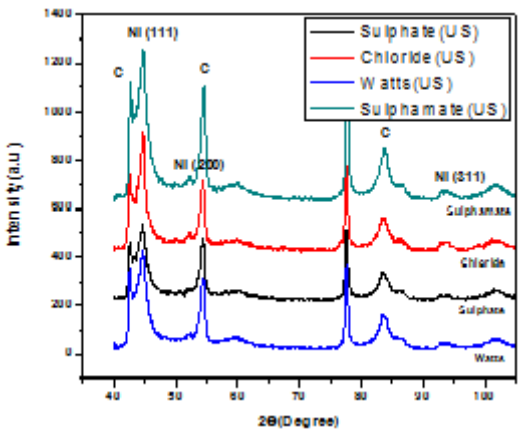

Figure 4.4(b): XRD pattern for ultrasonic condition for Ni deposits obtained from four different baths

Figure 4.4(a) & (b) shows that all baths have the same XRD peaks, and the peak intensities vary for different baths. From the XRD graph the diffraction peaks are obtained at 2θ = 44.64 and 93.09 for sulphate which can be indexed as (111) and (311) planes respectively. Again the diffraction peaks are obtained at 2θ = 44.44, 51.82 and 93.07 for chloride, 44.56, 51.92 and 93.18 for Watts, 44.67, 52.00, and 93.16 for sulphamate which can be indexed as the

(111), (200) and (311) crystallographic planes of Nickel with FCC crystal structure for all baths both for with and without sonication respectively. There are also some carbon peaks obtained which may be due to very thin deposits of nickel. From the graph, the intensity of the nickel peaks reduce for ultrasonication, this shows finer grain size for sonication condition. It is observed that the crystallite size decreases from chloride, sulphate, Watts to sulphamate and strain decreases from sulphamate, Watts, sulphate to chloride. Now strain is defined as a force which has a tendency to pull or stretch the grains. So finer the grains, number of grains per unit volume will be more, hence the grain boundary region increases with the increase in pulling effect between the grains. Thus it is observed that strain is more for finer grains. The measured crystallite size and lattice strain in the as deposited Nickel films for both silent and ultrasonic condition as a function of bath type calculated by XRD graphs are shown in Table-4.3.

Table−4.3: Calculated Crystallite size and Strain of Ni thin film deposits for silent and ultrasonic

Bath types	Potential (Volt)	Silent		Ultrasonic	
		Crystallite size (nm)	Strain %	Crystallite size (nm)	Strain %
Sulphate	−1.5V	91	0.233	44	0.797
Chloride	−1.5V	98	0.380	43	0.720
Watts	−1.5V	83	0.131	38	0.210
Sulphamate	−1.5V	69	0.099	21	0.405

5.4.2. **Morphology analysis**

A structural analysis study was carried out with the help of SEM and AFM micrographs.

5.4.2.1. SEM analysis

Film morphology and composition is obtained by scanning electron microscope (SEM) at low acceleration voltages. The SEM analysis of Ni electrocrystallization for with and without sonication for most practiced electrolyte baths is shown in Figure 4.5 below. It shows the SEM microstructure of Ni for four different bath i.e. sulphate, chloride, watts and sulphamate bath for both with and without sonication. Nickel deposition from chloride bath gives well connected spherical morphology. Here the grains appear to be nodular like shape for Watts, sulphate and sulphamate but for chloride the grains appear to be rice like precipitation with a globular structure. It is observed that the grain size for sulphamate is quite low as compared to the other baths. The extent or degree of agglomeration is high for sulphamate and Watts.

Due to the agglomeration, grains appear to have 3D model of growth for sulphamate and Watts. Some regions are nearly granular as seen in Watts and sulphate and some are highly coalesced fine grains along with some agglomeration of particles which are observed in chloride and sulphamate. These SEM data indicate that deposition at different Ni concentration in different baths leads to the formation of many small nodular nuclei and a relatively uniform coverage of the graphite substrate.

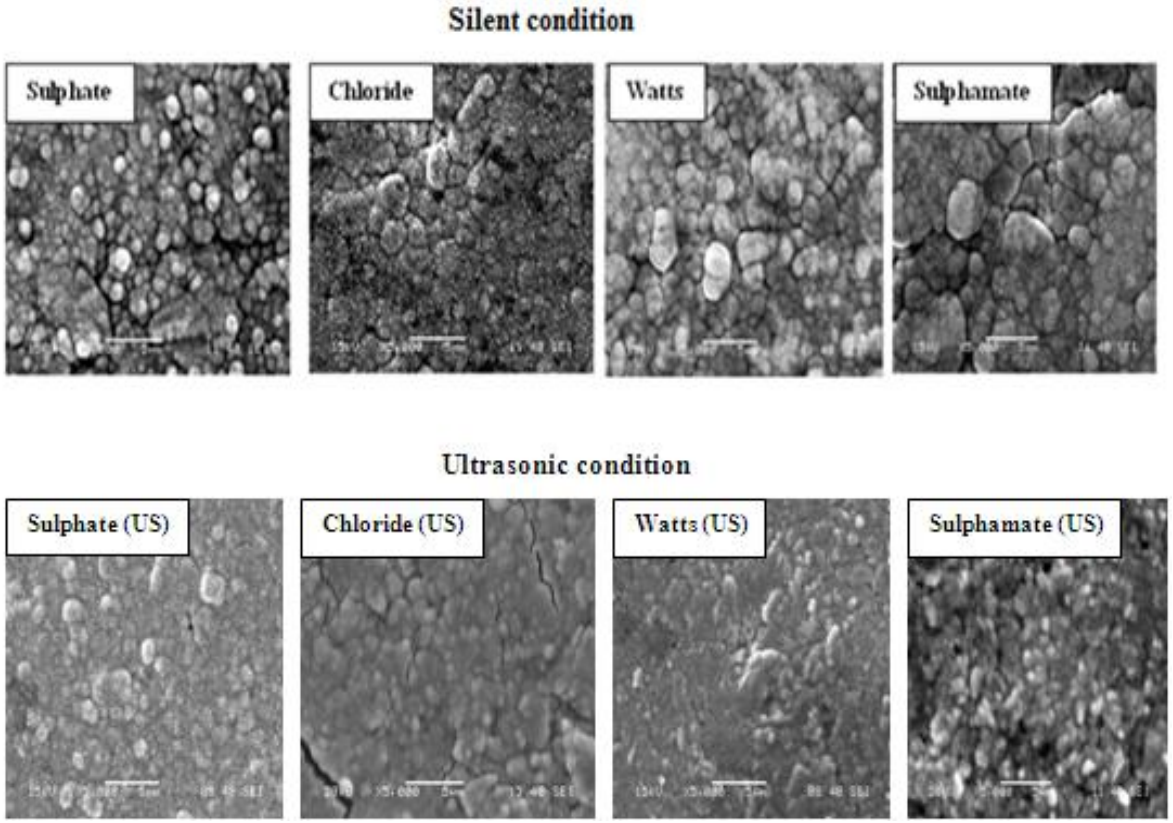

Figure 4.5: SEM morphology of Ni deposition on a graphite substrate for four types of bath for -1.5V and 25^0C, with and without sonication.

From the Figures 4.5 it can further be analyzed that, ultrasonic irradiation has a definite impact on the topological morphology variation. For Ultrasonic agitation the surface coverage is more and also grain size is reduced, which is also calculated from XRD pattern. It can be observed that, the deposit has got improved in terms of surface coverage, uniformity, grain size variation, surface quality from chloride, sulphate, Watts to sulphamate baths. It gives finer, smooth and continues film structures. However the film produced from sulphate and chloride bath shows more surface cracks than other baths, the reasons for which may not be concluded at this point. For both the condition (silent and ultrasound) for the watts and sulphamate bath gives the compact, adhered, higher surface coverage, comparatively uniform grain distribution and thicker deposits. The deposited nickel nuclei bear the spherical shape

with varying grain distribution. The basic characteristic of morphology is a uniform Nickel covered surface with well agglomerated spheroids. A comparative compositional analysis form the EDS is report below in fig. 4.6 (a) and (b) and the detail of the elemental percentage is given below in Table -5(a) and (b). From EDS it is clear that the Ni composition is more for sulphate bath rather than chloride, watts and sulphamate bath.

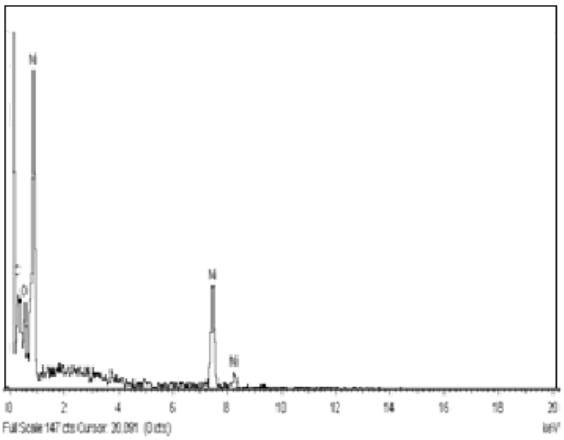

Figure 4.6(a): EDS of Ni deposition in silent condition.

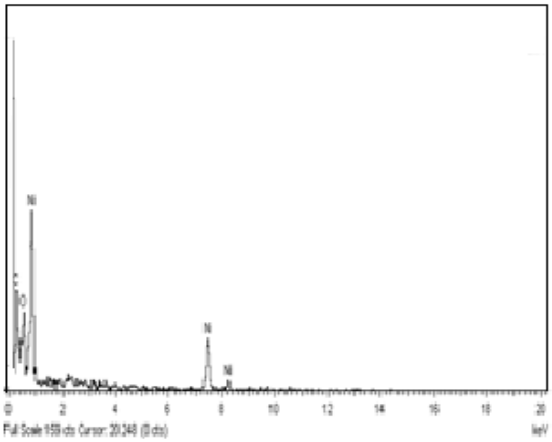

Figure 4.6(b): EDS of Ni deposition in ultrasonic condition.

Table 4.4: Ni composition in the deposited film from EDS analysis

Bath types	Ni wt %	C wt %	O wt %
Sulphate	77.25	5.65	17.1
Chloride	49.39	38.02	12.59
Watts	30.75	44.39	24.86
Sulphamate	32.92	37.01	30.07

5.4.2.2. AFM analysis

However, the SEM studies were not capable of producing the detail of morphological studies. Hence structural characteristics are further ventured with AFM. Figure 5 presents AFM micrograph of nickel deposits prepared in different baths at same conditions for all the baths for silent and ultrasound condition. The roughness factors and the average and maximum elevation along with the average grain size of nickel deposits for all the respective baths for both condition are illustrated in Table−4.5. The roughness values of the treated surfaces for different baths vary from 404 to 203 nm for silent and 121 to 196 nm. The roughness is very high for sulphamate, chloride and sulphate but minimum for Watts in both conditions. This higher extend of roughness may be due to the extent of agglomeration of particles. Here the calculation of grain size is difficult due to the high degree of agglomeration of the grains. Hence it shows the average agglomerated grain size for nickel deposits for the respective

baths are in micrometer range for silent and ultrasound. The average agglomerated grain size decreases from 1.436 to 0.540 for chloride, sulphate, sulphamate to Watts for silent and 0.789 to 0.380 µm for sulphate, Watts, chloride to sulphamate. From the results it may be told that ultrasound reduces the roughness and grain size which can be observed in Figure 4.8(a) & (b).

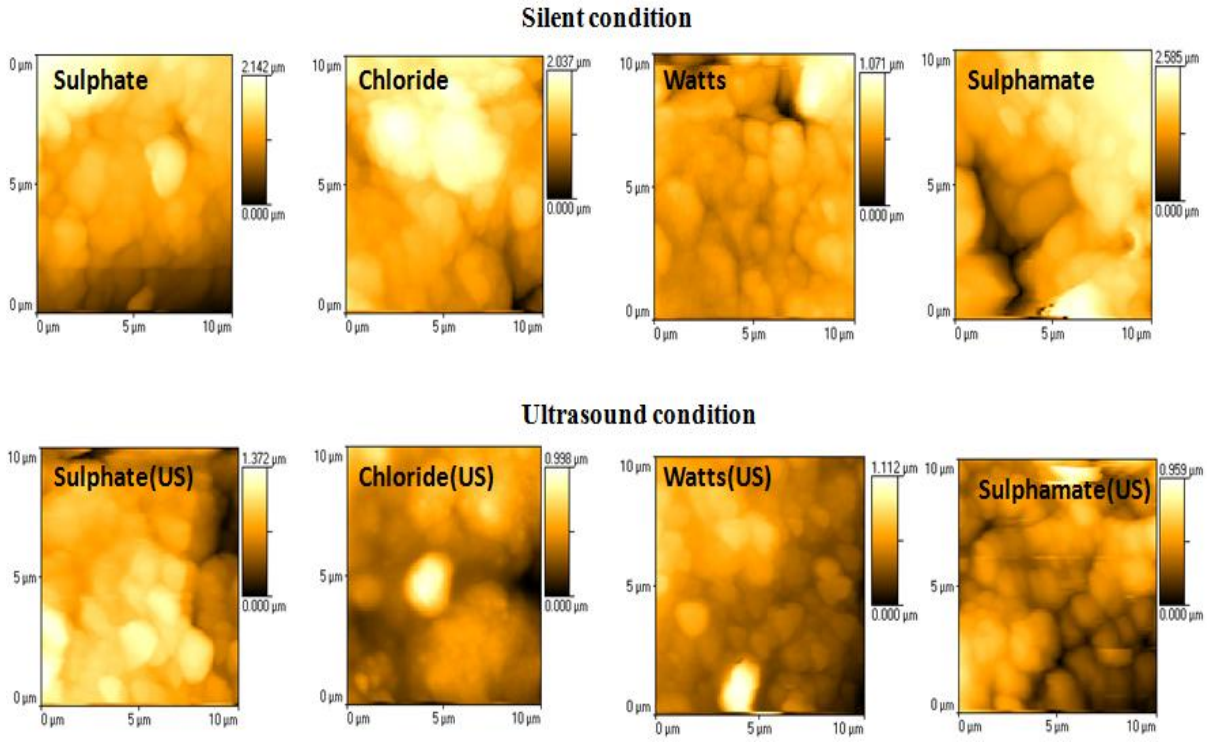

Figure 4.7: AFM morphology of four different baths with scan area of 10µm×10µm for silent and ultrasound

Table 4.5: Roughness factors, average grain size, the maximum and minimum height for all bath types with and without sonication from AFM analysis

Bath types	Roughness (µm)		Avg. Height (µm)		Max. Height (µm)		Avg. agglomerated Grain size (µm)	
	SL*	**US****	**SL***	**US****	**SL***	**UL****	**SL***	**US****
Sulphate	0.337	0.196	1.158	0.774	2.142	1.372	1.306	0.789
Chloride	0.302	0.115	1.292	0.148	2.037	0.998	1.436	0.401
Watts	0.203	0.142	0.559	0.455	1.071	1.112	1.086	0.446
Sulphamate	0.404	0.121	1.578	0.388	2.585	0.959	1.266	0.380

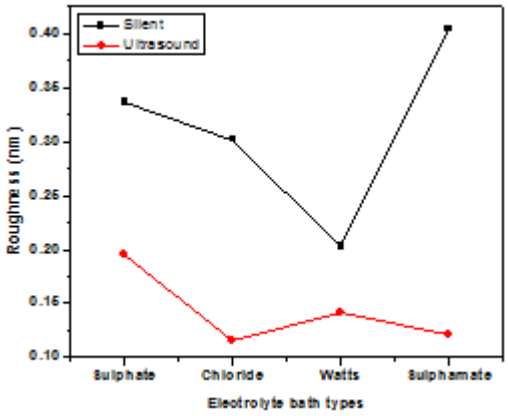

Figure 4.8(a): Variation of roughness in four baths with and without sonication.

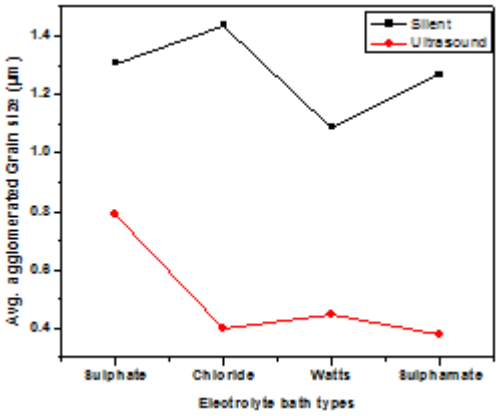

Figure 4.8(b): Variation avg. agglomerated grain size for four baths with and without sonication.

5.5. Property analysis

The structural properties include microhardness, nanohardness, residual stress etc. which were studied and analyzed with the help of microhardness tester machine, nanoindentation tester and stylus surface profilometer instruments.

5.5.1. **Hardness**

The microhardness of the deposited Ni was calculated by Microhardnesss tester. Table−4.6 presents the microhardness of Ni thin films deposited at different electrolytic baths for silent and ultrasound condition. The load applied for hardness testing is 50gf. From the below table it shows that the hardness is high for sulphamate and Watts and low for sulphate and chloride for both conditions. But with the application of ultrasound the microhardness improves which improves the mechanical properties. The microhardness decreases with the increase in grain size hence the hardness increases from chloride, sulphate, Watts to sulphamate baths. The relation between the grain size and microhardness fits by the Hall–Petch law (HPL) relationship expressed as, $\sigma = \sigma_o + K_H . d^n$, approximately, where 'σ' is yield stress, $'\sigma_o'$ is lattice friction to overcome when removing a single dislocation, 'K_H' is constant, 'd' is the average grain diameter, and 'n' is the exponent of grain size (usually −0.5). According to the expression, as the grain size decreases, the hardness of deposits will increase. This is a relational expression between yield stress or hardness and grain size, based on the dislocation pile-up theory of monocrystalline/polycrystalline materials [130− 132]. The hardness enhancement may also attribute to induced compressive residual stress as well as dense and compact microstructure [130−133] as mentioned in the following sections. Figure 4.9(a) &

(b) shows the variation of grain size and microhardness with the different electrolyte bath types and in both the cases it seems to have a better property for ultrasonic agitated baths.

Table−4.6: Microhardness of Ni deposits for four electrolyte baths for silent and ultrasound condition

Bath types	Load applied (gf)		Grain size (nm)		Microhardness (GPa)	
	SL*	US**	SL*	US**	SL*	US**
Sulphate	50	50	91	44	0.814	1.137
Chloride	50	50	98	43	0.482	0.965
Watts	50	50	83	38	1.402	1.751
Sulphamate	50	50	69	21	1.645	1.840

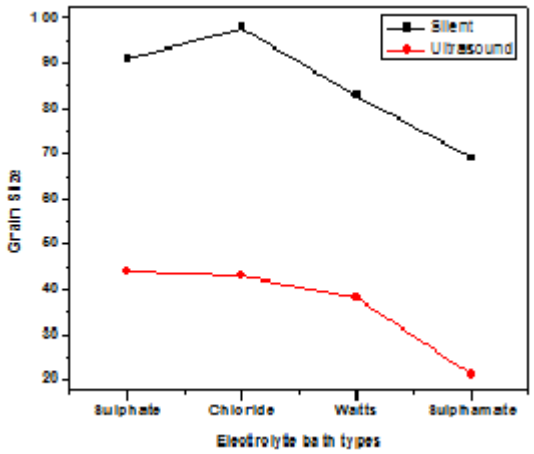

Figure 4.9(a): Variation in grain size for four baths with and without sonication.

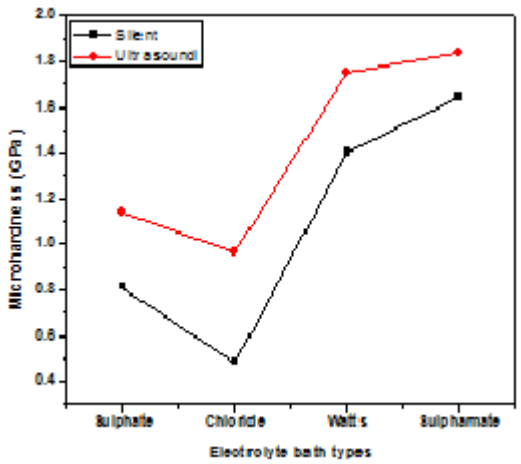

Figure 4.9(b): Variation in microhardness for four baths with and without sonication.

5.6. Residual stress analysis

Residual stress can have strong effects on film properties and mechanical performance. These stresses are basically caused by interface coherency, thermal cycling and change in deposition parameters [47-49]. The understanding the origin of such stresses and controlling them is important for the reliable manufacture of such thin film system. There are three components of the residual stress devolved in thin film at a given temperature. Magnitude of a residual stresses $'\sigma\ '$ can be expressed as

$$\sigma = \sigma_{th} + \sigma_i + \sigma_e$$

Where σ_{th}= Thermal stress is due to the difference in thermal coefficient of substrate and deposited films, σ_i= Intrinsic stress is due to the intrinsic factors like lattice mismatch, presence of impurities etc. and σ_e= Extrinsic stress is due to the external factors.

The residual stress can be measured by wafer curvature method. If the film thickness is far thinner than the substrate, the residual stress of the film is calculated by using the Stoney's equation [51] which is given by,

$$\sigma_f = \frac{1}{6}\left(\frac{1}{R_2} - \frac{1}{R_1}\right)\frac{E_s t_s^2}{(1-\upsilon_s)}\left[1 - \frac{t_f}{t_s}\right]$$

where, Es is that the Young's modulus. υ_s is that the Poisson's ratio of the substrate. R1 and R2 are substrate's radii of curvature before and after film deposition respectively. t_s is the thickness of the substrate and t_f is the thickness of the film. Table−4.7 shows the roughness, residual stress and film thickness for the deposits obtained from four different baths for silent and ultrasound conditions. From the table it is observed that stress reduces with the effect of ultrasonic agitation. For both silent and ultrasonic condition stress is more for sulphate, chloride and minimum for Watts and sulphamate baths. Here the compressive and tensile stress is found to be very low for sulphamate bath as compared to other baths. Also from the table it is observed that the tensile stress is more in case of silent condition and compressive stress is less but with the application of ultrasound to the electrolyte baths, the tensile stress reduces and compressive stress increases for all bath types. Table−4.7 gives the detail experimental values like film roughness, thickness and residual stresses for four different baths in which sulphamate and next to it is Watts which posses the best results for structural applications.

Table−4.7: Showing the experimental values for roughness and residual stress of the deposited Ni film on a graphite substrate with and without sonication from the stylus surface profilometer analysis

Bath types	Roughness (nm)		Residual Stress (GPa)				Film thickness (µm)			
	SL*	US**	Compressive		Tensile		Theoretical		Calculated	
			SL*	US**	SL*	US**	SL*	US**	SL*	US**
Sulphate	485	398	9.234	12.031	15.770	4.886	1.570	1.931	1.356	1.893
Chloride	576	492	11.231	16.195	16.608	1.122	2.670	3.685	2.767	3.787
Watts	409	311	8.684	11.119	4.272	1.009	2.360	2.613	2.380	2.849
Sulphamate	369	307	4.015	22.003	3.778	0.990	1.970	2.357	1.939	2.089

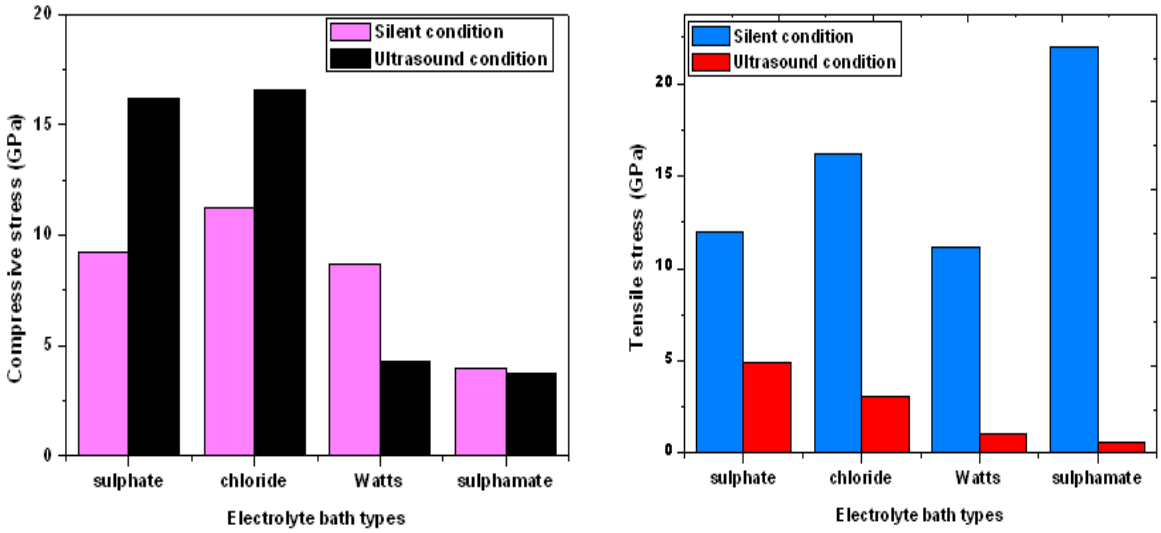

Figure 4.10: Showing the variation in stresses both for (a) silent and (b) ultrasound condition.

The residual stress was found to be compressive irrespective of deposition condition and is found to be increased but tensile stress is found to be reduced in the presence of ultrasound as it is observed from the bar graph chart mentioned in Figure 4.10. The result indicates that ultrasound has a definite impact on the deposit characteristics. The stress analyses were also done with the help of SEM micrographs which is shown in Figure 4.10 (c). Figure 4.10 (c) shows the SEM microstructure for all baths for silent and ultrasound. From the micrographs it is observed that for ultrasound the residual stress reduces to a higher extend.

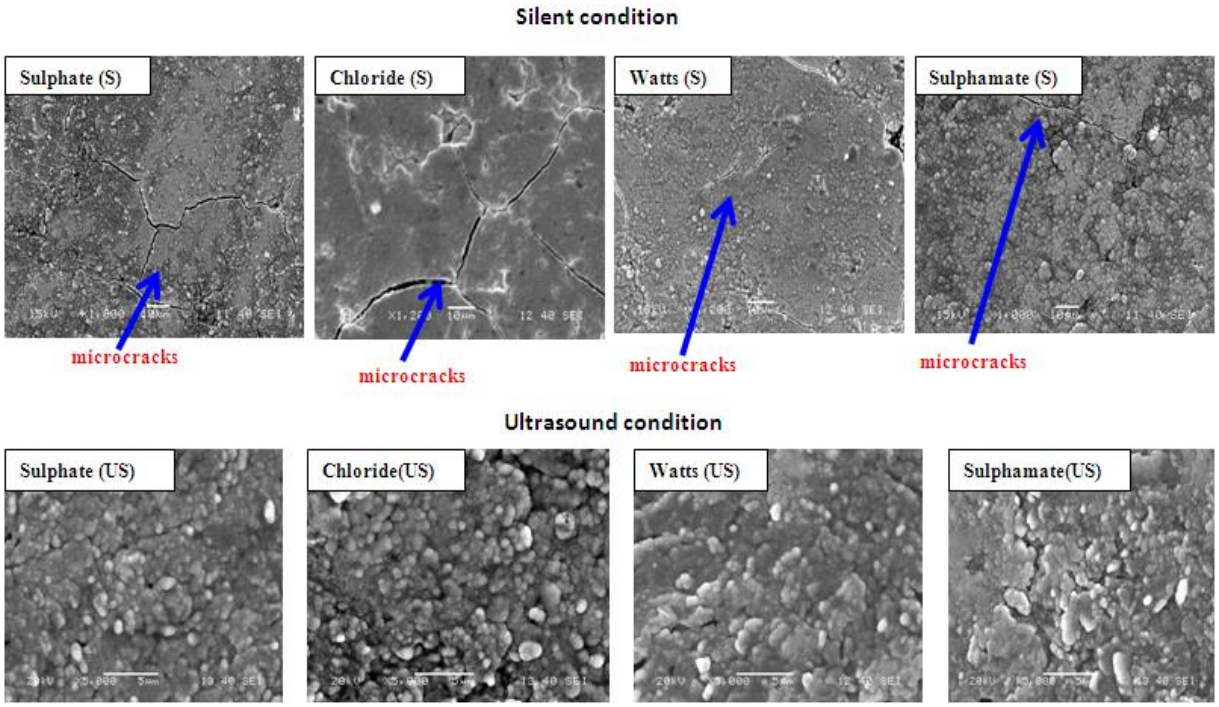

Figure 4.10(c): SEM micrograph showing generation of crack due to residual stresses in Ni deposited thin film and the relief of stress for ultrasound condition foe all electrolyte baths.

Figure 4.11(a) and Figure 4.11(b) are the data plots from the surface profilometer during the analysis of film thickness and, roughness and residual stress. Figure 4.11(b) shows the compressive and tensile stresses for the deposits from sulphamate bath for silent and Figure 4.11(d) shows the compressive and tensile stresses for the deposits from sulphamate bath for ultrasonic condition. Here the compressive and tensile stress is found to be very low as compared to other baths.

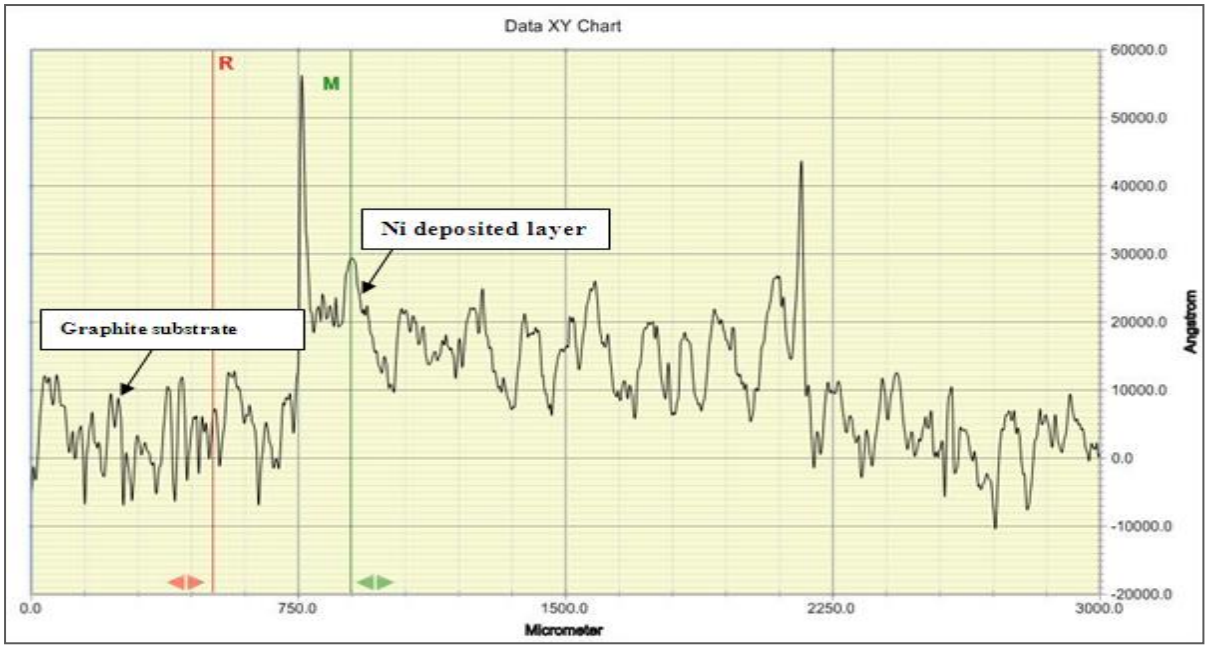

Figure 4.11(a): Showing the film thickness of electrodeposited nickel observed from the Dektak offline software of Stylus surface profilometer.

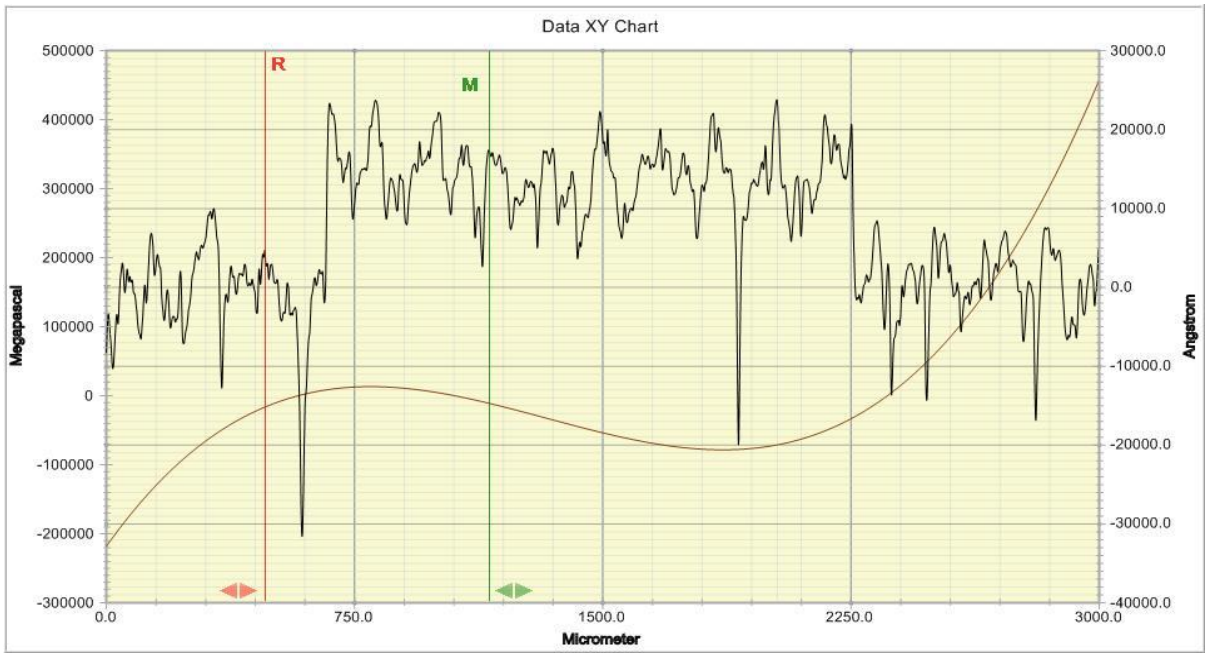

Figure 4.11(b): Showing the tensile as well as compressive stress generated during the film growth observed from Dektak software of Stylus surface profilometer.

Figure 4.11(c) and Figure 4.11(b) also shows the surface profile for sonoelectroplated Ni thin films, showing the film thickness, compressive and tensile stresses generated during the Ni thin films deposition.

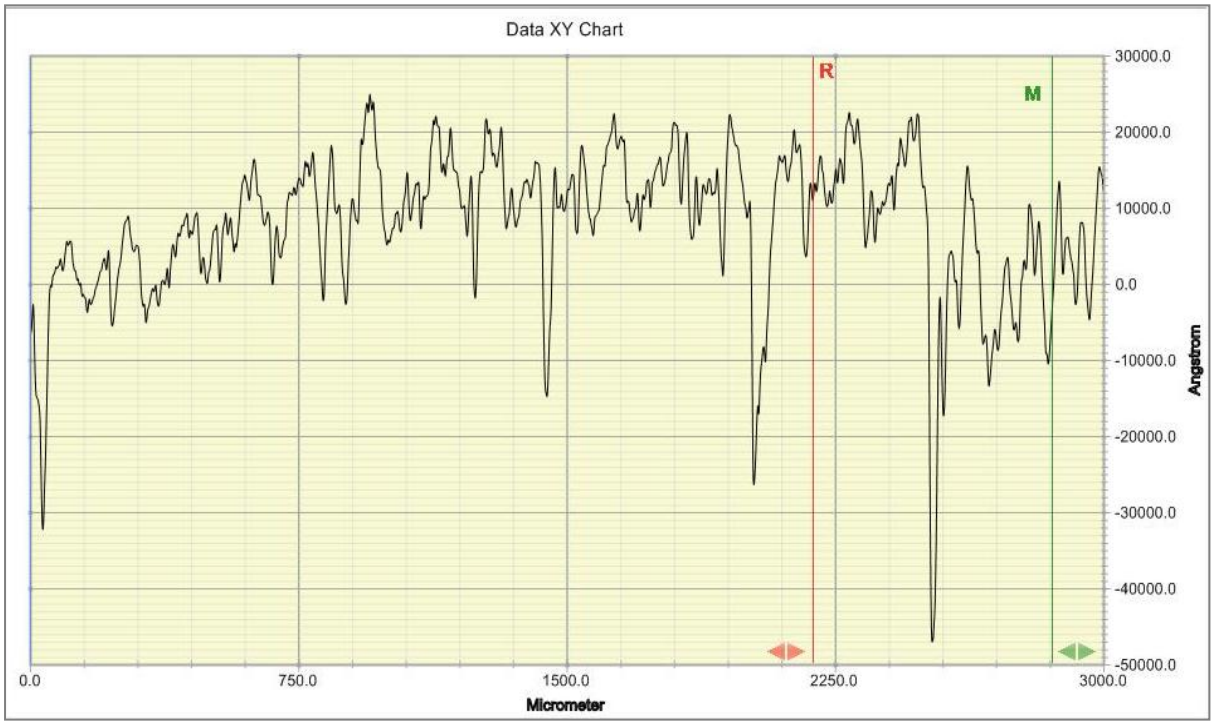

Figure 4.11(c): Showing the film thickness of sonoelectroplated nickel observed from the Dektak offline software of Stylus surface profilometer.

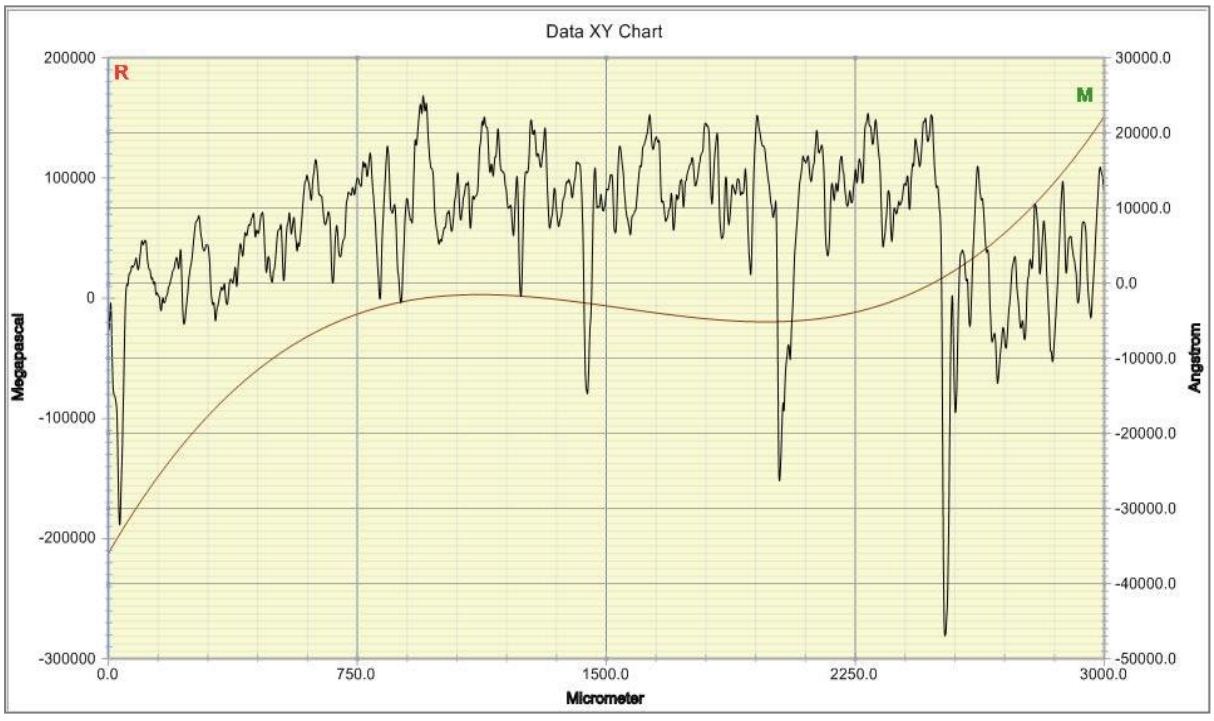

Figure 4.11(d): Showing the tensile as well as compressive stress generated during the film growth for sonoelectroplated Ni observed from Dektak software of Stylus surface profilometer.

5.6.1. **Residual stress dependence on film thickness**

It observed from the Table 4.8 that, residual stress in the nickel films was always compressive regardless of film thickness. In the films 500 nm to 2100 nm in thickness, the residual stress was approximately 7.757 GPa for tensile stress and 33.431 GPa. High tensile stresses leveling at 35.796 GPa were found in 500 nm thick films as well as the for this thickness the compressive stress is found to be 36.560 GPa. This shows that with the increase in thickness the compressive stress increases and tensile stress decreases which is also observed from the graph given in Figure 4.12.

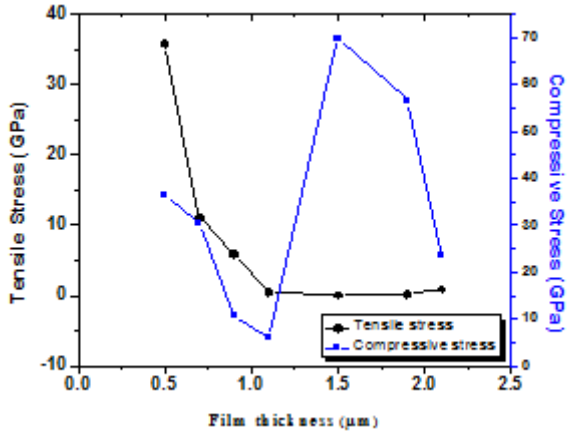

Figure 4.12: Stress versus Thickness for electrodeposited nickel thin films

Table 4.8: Stress values obtained for variations in thickness for Ni thin films

Film thickness	Tensile stress	Compressive stress
0.5	**35.796**	**36.560**
0.7	**11.096**	**30.424**
0.9	**5.863**	**10.845**
1.1	**0.431**	**5.837**
1.5	**0**	**69.851**
1.9	**0.25**	**56.671**
2.1	**0.866**	**23.625**

In the beginning of film deposition, the film does not form uniformly in its thickness but develops in an aggregate composed of small islands. Since the stress in a peripheral region of an island partially declines in its magnitude; an average stress in the islands is smaller than the stress in a film with uniform thickness. The stress reduction rate is largely determined by the ratio of thickness to size of the island. In the very beginning of the deposition, many nuclei of tiny islands are formed on the substrate. Since these nuclei are tiny, the stress is considered to be significantly small. As depositing time increases, these tiny nuclei coalesce

with each other to form islands and finally change into a solid film on the substrate. After this film formation, compressive stresses developed during the cooling stage will force the atoms through the grain boundaries as well as a film surface. These atomic migrations form hillocks at the grain boundaries on a film surface, bringing about stress relaxation in films thicker than 0.8μm. From the AFM micrographs in Figure 4.13 it is observed that as the film thickness goes on increasing the grain growth also increases and this may be the reason for the relaxation of residual stress in thin films.

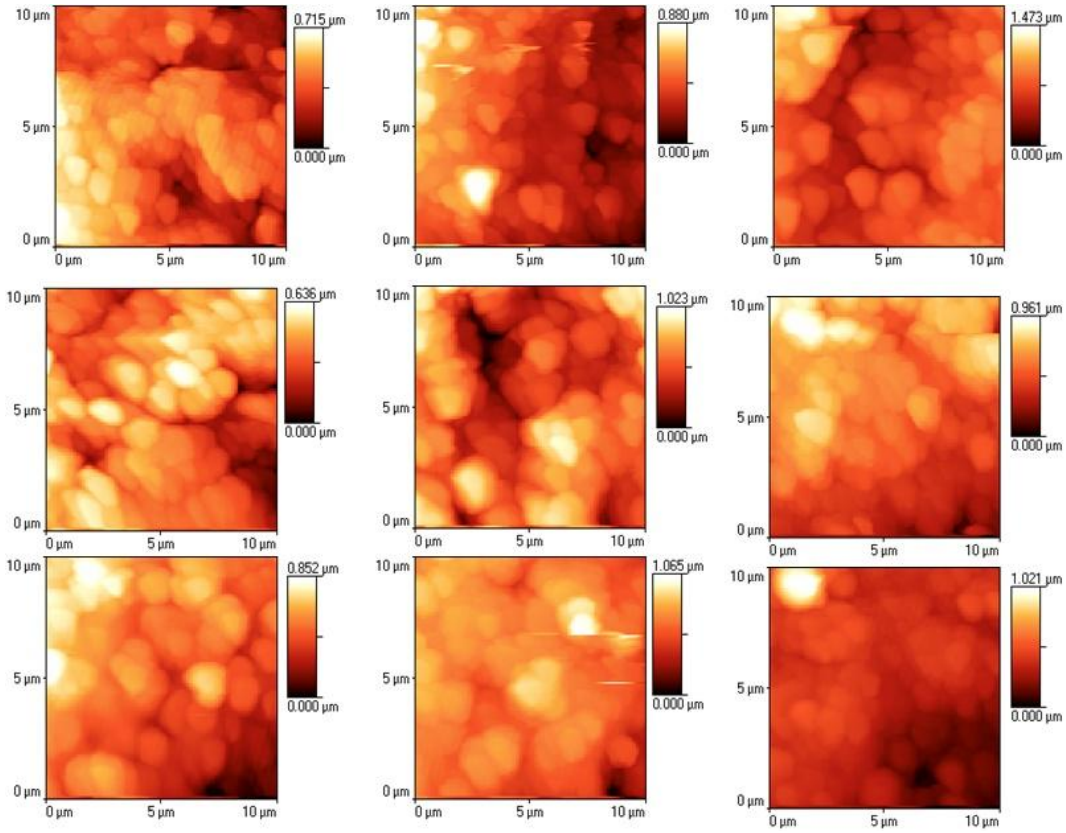

Figure 4.13: Variation in thickness which shows the change in grain structure that effect the stress in films.

CHAPTER -5

Conclusions

Conclusions

5.1. Conclusions

The project report enumerates on in−process analysis (cyclic voltammetric and chronoamperometry) and post synthesis analysis (SEM, AFM, XRD, Stress, Hardness) of nickel electrocrystallization from four different types of baths for different condition i.e. silent and ultrasonic condition. The observations and analysis of the results gained from the above studies are enumerated below which is concluded in points which are reflected below for a better understanding.

i. Cyclic Voltammetry (CV) was performed in the potential range of −2.5 to +02.5V at different bath temperatures to know the chemistry of redox couples both in silent and under ultrasound respectively. The redox couple undergoes two sequential electron transfer reactions which are confirmed from the two peaks in the voltammogram. At sonication reduction peak is not well resolved, indicates enhanced mass transport by the ultrasound but the oxidation peak is well resolved. The intensity of the peaks obtained from the CV scan for ultrasonic condition for all baths is three times greater than for silent conditions.

ii. Chronoamperometry was performed at −1.5V for 30 seconds for all baths. The standard kinetic parameters using Scharifker and Hills model are found. The diffusion coefficients calculated for the silent condition is between 6.069−8.990 x $10^{-12} Cm^2 S^{-1}$ while in the presence of ultrasound the value varies from 35.73-113.90 x$10^{-12} Cm^2 S^{-1}$. The increase in diffusion coefficient in sonication is the consequence of enhanced mass transport by the cavitations phenomena in the presence of ultrasonic field.

iii. From morphological and phase analysis, the grain structure, grain size, crystallite size and lattice strain were studied. From SEM and AFM analysis the surface roughness was reduced to a greater value with a fine grain structure, due to the effect of ultrasonic agitation. From XRD analysis it was observed that the grain size decreases and lattice strain increases form chloride, sulphate, Watts to sulphamate for silent and ultrasonic condition. The crystallite size varies from 69 to 91nm and lattice strain% from 0.099 to 0.380 for silent, similarly for ultrasonic condition the crystallite size varies from 21 to 44 nm along with the lattice strain% from 0.210 to 0.797 for all

baths. Also from AFM analysis it is observed that the grain size varies from 1.086 to 1.436μm for silent and 0.380 to 0.789μm for ultrasound for all bath types.

iv. The deposit from the bath with ultrasound gave a smoother surface from chloride, sulphate, Watts to sulphamate bath. Hardness value was found to be increased from 0.482, 0.814, 1.402, and 1.645GPa to 0.965, 1.137, 1.751 and 1.840GPa respectively for chloride, sulphate, Watts to sulphamate bath for silent and ultrasound conditions. The film thickness varies from 1.3 to 2.7 μm for silent and 1.8 to 3.7 for ultrasound in the four types of baths. The thickness of all the films is below 2.670μm for silent and 3.740μm for ultrasonic condition. The residual stresses of the deposits were reduced with an ultrasonically agitated bath. For silent condition the compressive stress for different bath vary from 4.0 to 11.2 GPa and tensile stress varies from 3.7 to 16.6 GPa similarly for ultrasound the compressive stress varies from 22.0 to 16.0 GPa and tensile stress varies from 0.9 to 4.8 GPa respectively for sulphamate, Watts, sulphate to chloride.

v. The structural properties like hardness and stress analysis were observed to give an overview on which electrolyte is better to be used for further applications both for silent and ultrasound. From the above results and discussions it shows that sulphamate is best among the other baths because the microhardness is large for sulphamate. Also the roughness and residual stress are less for sulphamate, but as the reagents required for sulphamate bath is quite expensive for structural and functional applications, so next to it, mostly Watts is preferred. An emerging technique sono-electroplating, coupling ultrasound with electroplating, has been used to synthesize Ni films at room temperature. And the effect of ultrasonic vibration on evolution of residual stresses along with analysis of various parameters including hardness, surface finish has improved a lot compared to the electroplated nickel thin films. Also the results indicate that ultrasound has a definite impact on the deposit characteristics. However the study needs further critical analysis on residual stress for better understanding.

References

[1] Li-Jian Meng, M.P. Dos Santos, A study of residual stress on rf reactively sputtered RuO_2 thin Films, Thin Solid Films 375 (2000) 29 –32.

[2] Y. Choi, S. Suresh, Size effects on the mechanical properties of thin polycrystalline metal films on substrates, Acta Materialia 50 (2002) 1881–1893.

[3] S. U. Jen, T. C. Wu, Young's modulus and hardness of Pd thin films, Thin Solid Films 492 (2005) 166 – 172.

[4] M. Yu, J. Zhang, D. Li, Q. Meng, W. Li, Internal stress and adhesion of Cu film/Si prepared by both MEVVA and IBAD, Surface & Coatings Technology 201 (2006) 1243–1249.

[5] M. W. Denhoff, A measurement of Young's modulus and residual stress in MEMS bridges using a surface profiler, Journal of Micromechanics and Microengineering 13 (2003) 686–692.

[6] L. R. Shaginyan, M. Misina, J. Zemeb, J. Musil, F. Regenct, V. F. Britun, Composition, structure, microhardness and residual stress of W–Ti–N films deposited by reactive magnetron sputtering, Thin Solid Films 408 (2002) 136–147.

[7] G. Abadias, Y. Y. Tse, Determination of intrinsic stresses in textured and epitaxial TiN thin films deposited by dual ion beam sputtering, Surface and Coatings Technology 180 (2004) 33–40.

[8] C. T. Chuanga, C. K. Chaob, R. C. Changa, K. Y. Chu, Effects of internal stresses on the mechanical properties of deposition thin films, Journal of materials processing technology, 201 (2008) 770–774.

[9] V. Weihnacht, W. Bruckner, Dislocation Accumulation and Strengthening in Cu thin Films, Acta Materialia 49 (2001) 2365–2372.

[10] F. A. Doljack, R. W. Hoffman, The origin of stresses in thin Nickel films, Thin Solid Films 12 (1972) 71-74.

[11] R. C. Cammarata, T. M. Trimble, D. J. Srolovitz, Surface stress model for intrinsic stresses in thin films, Journal of Materials Research 15 (2000) 2468-2474.

[12] J. G. Kim, J. Yu, D. H. Cho, Y. J. Baik, Calculation of intrinsic stress by creep deformation of a Si substrate on chemical vapour deposited diamond films, Diamond and Related Materials 9 (2000) 61–66.

[13] R. J. Dresea, M. Wuttig, In Situ Stress Measurements In Zirconium and Zirconium Oxide films prepared by direct current sputtering, Journal Of Applied Physics 99 (2006) 1-5.

[14] R. Abermann, R. Kramer, J. Maser, Stucture and internal stress in ultra thin Silver films deposited on MgF_2 and SiO substrates, Thin Solid Films 52 (1978) 215-229.

[15] L. B. Freund, S. Suresh, Thin Film Materials, stress defect formation and surface evolution, Cambridge University Press, ISBN: 0 521 82281 5, 2003.

[16] A. L. Shulla, F. Spaepen, Measurements of stress during vapour deposition of copper and silver thin films and multilayers, Journal of Applied Physics 80 (1996) 6243-6255.

[17] N. E. Reish and G. H. Girty, Visualizing stress and strain, http://www.geology.sdsu.edu/visualstructure/vss/htm_hlp/ns_ste.htm, accessed on 24/04/2013.

[18] M.N. James, Residual Stress Influences in Mechanical Engineering, XVIII Congreso Nacional de Ingeniería Mecánica 1 (2010) 1-12

[19] M. Mahdi, L. Zhang, Applied mechanics in grinding. Part 7: Residual stresses induced by the full coupling of mechanical deformation, thermal deformation and phase transformation, International Journal of Machine Tools & Manufacture 39 (1999) 1285–1298.

[20] L. Mordfin, Measurement of residual stresses: Problem and opportunities, Residual stress for designer and metallurgist (1992) 189-209.

[21] Z. Wang, B. Gong, Residual stress in the forming of metals: Handbook of residual stress and deformation of steel, ASM International (2002) 141-149.

[22] P.J. Withers, H.K.D.H. Bhadeshia, "Residual stress Part 1 – Measurement technique, Materials science and technology 17 (2001) 355-365.

[23] J. Schwaighofer, Determination of residual stresses on the surface of structural parts, Experimental Mechanics 4 (1964) 54-56.

[24] P.J. Withers, H.K.D.H. Bhadeshia, Residual stress. Part 2 – Nature and origins, Materials Science and Technology 17 (2001) 366-375

[25] Metal Finishing News, Residual Stresses and Their Origins in Manufacturing Processes, http://www.mfn.li/article/print_article.php?id=861, (2013) accessed on 24/04/2013.

[26] W. Z. Zhuang, G. R. Halford, Investigation of residual stress relaxation under cyclic load, International Journal of Fatigue 23 (2001) S31–S37.

[27] W. Jiang, Y. Zhang, W. Woo, Using heat sink technology to decrease residual stress in 316L stainless steel welding joint: Finite element simulation, International Journal of Pressure Vessels and Piping, 92 (2012) 56-62.

[28] O.N.Mohanty, Residual stresses in heat treatment, Tata steel, Jamshedpur http://eprints.nmlindia.org/5773/1/P-1__P-9.PDF, (1994) accessed on 01/05/2013.

[29] M. N. James, D. J. Hughes, Z Chen, H Lombard, D. G. Hattingh, D. Asquith, J. R. Yates and P. J. Webster, Residual stresses and fatigue performance, Engineering Failure Analysis, 14 (2007) 384-385.

[30] M. Beghini, L. Bertini et al., Residual stress distribution measurements in shot peened aluminium plates, Surface Treatment on Computational Mechanics Publications (1999) 301-309.

[31] A. Gruning, M. Lebsanft, B. Scholtes, Residual Stress in Tools and Components in Case of Thermo-Mechanical Metal Forming Processes, Materials Science Forum 681 (2011) 340-345.

[32] A. Weise, S. Lippmann and G. Fritsche, Measurement of residual stresses in heat treated steels, Fresenius' Journal of Analytical Chemistry 349 (1994) 165-167.

[33] Y. Matsumoto, M.M. Barash, C.R. Liu, Effect of hardness on the surface integrity of AISI 4340 Steel, Journal of Engineering for Industry 108 (1986) 169–175.

[34] J.D. Thiele, S.N. Melkote, R.A. Peascoe, T.R. Watkins, Effect of cuttingedge geometry and workpiece hardness on surface residual stresses in finish hard turning of AISI 2100 steel, Journal of Manufacturing Science and Engineering 122 (2000) 642–649.

[35] J.D. Thiele, S.N. Melkote, The effect of tool edge geometry on workpiece sub-surface deformation and through-thickness residual stresses for hard turning of AISI 52100 steel, Transactions NAMRI/SME 27 (1999) 135–140.

[36] P. Dahlman, F. Gunnberg, M. Jacobson, The influence of rake angle, cutting feed and cutting depth on residual stresses in hard turning, Journal of Materials Processing Technology. 147 (2004) 181–184.

[37] Y. Matsumoto, F. Hashimoto, G. Lahoti, Surface integrity generated by precision hard turning, Annals CIRP 48 (1999) 59–62.

[38] A.M. Abrao, D.K. Aspinwall, The surface integrity of turned and ground hardened bearing steel, Wear 196 (1996) 279–284.

[39] S.R. Agha, C.R. Liu, Experimental study on the performance of super finish hard turned surfaces in rolling contact, Wear 244 (2000) 52–59.

[40] J. Hua, X. Cheng, V. Bedekar, R. Shivpuri, Y. Matsumoto, F. Hashimoto, T.R. Watkins, Effect of feed rate, workpiece hardness and cutting edge on subsurface residual stress in the hard turning of bearing steel using chamfer hone cutting edge geometry, Material Science Engineering A 394 (2005) 238–248.

[41] S. Mittal, C.R. Liu, A method of modeling residual stresses in super finish hard turning, Wear 218 (1998) 21–33.

[42] B. Ekmekci, Residual stresses and white layer in electric discharge machining (EDM), Applied Surface Science 253 (2007) 9234–9240.

[43] R.H. Leggatt, Residual stresses in welded structures, International Journal of Pressure Vessels and Piping 85 (2008) 144–151.

[44] L. Mordfin, Measurement of residual stresses: Problem and opportunities, Residual stress for designer and metallurgist, (1992) 189-209.

[45] Z. Wang, B. Gong, Residual stress in the forming of metals: Handbook of residual stress and deformation of steel, ASM International, (2002) 141-149.

[46] P.J. Withers, H.K.D.H. Bhadeshia, Residual stress Part 1 – Measurement technique, Materials science and technology 17 (2001) 355-365.

[47] J. Schwaighofer, Determination of residual stresses on the surface of structural parts, Experimental Mechanics 4 (1964) 54-56.

[48] W. Buckel, Internal stresses, Journal of Vacuum Science & Technology 6 (1969) 606-609.

[49] R. W. Hoffman, Stresses in shin films: The relevance of grain boundaries and impurities, Thin Solid Films 34 (1976) 185-18 8.

[50] W. D. Nix, B. M. Clemens, Crystallite coalescence: A mechanism for intrinsic tensile stresses in thin films, Journal of Materials Research 14 (1999) 3467-3473.

[51] G.C.A.M. Janssen, Stress and strain in polycrystalline films, Thin Solid Films 515 (2007) 6654-6664.

[52] A. Mallik and B.C. Ray, Residual stress and nanomechanical properties of sonoelectrodeposited Cu films, Surface Engineering 27 (2011) 551-556.

[53] G. Abadias, Y. Y. Tse, Determination of intrinsic stresses in textured and epitaxial TiN thin films deposited by dual ion beam sputtering, Surface and Coatings Technology 180 –181 (2004) 33–40.

[54] C. Q. Liu, W. L. Li, W. D. Fei, Determination of the macroscopic residual stress in thin film with fiber texture on the basis of local grain-interaction models, Acta Materialia 58 (2010) 5393-5401

[55] A. Kumar, U. Welzel, E. J. Mittemeijer, Direction-dependent grain interaction in nickel and copper thin films, analysed by X-ray diffraction, Acta Materialia 54 (2006) 1419–1430.

[56] S. Kal, A. Bagolini, B. Margesin, M. Zen, Stress and resistivity analysis of electrodeposited gold films for MEMS application, Microelectronics Journal 37 (2006) 1329–1334.

[57] F. Spaepen, Interfaces and stresses in films, Acta Materialia 48 (2000) 31-42.

[58] E. Klokholm and B. S. Berry, Intrinsic stress in evaporated metal films, Journal of The Electrochemical Society 115 (1968) 823-826.

[59] R. Abermann, R. Kramer, and J. Maser, Structure and internal stress in ultra-thin silver films deposited on MgF2 and SiO substrates, Thin Solid Films 52 (1978) 215-229.

[60] R. Koch and R. Abermann, Microstructural changes in vapor-deposited silver, copper and gold films investigated by internal stress measurements, Thin Solid Films 140 (1986) 217-226.

[61] R. Abermann, Measurements of the intrinsic stress in thin metal films. Vacuum 41 (1990) 1279-1290.

[62] A. L. Shull and F. Spaepen, Measurements of stress during vapor deposition of copper and silver thin films and multilayers, Journal of Applied Physics 80 (1996) 6243-6256.

[63] R. Abermann and R. Koch, The internal stress in thin silver, copper and gold films, Thin Solid Films 129 (1985) 71-78.

[64] R. Abermann, H.P. Martinz, Internal stress and structure of evaporated chromium and MgF2 films and their dependence on substrate temperature. Thin Solid Films 115 (1984) 185-194.

[65] G. Thurner and R Abermann, On the mechanical properties of uhv-deposited Cr films and their dependence on substrate temperature, oxygen pressure and substrate material. Vacuum 41 (1990) 1300-1301.

[66] G. Thurner and R. Abermann, Internal stress and structure of ultrahigh vacuum evaporated chromium and iron films and their dependence on substrate temperature and oxygen partial pressure during deposition. Thin Solid Films 192 (1990) 277-285.

[67] H. J. Schneeweiß and R. Abermann, Ultra-high vacuum measurements of the internal stress of PVD titanium films as a function of thickness and its dependence on substrate temperature, Vacuum 43 (1992) 463-465.

[68] Carl V. Thompson, The Origin and Control of Residual Stress in Polycrystalline Films for Applications in Microsystems,

http://www.sematech.org/meetings/archives/reliability/20041025/MEMs/04MEMs_CThompson_TRC2004.pdf, (2004) accessed on 13/05/2013.

[69] M. Laugier, Intrinsic stress in thin films of vacuum evaporated LiF and ZnS using an improved cantilevered plate technique, Vacuum 31 (1981) 155-157.

[70] R. Abermann and R. Koch, The internal stress in thin silver, copper and gold films, Thin Solid Films 129 (1985) 71-78.

[71] R. Koch: The intrinsic stress of polycrystalline and epitaxial thin metal films. Journal of Physics: Condensed Matter, 6 (1994) 9519-9550.

[72] J. A. Floro, S. J. Hearne, J. A. Hunte, P. Kotula, E. Chason, S. C. Seel, and C. V. Thompson, The dynamic competition between stress generation and relaxation mechanisms during coalescence of Volmer-Weber thin films. Journal of Applied Physics 89 (2001) 4886-4898.

[73] F. Spaepen, Interfaces and stresses in thin films, Acta materialia 48 (2000) 31-42.

[74] R. W. Hoffman, Stresses in thin films: The relevance of grain boundaries and impurities, Thin Solid Films 34 (1976) 185-190.

[75] W. D. Nix and B. M. Clemens, Crystallite coalescence: A mechanism for intrinsic tensile stresses in thin films, Journal of Materials Research 14 (1999) 3467-3473.

[76] L. B. Freund and Eric Chason, Model for stress generated upon contact of neighboring islands on the surface of a substrate, Journal of Applied Physics 89 (2001) 4866-4873.

[77] F. Spaepen, Interfaces and stresses in thin films. Acta Materialia 48 (2000) 31-42.

[78] A. L. Shull and F. Spaepen, Measurements of stress during vapor deposition of copper and silver thin films and multilayers, Journal of Applied Physics 80 (1996) 6243-6256.

[79] E. Chason, B. W. Sheldon, and L. B. Freund, Origin of compressive residual stress in polycrystalline thin films, Physical Review Letters 88(15) (2002) 156103.

[80] L. Souzis and R. Weil, Residual stresses in electrodeposited nickelmonocrystals, Surface Technology, 4 (1976) 41 – 58.

[81] N. Pangarov and R. Pangarova, Stress in electrodeposited metals general thermodynamic theory, Journal of Electroanalytical Chemistry 91 (1978) 173-188.

[82] F.A. Lowenheim, Electroplating, chapter 7, 1st ed. (New York: McGraw- Hill, 1978).

[83] S.E. Hadian, D.R. Gabe, Residual stresses in electrodeposits of nickel and nickel–iron alloys, Surface and Coatings Technology 122 (1999) 118–135.

[84] S.K. *Ghosh*, A.K. Grover, G.K. Dey, and M.K. Totlani, Internal stress in electrodeposited nanocrystalline Ni-Cu alloys, Transactions of the Institute of Metal Finishing, 80 (2002) 56-59.

[85] S. Basrour and L. Robert, X-ray characterization of residual stresses in electroplated nickel used in LIGA technique, Materials Science and Engineering: A 288, (2000) 270 -274.

[86] F.A. Lowenheim, *Electroplating*, 1st ed. (New York: McGraw- Hill, 1978).

[87] J.K. Dennis and T.E. Such, *Nickel and Chromium Plating*, 3rd ed. (Cambridge, UK: Woodhead Pub., 1993).

[88] R.W. Hoffman,Mechanical Properties of Non-Metallic Thin Films, Physics of Nanometallic Thin films 14 (1976) 273-353.

[89] Takao Hanabusa, Kazuya Kusaka, Osami Sakata, Residual stress and thermal stress observation in thin copper films, Thin Solid Films 459 (2004) 245–248.

[90] S.H. Kim, J.Y. Kim, J. Yu and T.Y. Lee, Residual Stress and Interfacial Reaction of the Electroplated Ni-Cu Alloy under Bump Metallurgy in the Flip Chip Solder Joint, Journal of Electronic Materials 33(2004) 948-957.

[91] B. Okolo, The effect of deposition parameters and substrate surface condition on texture, morphology and stress in magnetron-sputter-deposited Cu thin films, Thin Solid Films 474 (2005) 50–63.

[92] M. Yu, J. Zhang, D. Li, Q. Meng and W. Li, Internal stress and adhesion of Cu film/Si prepared by both MEVVA and IBAD Surface Coating Technology 201 (2006) 1243–1249.

[93] T. Hanabusaa, K. Kusakaa and O. Sakatab, Thin Solid Films 459 (2004) 245–248.

[94] S. Kima, J. H. Jang, J. S. Lee and D. J. Duquette, Stress behavior of electrodeposited copper films mechanical supporters for light-emtting diodes, Electrochimica Acta 52 (2007) 5258–5265.

[95] Madhusmita Moharana, Archana Mallik, Nickel electrocrystallization in different electrolytes: An in-process and post synthesis analysis, Electrochimica Acta 98 (2013) 1-10.

[96] P. B. S. N. V. Prasad, R. Vasudevan, S. K. Seshadri, Residual stresses of nickel electrodeposits with ultrasonically agitated Bath, Journal of Materials Science Letters 11 (1992) 1424-1425.

[97] A. Chiba, H. Haijima, K. Kobayashi, Effect of sonication and vibration on the electroless Ni–B deposited film from acid bath, Surface and Coatings Technology 169 –170 (2003) 104–107.

[98] A. Mallik, B. C. Ray, Residual stress and namomechanical properties of Sonoelectrodeposited Cu thin films, Surface Engineering 27 (2011) 551-556.

[99] T. Hanabusa, K. Kusaka, O. Sakata, Residual stress and thermal stress observation in thin copper films, Thin Solid Films 459 (2004) 245–248.

[100] H. Natter and R. Hempelmann, Nanocrystalline copper by pulsed electrodeposition: The effects of organic additives, Bath temperature and PH 50 (1996) 19525-19532.

[101] M.H. Seo, D.J. Kim, J.S. Kim, The effect of PH and temperature of Ni-Fe-P alloy electrodeposition from a sulfamate bath and the material properties of the deposits, Thin solid films 489 (2005) 122-129

[102] M. Birkholz, C. Genzel, T. Jung, X-ray diffraction study on residual stress and preferred orientation in thin titanium films subjected to a high ion flux during deposition, Journal Of Applied Physics 96 (2004) 7202-7211.

[103] X. Zhang, K .S. Chen, R. Ghodssi, A. A. Ayon, S. M. Spearing, Residual stress and fracture in thick tetraethylorthosilicate (TEOS) and silane based PECVD oxide films, Sensors and Actuators A 91 (2001) 373-380.

[104] A Review of Residual Stress Measurement Methods- A guide to Technique Selection, National Physical Laboratory, UK, Report MATC (A) 04 (2001) ISSN: 1473-2734.

[105] D.A. Glocker, S. Shah, Handbook of Thin Film Process Technology, Institute of Physics Publishing, Bristol and Philadelphia (1998)

[106] K.L. Chopra, I. Kaur, Thin Film Device Application, New York & London, Plenum Press, Physical Review B: 49 (1983) 106.

[107] Kanani N.,Electroplating-Basic principle,process and practice,Elsevier Ltd.2004

[108] A. Mallik and B.C. Ray, Residual stress and nanomechanical properties of sonoelectrodeposited Cu films, Surface Engineering 27 (2011) 551-556.

[109] P.R. Birkin, D.G. Offin, P.F. Joseph and T. G. Leighton, Cavitation, Shock Waves and the Invasive Nature of Sonoelectrochemistry, Journal of physical chemistry B 109 (2005) 16997-17005.

[110] M.R. Khelladi, L. Mentar, A. Azizi, A. Sahari, A. Kahoul, Electrochemical Nucleation and growth of copper deposition onto FTO and n-Si(100) electrodes; Materials Chemistry and Physics 115 (2009) 385-390.

[111] M.R. Majidi, K.A. Zeynoli K, B. Hafezi, Reaction and Nucleation mechanisms of copper electrodeposition on disposable pencil graphite electrode, Electrochimica Acta 54 (2009) 1119-1126.

[112] D. Grujicic, B. Pesic, Electrodeposition of copper: the nucleation mechanism; Electrochimica Acta 47 (2002) 2901-2912.

[113] J. Randles, A cathode ray polarograph, Trans. Far. Soc. 44 (1948) 327.

[114] J. Bard, L.R. Faulkner, Electrochemical Methods, Fundamentals and Applications, 2nd ed. New York: John Wiley and Sons; 2001.

[115] R. Parsons, The electrical double layer: recent experimental and theoretical developments, Surface Science 90 (1990) 813.

[116] R. Orinakova, L. Trnkova, M. Galova, M. Supicova, Application of elimination voltammetry in study of electroplating processes on the graphite electrode, Electrochimica Acta 49 (2004) 3587.

[117] G.R.P.Malpass, M. Kalaji, E.C.Venancio, A.J. Motheo, Electrodeposition of nickel on carbon felt, Electrochimica Acta 49 (2004) 4933.

[118] R. Orinakova, M. Streckova, L. Trnkova, R. Rozik, M. Galova, Comparison of chloride and sulphate electrolytes in nickel electrodeposition on a paraffin impregnated graphite electrode, Journal of Electroanalytical Chemistry 594 (2006) 152.

[119] M.R. Khelladi, L. Mentar, A. Azizi, A. Sahari, A. Kahoul, Electrochemical Nucleation and growth of copper deposition onto FTO and n-Si(100) electrodes; Materials Chemistry and Physics 115 (2009) 385-390.

[120] D. Grujicic, B. Pesic, Electrodeposition of copper: the nucleation mechanisms, Electrochimica Acta 47 (2002) 2901-2912.

[121] http://en.wikipedia.org/wiki/X-ray_crystallography, accessed on 10.03.2010

[122] http://en.wikipedia.org/wiki/Scanning_electron_microscope, accessed on 12.05.2013.

[123] http://en.wikipedia.org/wiki/Energy-dispersive_X-ray_spectroscopy, accessed on 12.05.2013

[124] G. Binning, C. F. Quate, Ch. Gerber, Atomic force microscope. Physical Review Letters 56 (9) (1986) 930-933.

[125] http://www.hardnesstesters.com/Applications/Vickers-Hardness-Testing.aspx, accessed on 17/05/13.

[126] B. Scarifker, G. Hills, Theoritical and Experimental Studies of Multiple Nucleation, Electrochimica Acta 28 (1983) 879-889.

[127] A. Mallik, A. Bankoti, B.C. Ray, A study on the Modification of Conventional Electrochemical Crystallization under Sonication: The Phenomena of Secondary Nucleation, Electrochemical and Solid State Letters 12 (2009) F46-F49

[128] A. Bewick, M. Fleischmann, H.R. Thirsk, Kinetics of Electrocrystallisation of Thin Films of Calomel, Transaction of Faraday Society 58 (1962) 2200-2216.

[129] B. Scharifker, B. Hills, Theoretical and experimental studies of multiple nucleation, Electrochimica Acta 28 (1982) 879-889.

[130] L.P. Wang, Y. Gao, T. Xu, Q.J. Xue, Comparative study on the tribological behavior of nanocrystalline nickel and cobalt coatings correlated with grain size and phase structure, Materials Chemistry and Physics 99 (2006) 96-103.

[131] J. Lian, B. Baudelet, A. A. Nazarov, Model for the prediction of the mechanical behaviour of nanocrystalline materials, Materials Science and Engineering A172 (1993) 23-29.

[132] A.M. El-Sherik, U. Erb, G. Palumbo, et al., Deviations from Hall-Petch behaviour in as-prepared nanocrystalline nickel, Scripta Metallurgical Materialia 27 (1992) 1185-1187.

[133] X. Yuan, Y. Wang, D. Sun, H. Yu, Influence of pulse parameters on the microstructure and microhardness of nickel electrodeposits, Surface Coating Technology 202 (2008) 1895-1903.

[134] T. Hanabusa, K. Kusaka, O. Sakata, Residual stress and thermal stress observation in thin copper films, Thin Solid Films 459 (2004) 245–248.